CHARACTERISATION OF AEROSOLS FROM SIMULATED RADIOLOGICAL DISPERSION EVENTS

CHARACTERISATION OF AEROSOLS FROM SIMULATED RADIOLOGICAL DISPERSION EVENTS

Proefschrift

ter verkrijging van de graad van doctor
aan de Technische Universiteit Delft,
op gezag van de Rector Magnificus prof. ir. K. C. A. M. Luyben,
voorzitter van het College voor Promoties,
in het openbaar te verdedigen op dinsdag 16 maart 2015 om 10:00 uur

door

Fidelma Giulia DI LEMMA

Diploma di Laurea Magistrale in Ingegneria Energetica,
Università degli studi di Roma, "La Sapienza", Italië
geboren te Cork, Ierland.

Dit proefschrift is goedgekeurd door de promotor:

Prof. dr. R.J.M. Konings

Rector Magnificus,	voorzitter
Prof. dr. R.J.M. Konings,	Technische Universiteit Delft, promotor
Prof. dr. H.T. Wolterbeek,	Technische Universiteit Delft
Prof. dr. A. Schmidt-Ott,	Technische Universiteit Delft
Prof. dr. ir. R. Remetti,	Università degli studi di Roma, La Sapienza
Prof. dr. H. Horvath,	University of Vienna
Dr. K. Mayer,	Institute for Transuranium Elements
Dr. ir. J. L. Kloosterman,	Technische Universiteit Delft

The research described in this thesis was performed within a cooperation of the Institute for Transuranium Elements (ITU) of the Joint Research Centre (JRC) of the European Commission, P.O. Box 2340, 76125 Karlsruhe, Germany and the Department of Radiation Science and Technology, Faculty of Applied Sciences, Delft University of Technology, Melkeweg 15, 2629 JB Delft, The Netherlands.

An electronic version of this dissertation is available at
http://repository.tudelft.nl/.

Bibliographic information published by the Deutsche Nationalbibliothek – Standard CIP-Record. The German National Library lists this publication in the Deutsche Nationalbibliografie; detailed bibliographic data are available in the Internet at < http://dnb.ddb.de >

Fidelma Giulia Di Lemma

Characterisation of aerosols from simulated Radiological Dispersion Events

©sierke VERLAG
Tel. 0551-503664-7 | Fax 0551-3894067
www.sierke-verlag.de

Graphic: sierke VERLAG
Printed on acid- and chlorine-free paper.

ISBN 13: 978-3-86844-687-6
1. Edition 2015

An expert is a person
who has made all the mistakes
that can be made
in a very narrow field

Niels Bohr

CONTENTS

1

INTRODUCTION

1.1. MOTIVATION TO THIS WORK

Nuclear Safety and Security are pillars for the application of the nuclear technology and for its acceptance by the public. Moreover the regulatory authorities require nuclear facilities to guarantee that the radioactive contamination, following accidents and/or sabotage involving their nuclear material inventory, remains within the licensed limits and require to study emergency plans for such events. In addition the Fukushima accident has caused a re-focus on nuclear reactor safety worldwide. This accident has shown that events previously considered unlikely can indeed happen and their environmental impact therefore needs to be evaluated. Following this event, attention has been focused also on the safety of spent fuel ponds, which were previously neglected in the assessment of the radiological consequences. The safety of nuclear material has become consequently relevant not only during reactor operations, but also in all the other phases of the nuclear fuel cycle (including the storage and transport) and the assessment of the radiological consequences should be carried out also for these phases.

Scenarios to be investigated for such assessments include furthermore malicious attacks. This has become relevant after the $9/11^{th}$ terrorist attack. After this event attention has been focused on CBRN (Chemical, Biological, Radiological and Nuclear) devices that could be used by terrorist groups to spread panic. An Improvised Nuclear Device (IND) will be difficult to acquire or create, due to the high regulatory control on fissile materials (such as highly enriched uranium or plutonium) and also due to technical complexity of building such weapons. "Dirty bombs", a.k.a. RDD's (Radiological Dispersion Devices), are instead feared to be of interest to terroristic groups, as they are simply created by coupling a conventional explosive with a highly radioactive material. These materials can be accessible, as they are commonly used in nuclear medicine or in industrial processes. Following the radiological consequences of RDD's detonations should be studied. It worth pointing out the difference between

a nuclear explosion (e.g. from a IND) and a RDD detonation. The former consists of an explosion produced by a uncontrolled fission chain reaction and will generate an enormous blast accompanied by the release of high energy gamma rays and neutrons. As an example a nuclear weapon of 1000 kg can produce an explosive force comparable to the detonation of more than 1 million tonnes of TNT (Trinitrotoluene) explosive. Such weapons will generate a high number of casualties and the destruction of a city. RDD's instead do not have the aim of destroying a city or creating a high number of fatalities, their aim is the release of radioactivity in the environment. This can have a high impact due to the panic spread and the economic cost of the clean up [1, 2]. Moreover apart from the economic damage, an important major long-term effect is related to human health, consisting of an increase of cancer rate mainly related to inhalation of radioactive particles [2, 3].

To assess the consequences of such Radiological Dispersion Events (RDE's) it is necessary to perform a source term evaluation. This consist of a quantitative description of the radioactive release, which include both the gaseous species and aerosols released. This description is also the input of simulation codes (e.g. ARGOS, RODOS, HOTSPOT [4–6]) that are used for calculating the extension and the level of the contaminated area. The results from such codes are needed for the creation of emergency plans and to plan mitigation strategies but also to assess the health consequences of radioactive releases for the population. However the description of the source term can suffer of high uncertainties, which can affect the results of the calculations. Therefore extensive studies are necessary for reliable source term input data.

1.2. LITERATURE REVIEW

Extensive research was conducted on the gaseous and aerosol release of radioactive species following nuclear reactor accidents. These studies focused mainly on the fission products behaviour in accidental conditions [7–17]. The technical report of NEA (Nuclear Energy Agency) for OECD (Organisation for Economic Co-operation and Development) [8] is an important and complete reference, summarizing the experiments and most important findings on nuclear aerosol release. In their final recommendations the authors conclude that although progress has been made in the understanding of the physics and chemistry of nuclear aerosols, further investigations are needed on various topics (e.g. resuspension and revaporization phenomena, influence of recombiners, influence of chemistry etc.). Separate effect experiments consequently are useful for a better understanding of the influence of single variables on the aerosols characteristics.

Studies on the radioactive release following nuclear reactor accidents give strong attention to the release of cesium and iodine, especially following the Three Mile Island accident [7, 14, 17]. These elements have been especially investigated due to their volatility and radiological health effects. Attention is focused on the I^{131} and on the Cs^{137} and Cs^{134} isotopes, which are very dangerous due to their chemical reactive and high solubility in the blood stream [18, 19]. Moreover for the cesium isotopes the

half-life of 30 and 2 years leads to long duration of the contamination of the affected area. It is thus important to analyse the release of these radioactive elements after a RDE. In the last years attention has been posed also on molybdenum and ruthenium release, which initially were thought to be retained in the metallic form in the nuclear fuel. However when accidental oxidising conditions are achieved volatile species can be formed (such RuO_3 or RuO_4, and MoO_3) leading to the release of these elements. This was also observed in the Phébus experiments [17]. These experiments consisted of the analyses of the release from a scaled nuclear reactor experiencing different accidental scenarios until core degradation was achieved. The interaction of such metallic fission products with CsI can have an effect on the iodine gaseous release, as observed for molybdenum [20–22]. On the other hand for ruthenium experiments have focused on its release from UO_2 fuel or simulated ZrO_2 fuel [23–25] and less attention has been focused on its interaction with other chemical species. The interaction of Cs with Ru was investigated, only by Hózer et al. [25] and Vér et al. [26], by the vaporization of these compounds in a furnace and the analyses of the escaping gases after a low temperature region. The escaping gases were collected by means of a NaOH adsorber solution. From these experiments it was observed that Ru gases had a lower concentration coupled with a delay in the maximum concentration in the adsorber solutions when Cs was present. It was inferred that these effects were related to the formation of Cs_2RuO_4, which by condensing and depositing in the cold region after the furnace can avoid the ruthenium containing gases to reach the adsorber. Thus the interaction of Cs and I with these metallic fission products need further investigation.

For sabotage involving radioactive materials, a.k.a. dirty bomb detonations, fewer tests have been performed. In the past some integral tests were performed, as reported in [27–29]. Lee et al. [27] concentrated their study on CsCl samples, creating a simulated dirty bomb from non-radioactive powder coupled with C4 explosive. They tested also the influence of soil on the aerosol formed, and analysed the particles mass concentration and particles characteristics by SEM/EDX. Prouza et al. [28] applied instead a radioactive substance ($^{99\text{-m}}Tc$ solution in water colored with potash) studying in a free and indoor environment the dose rate distribution, surface and volume activities after exploding it. The particles were collected by inertial impactors. This permitted their classification by their aerodynamic equivalent diameter (AED) and the analysis of the dose and activities in relation to the particles size range. One of the most interesting studies on dirty bombs detonations was conduced by Harper et al. [29], in a 20 year study program at the Sandia National Laboratories. They performed explosive aerosolization tests on a wide range of materials. The experiments were conducted in a chamber, in which the atmosphere could be controlled. The aerosols were then washed in a smaller stainless steel chamber, where they were collected with different systems (such as cascade impactors, filters, deposition wires etc.) for post analyses of size distribution and total mass released. They also considered the time dependence of this parameter. Lee et al. [27] observed an influence of the soil on the aerosols, but due to limited data could not assess the phenomena taking place. Harper et al. [29] focused instead at describing the formation mechanism. Finally Prouza et al. [28] assessed the aerosols dimension (mean diameter 10μm) and observed that the

activity is predominantly attached to the particles surface. The results of Prouza et al. [28] however could have been highly influenced by the form chosen for the radioactive source (liquid solution). While these experiments [27–29], as presented, have tried to simulate dirty bombs detonations and to describe the activity and material released, separate studies are needed for a deeper understanding of the aerosol formation processes and of the influence of different materials on the aerosols characteristics.

Finally studies were also performed on release from spent fuel during storage or nuclear transports. These focused on the risk assessment and identified such events as unlikely [30–34]. As a result the source term characterisation for such events was not performed. However the Fukushima accident has renewed the interest on the analyses of the radioactive release from these events. Moreover also sabotage scenarios involving spent fuel should be taken in account. For these scenarios the only studies available, focusing on the aerosol source term evaluation, are those of Molecke et al. [35, 36]. They studied the exploding of a High Energy Density Device (HEDD) with surrogate nuclear spent fuel (rodlets containing CeO_2, or depleted UO_2) and studied the formed particles, focusing on the respirable fraction, and the enhancement of fission products in the aerosols. They observed an enrichment of the high volatile element class, simulated only by CsI, in the respirable fraction, while the matrix elements (CeO_2, or depleted UO_2) were concentrated in the bigger particles. Thus the possibility of a radioactive elements partitioning as function of the aerosol sizes was observed. However such experiments were conducted on simulated spent nuclear fuel with a limit number of chemicals (only CsI, RuO_2, SrO, Eu_2O_3) to simulate the different fission products volatility class. Thus more studies are needed to evaluate and understand an eventual fission product partitioning as function of particles size.

In the current studies aerosols from simulated RDE's have been produced by a laser heating technique and analysed by various post-analyses techniques for a complete aerosol characterisation. Laser heating has been newly applied for the simulation of RDE's (Radioactive Dispersion Events) and its choice over other available heating techniques, as explained in Chapter 2, is related to specific experimental requirements. Only a few examples of application of laser heating to simulate accident conditions have been reported [37, 38], and only Zanotelli et al. [38] applied this technique to study, similar to our application, the aerosols released from nuclear material. On the other hand many studies have applied laser heating for the investigation of the thermophysical properties of nuclear and non-nuclear materials [39–42]. Moreover laser ablation is commonly used for the production of nanoparticles in controlled atmosphere [43–45]. In those case generally pulsed lasers were used, applying very short pulses (<ms) and reaching high energy density on the samples. This will lead to the creation of a plasma over the sample, from which then nanoparticles nucleate. In our experiments the selected sample materials are vaporized by a laser pulse that is much longer but has a smaller energy density. Thus plasma formation is not achieved. The material is thus only heated and vaporized and aerosols are formed from the nucleation/condensation of the released vapour. Most studies on aerosol formation mechanisms were performed for aerosols produced by free jet aerosol generators in [46–52].

This system consists of a gaseous precursor jet introduced into the center of a co-flow laminar flame stream. This stream mixes at different axial distances with ambient air [48], thus the thermal gradient is less abrupt than in our set-up. In contrast the plasma gas generated by laser ablation can encounter steeper thermal gradients during the aerosol formation. As in our set-up intermediate conditions with respect to the previously studies methods can be reached, there is a need for the investigation of the influence of the aerosol formation mechanisms on the produced aerosols characteristics. Finally although laser heating cannot provide a full simulation of a detonation (e.g. shock waves with an impact pressure up to 450 GPa), it is useful to simulate the process of rapid expanding hot gases (up to approximately 5500 K in the microsecond range [53, 54]) involved in the detonation or to study the vaporization process related to high temperature release.

1.3. AIM OF THE WORK

The research described in this thesis aims at improving the evaluation of the radioactive release by describing the aerosol release from different dispersion scenarios, such as accidents and sabotage involving radioactive and nuclear materials. These studies contribute to a better assessment of the source term as input for the codes (such as ARGOS, RODOS, HOTSPOT [4–6]), which calculate the extension and level of the contaminated area. A better source term description for such codes will finally lead to improved predictions for such events, with impact on the risk assessment and on the creation of emergency plans. These codes could be improved for example by a better description of the particles size distribution and of the radioactive elements partitioning as a function of particles' size. Although the aerosol size distribution influences highly the transport behaviour, the majority of codes do not take into account such parameter. The input source term is divided only in respirable and not-respirable fractions or apply a simplified uniform plume model varying just the settling velocity. Moreover a homogeneous radioactivity partitioning between the different aerosols size ranges is considered. Calculations could be influenced if this hypothesis is not met, as in the case of radioactive elements partitioning in the aerosols as function of their size. Thus such aerosol characteristics are investigated in our studies.

An important size parameter for the aerosols is the Aerodynamic Equivalent Diameter (AED). This parameter has been chosen in our tests to describe the particles released, as it influences the transport of the radioactive particles in the environment and in the respiratory track. The AED is defined as the diameter of an equivalent spherical particle of 1000 kg/m^3 density having the same settling velocity as the particle studied. The importance of this parameter for the deposition in the lungs is shown in Figure 1.1, as reported in by Guariero and Guariero [55]. Figure 1.1 shows that particles with an AED<10 μm will be inhalable and that these will deposit in different parts of the respiratory systems as function of their AED. It is also demonstrated that the most dangerous aerosols are the ones with an AED<0.1 μm as these will be rapidly incorporated in the blood stream, transported to the complete body and finally will deposit in the organs in which they have a chemical high affinity.

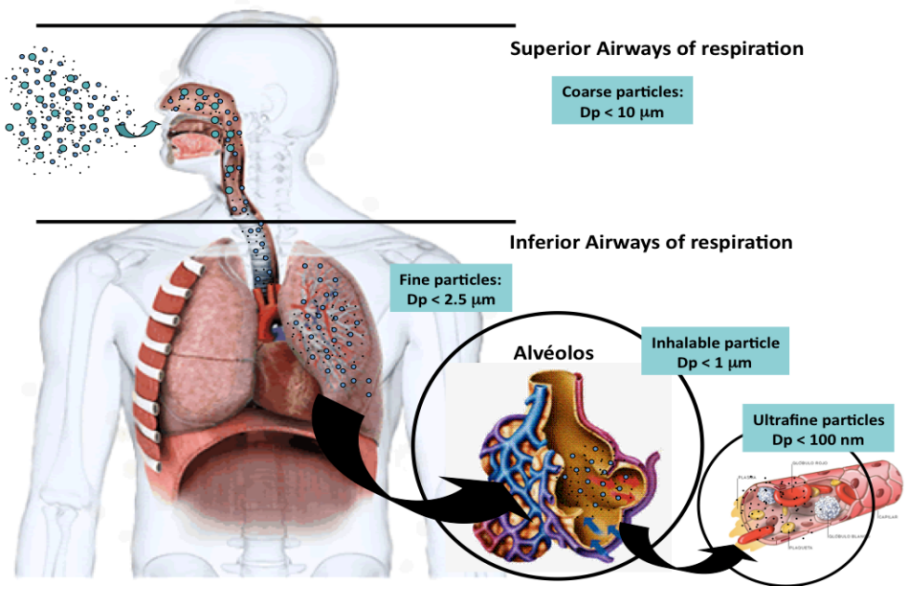

Figure 1.1: Deposition of the particles in the respiratory track. ©2013 Lílian Lefol Nani Guarieiro, Aline Lefol Nani Guarieiro. Originally published in [55] under CC BY 3.0 license. Available from: http://dx.doi.org/10.5772/52513.

Moreover the aim of this study is to investigate the influence of different variables (e.g. interactions with other materials) on the aerosol characteristics by separate effect experiments. By coupling the results from the aerosol characterisation with the study of the gaseous aerosols precursors and their interaction, this research wants finally to provide a basic understanding of the aerosol formation processes for such radioactive dispersion events. Attention is posed in these studies on the influence of the chemical reactions, such as gas-gas and gas-aerosols reactions, on the release.

1.4. THESIS SYNOPSIS

In this section a summary of the thesis layout is presented and a scheme is shown in Figure 1.2. To study and analyse the aerosols release from different RDE's a new experimental set-up was developed (RADES, Radioactive Dispersion Event Set-up), which is presented in Chapter 2. This has been used to produce the aerosols under controlled laboratory conditions and collect them on suitable substrates for post-analyses. Our aerosol characterisation provided information on the morphology, the size distribution and the chemical and elemental composition of the particles as function of the AED size, as this is a fundamental parameter for the risk assessment. This permits to identify in which size range the most dangerous and active compounds will concentrate. In Chapter 2 the post analyses techniques used for the

aerosols characterisation are also described, together with the results of the feasibility studies of this experimental set-up on a range of materials. While the techniques applied for the study of the aerosol gaseous precursors were presented in previous work. Thermochemical equilibrium vaporization calculations (by FactSage software, described in [56, 57]) and experiments with the Knudsen Effusion Mass Spectrometer (KEMS, described in [58, 59]) were used for such studies.

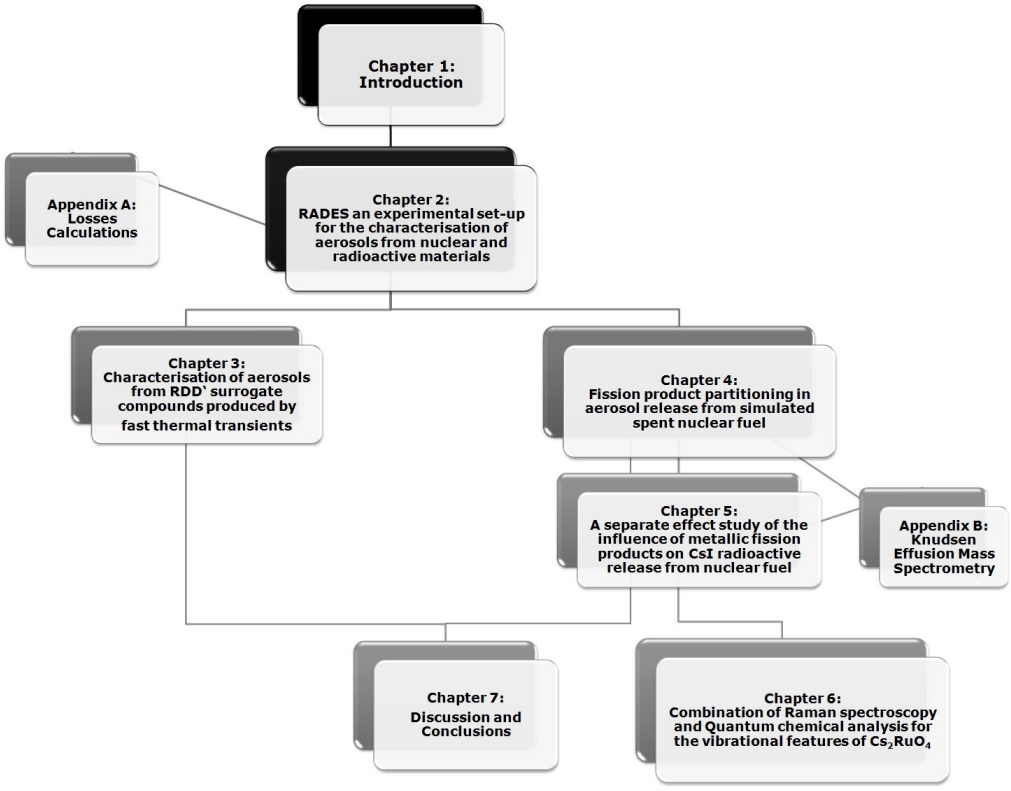

Figure 1.2: A scheme of the thesis layout.

Chapter 3 will describe the release related to sabotage involving radioactive materials (called RDD's, Radioactive Dispersion Devices, or dirty bombs), because for these events an understanding of the chemical behaviour of the aerosols in complex environment is lacking. We have tested a wide range of simulated high activity sources, focusing on the influence of the cladding materials on the aerosol characteristics.

Separate effect studies with this set-up were performed for a range of materials that can cause significant radiological consequence following a release, particularly materials used in the nuclear industries, but also for radioactive source applied widely

in the non-nuclear industry (for example in the nuclear medicine). As shown by the literature review only a few studies were performed on the release from sabotage of radioactive and nuclear materials, and also on the release from spent fuel during storage or transport. Thus the release from such materials is studied in this thesis. Finally also in the case of the extensive research conducted on the radioactive release following nuclear reactor accidents, still some questions need to be addressed. This is especially true for the predictions of the chemical form in the aerosols of radioactive elements such as Cs, I, Ru, and Mo, which will be addressed in this work. These studies are described in the subsequent chapters.

Chapter 4 will treat the release from simulated spent nuclear fuel. These experiments have been conducted with the aim of simulating sabotage or accidents involving spent nuclear fuel under oxidising conditions, such as breaching of the spent fuel cask during transport or uncovering of the spent fuel pond. In this study we investigated the behaviour of the different fission products in the aerosols. These experiments aimed at evaluating the fission product partitioning as function of the aerosols' size range (AED), as this can have an influence on a radioactivity partitioning and finally on codes predictions.

Chapter 5 focuses on the chemical reactions influencing the radioactive release of cesium and iodine, which are important in the case of release from spent nuclear fuel but also in case of a nuclear reactor severe accidents (such as air ingress). The aim was to study the influence of the metallic fission products on CsI release under oxidising conditions. Following such investigations a related study is presented in Chapter 6, on the vibrational structure of one of the compounds observed in these experiments (Cs_2RuO_4). This study was necessary to identify the chemical species of the aerosols released in the experiments presented in Chapter 5.

Finally in Chapter 7 a summary of the results, and the outcomes are presented, together with an outlook for the future research.

REFERENCES

[1] J. Medalia. "dirty bombs": Technical background, attack prevention and response, issues for congress. Technical Report R41890, Congressional Research Service, 2011. Accessed from http://www.fas.org/sgp/crs/nuke/R41890.pdf.

[2] H. Shin and J. Kim. Development of realistic RDD scenarios and their radiological consequence analyses. *Applied Radiation and Isotopes*, 67(7-8):1516–1520, 2009.

[3] J. Magill, D. Hamilton, K. Latzenkirchen, M. Tufan, G. Tamborini, W. Wagner, V. Berthou, and A. von Zweidorf. Consequences of a radiological dispersal event with nuclear and radioactive sources. *Science & Global Security*, 15(2):107–132, 2007.

[4] ARGOS. Computer software CBRN whitepaper. decision support for emergency management, 2008. Accessed from www.pdc.dk/Argos/downloads/ARGOS_whitepaper.pdf.

[5] RODOS. RODOS: Decision support system for off-site nuclear emergency management in europe, 2000. Accessed from http://www.rodos.fzk.de/Overview/moreinfo.html.

[6] HotSpot. NARAC: Hotspot 2.07.2, computer software, 2011. Accessed from https://narac.llnl.gov/HotSpot/HotSpot.html.

[7] P.D.W. Bottomley, B. Clément, T. Haste, D. Jacquemain, M. Powers, D.A. Schwarz, B. Teisseire, and R. Zeyen. Final seminar of the Phébus FP programme. *Annals of Nuclear Energy*, 61:1–230, 2013.

[8] H.J. Allelein, A. Auvinen, J. Ball, S. Guntay, L.E. Herranz, A. Hidaka, A.V. Jones, M. Kissane, D. Power, and G. Weber. State of the art report on nuclear aerosols. Technical report, NEA, Nuclear Energy Agency, 2009.

[9] B.R. Bowsher. Fission-product chemistry and aerosol behaviour in the primary circuit of a pressurized water reactor under severe accident conditions. *Progress in Nuclear Energy*, 20(3):199–233, 1987.

[10] E.H.P. Cordfunke and R.J.M. Konings. The release of fission products from degrade UO_2 fuel: Thermochemical aspects. *Journal of Nuclear Materials*, 201:57–69, 1993.

[11] L.E. Herranz, J. Ball, A. Auvinen, D. Bottomley, A. Dehbi, C. Housiadas, P. Piluso, V. Layly, F. Parozzi, and M. Reeks. Progress in understanding key aerosol issues. *Progress in Nuclear Energy*, 52:120–127, 2010.

[12] T.S. Kress, R.A. Lorenz, T. Nakamura, and M.F. Osborne. Correlation of recent fission product release data. In *ICHMT International Seminar "Fission product transport process in reactor accidents"*, number CONF-890546–7, 1989.

[13] B.J. Lewis, W.T. Corse, M.H. Kaye, F.C. Iglesias, P. Elder, R. Dickson, and Z. Liu. Low volatile fission-products release and fuel volatilization during severe accident conditions. *Journal of Nuclear Materials*, 252:235–256, 1998.

[14] B. Clément, L. Cantrel, G. Ducros., F. Funke, L. Herranz, A. Rydl, G. Weber, and C. Wren. State of the art report on iodine chemistry. Technical report, NEA, Nuclear Energy Agency, 2009.

[15] F.C. Iglesias, B.J. Lewis, P.J. Reid, and P. Elder. Fission products release mechanism during reactor accident conditions. *Solid State Ionics*, 53-56:376–382, 1992.

[16] M.P. Kissane. On the nature of aerosols produced during a severe accident of a water-cooled nuclear reactor. *Nuclear Engineering and Design*, 238:2792–2800, 2008.

[17] W. Krischer and M.C. Rubinsten. *The Phebus fission product project*. Elsevier applied science, 1992.

[18] U.S. Environmental Protection Agency. Commonly encountered radionuclides. Accessed from http://www.epa.gov/rpdweb00/radionuclides/index.html.

[19] Agency for Toxic Substances and Disease Registry. Toxicological profiles-cesium. PB2004-104397 Accessed from http://www.atsdr.cdc.gov/toxprofiles/tp157-c3.pdf.

[20] M. Gouello, M. Lacou-Negre, H. Mutelle, F. Cousin, S. Sobanska, and E. Blanquet. Chemistry of iodine and aerosol composition in the primary circuit o a nuclear power plant. In *Proceedings of ICAPP*, 2011.

[21] M. Lacoue-Negre. *Iodine Chemistry in the reactor coolant system of a nuclear power plant in case of a severe accident – Study of CsI/MoO_3 mixtures under steam*. PhD thesis, University of Lille, December 2010.

[22] M. Lacoue-Negre, H. Mutelle, and F. Cousin. Speciation of aerosol transported in the primary circuit: A comparative study. In *Proceedings International Conference "Nuclear energy for New Europe 2009"*, page 408.1, 2009.

[23] C. Mun, Cantrel, and C. Madic. Review of literature on ruthenium behavior in nuclear power plant severe accidents. *Nuclear Technology*, 156:332–346, 2006.

[24] C. Mun, J. Colombani, and L. Cantrel. Current status on ruthenium chemistry in the containment of a nuclear reactor in case of a severe accident with air ingression. In *Proceedings of Nuclear Energy for new Europe*, 2009.

[25] Z. Hózer, L. Matus, O. Prokopiev, B. Alföldy, and Csordás-Tóth. Escape ruthenium with high temperature air. Technical report, KFKI, Atome nergia Kutatóintézet, 2002.

[26] N. Vér, L. Matus, M. Kunstá, J. Osán, Z. Hózer, and A. Pintér. Influence of fission products on ruthenium oxidation and transport in air ingress nuclear accidents. *Journal of Nuclear Materials*, 396:208–217, 2010.

[27] S.D. Lee, E.G. Snyder, R. Willis, R. Fischer, D. Gates-Anderson, M. Sutton, B. Viani, J. Drake, and J. MacKinney. Radiological dispersal device outdoor simulation test: Cesium chloride particle characteristics. *Journal of Hazardous Materials*, 176(1-3):56–63, 2010.

[28] Z. Prouza, V. Beckova, I. Cespirova, J. Helebrant, J. Hulka, P. Kuca, V. Michalek, P. Rulik, J. Skrkal, and J. Hovorka. Field tests using radioactive matter. *Radiation Protection Dosimetry*, 139(4):519–531, 2010.

[29] F. T. Harper, S. V. Musolino, and W. B. Wente. Realistic radiological dispersal device hazard boundaries and ramifications for early consequence management decisions. *Health Physics*, 93(1):1–16, 2007.

[30] A. Barto, Y.J. Chang, K. Compton, H. Esmaili, D. Helton, A. Murphy, A. Nosek, J. Pires, F. Schofer, and B. Wagner. Consequence study of a beyond-design-basis earthquake affecting the spent fuel pool for a U.S. Mark I boiling water reactor. Technical report, Office of Nuclear Regulatory Research, US Nuclear Regulatory Commission, 2013.

[31] T.E. Collins and G. Hubbard. Technical study of spent fuel pool accident risk at decommissioning nuclear power plants. Technical Report NUREG-1738, ISTP report 141, 2001.

[32] IAEA. Health and environmental aspects of nuclear fuel cycle facilities. Technical report, IAEA, 1996.

[33] Nuclear Regulatory Commission Office of Nuclear Regulatory Research. Spent fuel pool beyond-design-basis earthquake consequence study. In *Regulatory Information Conference (RIC)*, 2014.

[34] A. Dykes and A. Machiels. Criticality risks during transportation of spent nuclear fue:l revision 1. Technical report, EPRI, Electric Power Institute, 2008.

[35] M. A. Molecke, J.E. Brockmann, D.A. Lucero, M. Steyskal, and M.W Gregson. Spent fuel sabotage test program, surrogate and fission product aerosol results. In *47th Annual Meeting of the INMM*, number SAND2006-5556C, Paper 116, 2006.

[36] M. A. Molecke, J. E. Brockmann, L. A. Klennert, M. Steyskal, M. W. Gregson, W. Koch, O. Nolte, W. Brücher, G. G. Pretzsch, B. A. Autrusson, and O. Loiseau. Spent fuel sabotage testing: depleted uranium oxide aerosol results. *Packaging, Transport, Storage and Security of Radioactive Material*, 19(2):95–101, 2008.

[37] C. S. Viswanadham, K. C. Sahoo, T. R. G. Kutty, K. B. Khan, V. P. Jathar, S. Anantharaman, A. Kumar, and G. K. Dey. Laser pulse heating of nuclear fuels for simulation of reactor power transients. *Pramana - Journal of Physics*, 75(6):1267–1272, 2010.

[38] W. A. Zanotelli, G.D. Miller, and E.W. Johnson. Aerosol characterization from a simulated HCDA : 1979 annual report. 1981. NUREG/CR-2109, MLM-2790, R7 Accessed from http://www.osti.gov/bridge/servlets/purl/972223-KyjlCP/972223.pdf.

[39] P. D. W. Bottomley, T. Wiss, A. Janssen, B. Cremer, H. Thiele, D. Manara, M. Scheindlin, M. Murray-Farthing, P. Lajarge, M. Menna, D. Bouexiére, and V. V. Rondinella. Characterisation of high temperature refractory ceramics for nuclear applications. *IOP Conference Series: Materials Science and Engineering*, 32(1): 012003, 2012.

[40] F. De Bruycker, K. Boboridis, P. Poeml, R. Eloirdi, R. J. M. Konings, and D. Manara. The melting behaviour of plutonium dioxide: A laser-heating study. *Journal of Nuclear Materials*, 416(1-2):166–172, 2011.

[41] D. Manara, M. Sheindlin, W. Heinz, and C. Ronchi. New techniques for high-temperature melting measurements in volatile refractory materials via laser surface heating. *Review of Scientific Instruments*, 79(11):113901–7, 2008.

[42] M. Sheindlin, D. Staicu, C. Ronchi, L. Game-Arnaud, B. Remy, and A. Degiovanni. Experimental determination of the thermal conductivity of liquid UO_2 near the melting point. *Journal of Applied Physics*, 101(9):093508–9, 2007.

[43] K.H. Leitz, B. Redlingshöfer, Y. Reg, A. Otto, and M. Schmidt. Metal ablation with short and ultrashort laser pulses. *Physics Procedia*, 12, Part B(0):230 – 238, 2011.

[44] Y. Di Maio, J.P. Colombier, P. Cazottes, and E. Audouard. Ultrafast laser ablation characteristics of pzt ceramic: Analysis methods and comparison with metals. *Optics and Lasers in Engineering*, 50(11):1582 – 1591, 2012.

[45] Y. Ren, C.W. Cheng, J.K. Chen, Yuwen Zhang, and D.Y. Tzou. Thermal ablation of metal films by femtosecond laser bursts. *International Journal of Thermal Sciences*, 70(0):32 – 40, 2013.

[46] S. K. Friedlander. *Smoke, Dust, and Haze: Fundamentals of Aerosol Dynamics*. Oxford University Press, 2 edition, 2000.

[47] R. S. Windeler and S. K. Friedlander. Nanometer particles and their agglomerates. *Journal of Aerosol Science*, 27(4):645, 1996.

[48] R. S. Windeler, S. K. Friedlander, and K. E. J. Lehtinen. Production of nanometer-sized metal oxide particles by gas phase reaction in a free jet. I: Experimental system and results. *Aerosol Science and Technology*, 27(2):174–190, 1997.

[49] R. S. Windeler, K. E. J. Lehtinen, and S. K. Friedlander. Production of nanometer-sized metal oxide particles by gas phase reaction in a free jet. II: Particle size and neck formation-comparison with theory. *Aerosol Science and Technology*, 27(2): 191–205, 1997.

[50] R. S. Windeler, K. E. J. Lehtinen, and S. K. Friedlander. Production of nanometer-sized metal oxide particles by gas phase reaction in a free jet. *Journal of Aerosol Science*, 26, Supplement 1:S859–S860, 1995.

[51] M. K. Wu, R. S. Windeler, C. K. R. Steiner, T. Boers, and S. K. Friedlander. Controlled synthesis of nanosized particles by aerosol processes. *Aerosol Science and Technology*, 19(4):527–548, 1993.

[52] L. Zhang, M.B. Ranade, and J.W. Gentry. Synthesis of nanophase silver particles using an aerosol reactor. *Journal of Aerosol Science*, 33:1559–1575, 2002.

[53] W. D. Reinhart, T. F. Thornhill, L. C. Chhabildas, W. G. Breiland, and J. L. Brown. Temperature measurements of expansion products from shock compressed materials using high-speed spectroscopy. *International Journal of Impact Engineering*, 35:1745–1755, 2008.

[54] R. Simpson, L. Fried, F. Ree, and J. Reaugh. Unraveling the mystery of detonation. *Science and Technology Review*, June:12–18, 1999.

[55] L.L.N Guariero and A.L.N Guarieiro. *Biofuels - Economy, Environment and Sustainability-Chapter 14*. InTech, 2013.

[56] C.W. Bale, P. Chartrand, S.A. Degterov, G. Eriksson, K. Hack, R. Ben Mahfoud, J. Melancon, A.D. Pelton, and S. Petersen. Factsage thermochemical software and database. *Calphad*, 26(2):189–228, 2002.

[57] C.W. Bale, E. Bélisle, , P. Chartrand, S.A. Decterov, G. Eriksson, K. Hack, I.-H. Jung, Y.-B. Kang, J. Melancon, A.D. Pelton, C. Robelin, and S. Petersen. Factsage thermochemical software and databases – recent developments. *Calphad*, 33(2):295–311, 2009.

[58] J.P. Hiernaut, J.Y. Colle, R. Pflieger-Cuvellier, J. Jonnet, J. Somers, and C. Ronchi. A Knudsen cell-mass spectrometer facility to investigate oxidation and vaporisation processes in nuclear fuel. *Journal of Nuclear Materials*, 344:246–253, 2005.

[59] J.P. Hiernaut, P. Gotcu, J.Y. Colle, and R.J.M. Konings. Thermodynamic study of actinides and lanthanides during total vaporisation of a very high burn-up UO_2 fuel. *Journal of Nuclear Materials*, 378:349–357, 2008.

2

RADES AN EXPERIMENTAL SET-UP FOR THE CHARACTERISATION OF AEROSOL RELEASE FROM NUCLEAR AND RADIOACTIVE MATERIALS

F. G. Di Lemma, J.Y. Colle, M. Ernstberger, G. Rasmussen, H. Thiele, and R. J. M. Konings

A new experimental set-up has been developed for the production and characterisation of aerosols from nuclear and radioactive materials. Separate effect of temperature, materials and different atmospheres on the produced aerosols characteristics can be systematically studied. Laser heating technique is used to vaporize the sample, and aerosols are then generated mainly by nucleation/condensation of the formed vapour. Different collection systems have been developed, permitting the use of different substrates and consequently the application of different post-analysis techniques for aerosols characterisation (SEM/EDX, Raman spectroscopy, ICP-MS). The set-up permits to study the chemistry acting in aerosol formation processes, thanks to the control of the experiments atmosphere and temperature. The set-up has been tested for different materials, such as ceramic, salts and metals, and proved to be feasible for the production, collection and post-analyses of aerosols. Moreover the set-up is set in a glove box, and suitable for test with radioactive and nuclear materials. In this chapter the set-up will be described, focusing on the instrumentation applied, on the post analysis techniques and on the experimental procedure. Finally also examples of the results obtained will be given.

Parts of this chapter have been published in Journal of Aerosol Science **40**, 39-46 (2014) [1].

2.1. INTRODUCTION

Evaluation of the source term (the quantitative assessment of radioactive release) is of main importance for risk assessment and emergency response in case of accidents or sabotages involving radioactive and nuclear materials (RDE's, Radiological Dispersion Events). Following the $9/11^{th}$ terrorist attack in the U.S., an increased focus has been posed on the threat of terrorist attacks. After this event attention has been focused on the consequences of "dirty bombs" detonation (these are bombs created by coupling a conventional explosive with highly radioactive material, a.k.a. RDD's). Studies for the estimation of doses and health consequences following a dirty bombs have been conducted applying different modelling and simulation codes [2–5]. However, as also reported by Andersoon et al. [6], there is needs for better description of the source term, as these codes are highly sensitive to the input parameters. To calculate the impact on the population of a RDE the quantification of the release (total material mass and activity) and its description (size distribution, chemical composition, isotopic composition and partition) is necessary. In order to obtain these data and to generalize the results to different case scenarios, a deep understanding of the aerosol formation process and of the parameters influencing the aerosol characteristics is needed. In the view of this we have developed an experimental set-up with the following goals:

- the production aerosols (from also radioactive materials) by a laser heating technique;
- the characterisation of the aerosols (describing the size distribution, chemical composition and elemental partioning);
- the study of the separate effects of different variables on the aerosol formation (e.g. materials properties, environment and temperature transients);
- understanding the chemical reactions between the gaseous precursor and the chosen environment.

The use of laser heating intends to mimic aerosols generation by a dirty bomb explosions, as the vapour is formed by a rapid high temperature transients and then subject to a very sharp reduction in temperature, due to a cold gas flow. It is not intended however with our set-up to provide a complete simulation of RDD's for which large scale studies have already been performed [7, 8]. Laser heating has been previous applied for production of radioactive aerosols [9], but in the frame of severe nuclear reactor accidents, and also for the production of metallic and ceramic particles (e.g. [10–12]).

2.2. EXPERIMENTAL SET-UP

A scheme of the RADES set-up (Radiological Dispersion Events Set-up) is presented in Figure 2.1. This set-up fulfills the need on one hand of controlling the temperature transients by applying a controlled heating laser pulse to sample materials, on the other hand of controlling the cell experimental environment (choosing the gaseous atmosphere and pressure for each experiment); and finally it permits the collection of the aerosols on different substrates, permitting subsequently the application of a wide range of different post-analysis techniques.

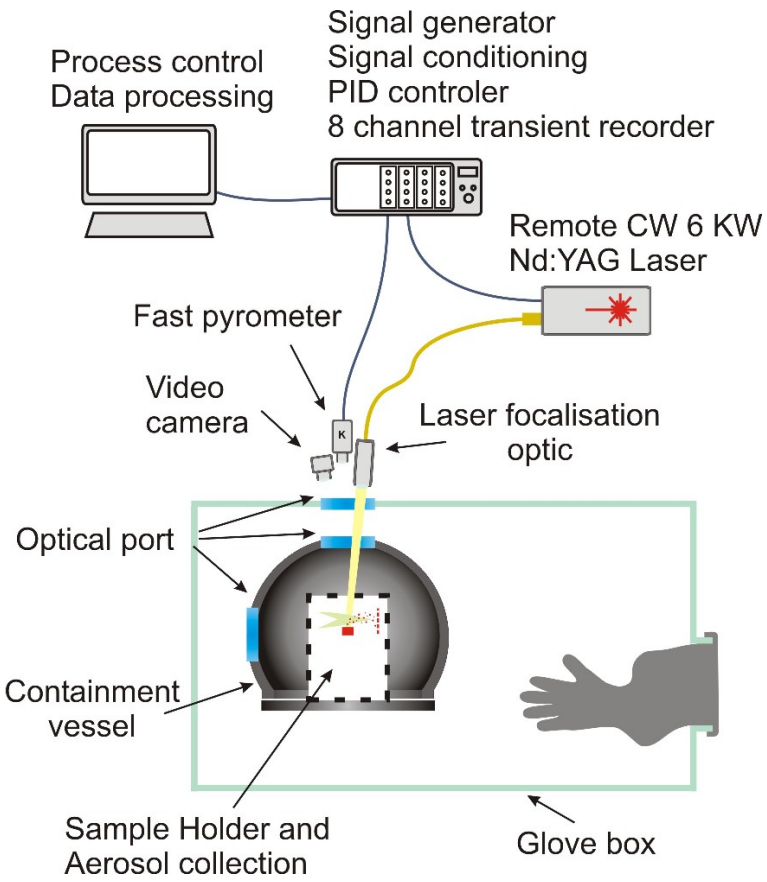

Figure 2.1: A simplified scheme of the experimental set-up, showing the pyrometer and the laser optic mounted outside the gloves box, the containment vessel and the connection between the PID controller and the instrumentation. The sample holder and aerosol collection system can be changed to perform different analyses.

2.2.1. INSTRUMENTATION

CONTAINMENT VESSEL AND LASER HEATING

The set-up (shown in Figure 2.1) consist of a metallic spherical vessel of ca. 300 mm in diameter, used as confinement, which is closed at the bottom by a 250 mm diameter blank flange fixed with screws. The complete set-up is placed in a glove box for testing also nuclear materials. The vessel can be evacuated by vacuum pump (BOC Edwards XDS-5) and filled with different gases. The vessel is further equipped with several (63 mm diameter) flange openings, equipped with windows for visual inspection. These openings are also used for gas inlet and outlet, for the instrumentation and for the laser heating.

The laser beam comes from a remote laser via a 600 μm fiber. The beam is focused with a 150 mm focal length optic giving a 3 mm diameter spot on the sample. As the power distribution profile of the laser spot is fairly square, it gives an homogeneous power distribution on the heated surface. The focusing distance has also been carefully checked in order to have the best power profile (exact focal point). Before interacting with the sample the beam passes through two quartz windows (one on the glove box and the other on the vessel). The sample is positioned horizontally inside the vessel on a support. Energy transfer to the sample can be easily estimated, taking into account the transmittance of the two windows and emissivity of the sample at the laser wavelength. Emissivity values can be taken from literature (e.g. [13]). As an example a calculation for a ceramic material (ZrO_2) lead to ca. 78% energy adsorbed, assuming emissivity ε=0.85 and using for the transmittance of the two window τ=0.956. For the metals energies adsorbed are much lower, due to their higher reflectance, for example for a Mo sample around 30% of laser energy is adsorbed. For more precise simulation of laser heating, in order to obtain temperature profile in the pellet and heat transfers in the system, computer code can be used [14].

The laser used to heat the sample is a TRUMPF Nd:YAG continuous-wave emitting at 1064.5 nm. The laser pulse can be regulated in a very flexible way (with power from 40 to 4500 W, and length from 1 ms to hours). The laser can be controlled by the dedicated software (TIL-WinLas 2.43), which permits to vary manually the parameter during the experiment or to design different pulses (e.g. heating and cooling ramps, square pulse, etc). In order to have a more precise control of the heating shape (a.k.a. sample temperature transient), we can control the laser via analog signal input.

The choice of a laser heating technique, over other available heating techniques (e.g. spark generator, furnace technology, plasma generator) is related to specific experimental requirements, such as:

- avoiding interaction of the sample with supports or heating elements (as laser heating is a self containing system);
- the possibility of avoiding contamination of the heating system when using radioactive materials;

- obtaining a precise and flexible control on the heating transient;
- reaching extreme conditions, such as rapid (tenths of ms) high temperature (up to 4000 K) thermal transients.

TEMPERATURE CONTROLLER

The laser power control is performed by an analog signal input, coming from a fast PID controller (SIM 960 analog controller from Stanford Research System). The PID regulates the power applied by the laser by measuring the difference between the set temperature transients (Set point) and the surface temperature of the sample measured by a pyrometer (Radiance temperature). The output voltage from the PID is connected to the laser control and regulates the power applied by the laser to the sample. The output of the PID is calculated through the following formula:

$$PID(V) = P(e(t) + D\frac{\mathrm{d}}{\mathrm{d}t}\big(e(t)\big) + I\int_0^t e(\tau)d\tau) \tag{2.1}$$

where e is the error calculated as following:

$$e(t) = Measured(t) - SetPoint(t) \tag{2.2}$$

The Set point is generated through a function generator (Function Generator/Arbitrary Waveform Generator HP 33120A from Hewlett-Packard), creating a square voltage pulse, corresponding to the desired thermal transients. The temperature signal measured by the pyrometer is modified before feeding the PID controller. The pyrometer used for high temperature measurements has in fact a logarithmic amplifier, which has a non-linear response with the temperature and thus a always smaller voltage/temperature response at increasing radiance temperature. This makes it difficult to regulate with the same PID parameters the complete temperature range. To respond to this problem a custom analog linearizator electronic was used, this is able to correct the logarithmic amplifier effect, achieving a linear signal/temperature response on the complete temperature range, through the following formula:

$$Lv = A * (Pv + C) + B \tag{2.3}$$

where Lv is the Linearizator output voltage (V) and Pv is the pyrometer output voltage (V). The linearizator output signal is then connected to the PID measure inlet. Furthermore the logarithmic amplifier implemented in the pyrometer is slow for low input signal. To avoid any delay during the increase in temperature, the pyrometer is equipped of a light-emitting diode (LED) lightening the detector and thus generating a "virtual" constant temperature of 1750 K (pyrometer output signal of -3.2 V) which is automatically turned off as soon as the temperature increase over the "virtual" signal. With this system we are able to perform a quasi square temperature pulse, as shown in Figure 2.2.

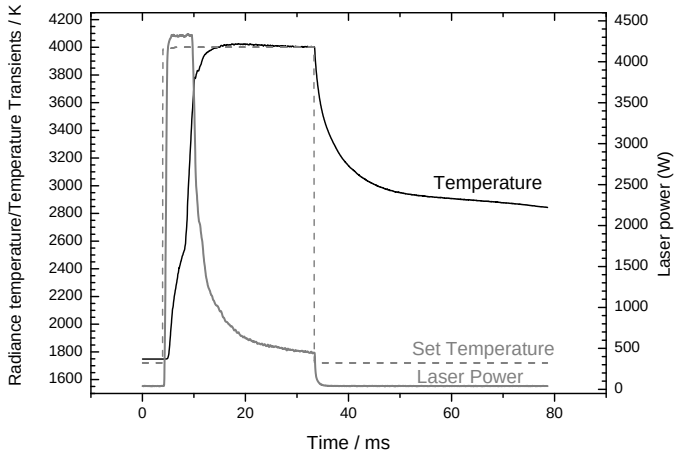

Figure 2.2: Example of the PID temperature regulation performed on a ZrO_2 sample. The parameter used in this experiment are P=7.2, I=200, and D=2*10^4. Rapid heating is achieved thanks to the high power applied in the firsts ms. The sample was heated to 4000 K for 30 ms, the temperature transients (gray dashed line) represent the Set point for the PID controller.

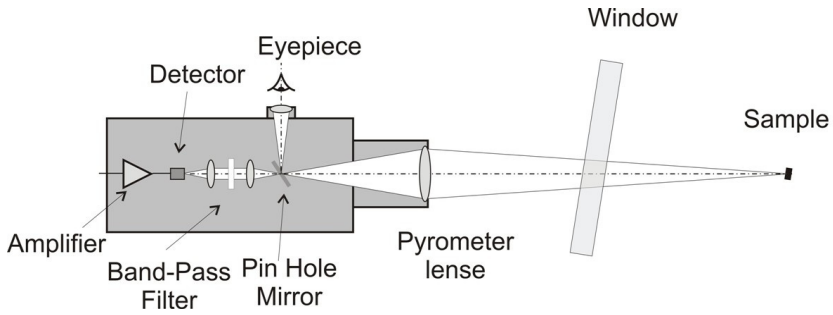

Figure 2.3: A general scheme of the pyrometers applied in our experiments.

TEMPERATURE MEASUREMENTS

For the temperature measurements a pyrometer has been built in house (a scheme is shown Figure 2.3). This pyrometer can be used for high temperature measurements (from 1500 to 4500 K) and consists of a lense focalising on a pinhole mirror. While the pyrometer can be adjusted by an eye piece looking at the image reflected from the mirror, the sample light is filtered by a narrow band-pass filter (10 nm) at 650 nm and detected by a Si-photo-diode, itself connected to a high-speed logarithmic amplifier. It measures the radiance temperature of the sample at effective wavelength 658.56 nm on a spot of 0.5 mm. The pyrometer has been calibrated with two calibrated tungsten ribbon filament strip lamps: one for the low range temperature (1100-1800 K Polaron model Wi22/V Nr.P224c), and the other for calibration at the higher temperatures (1800-2500 K Polaron model Wi22/G Nr.P213c). To avoid any scattered laser light to be detected by the pyrometer, it has been equipped with a holographic Notch filter (from Kaiser Optical Systems, Notch-Plus model for wavelength 1064 nm, diameter 2 inches). Alignment of laser and pyrometer is performed before every experiment in order to measure in the center of the heated spot, the position of the pyrometer is centered with the help of a pilot laser. The signals (e.g. Pyrometer Voltage, Laser Power, PID and Linearizator signal etc.) are recorded by a transient recorder (LTT-184 Labortechnik Tasler GmbH up to 16 bits and 20 MHz) controlled by Lab-View software.

AEROSOL COLLECTING SYSTEMS

Different systems to collect the produced aerosols have been developed. The first (shown in Figure 2.4) is a simple collector, consisting of a metallic horizontal tube of 22.4 mm internal diameter equipped with a circular opening of 19 mm diameter drilled on the upper part for introducing the sample and for the laser beam to interact with it. At the end of the tube a plastic holder is connected to support the filter substrates of 47 mm diameter, which is kept in vertical position by the filter holder. The second system used (presented in Figure 2.5) consists of an U-Tube structure of internal diameter 27 mm, equipped with a circular opening of 25.5 mm diameter drilled in the horizontal part of the U-tube for the interaction of the laser beam with the sample. On the outlet vertical tube, different flanges permit the positioning of a 27 mm filter on a grate filter support in different positions. This variable position of the filter has been shown to be necessary during preliminary test with CsCl, which showed that to perform an effective collection on complete solidified particles a longer path is required, in order to cool and condense the aerosols, as the melting temperature of this material is low. Filters used in both systems were Millipore polycarbonate filters with pores diameter of 0.1-0.2 μm.

The last system (shown in Figure 2.6) consists of a MOUDI impactor (from MSP Corporation model 110R-MRD371), which collects the particles on dedicated substrates (in our application disks of aluminum foil of 47 mm diameter), separating them on 8 different stages by their Aerodynamic Equivalent Diameter (AED, Table 2.1 presents the nominal cut-off size for the different impactor stages). The MOUDI impactor acts through inertia phenomena to separate the agglomerated particles, which requires that a particular flow (30 l/min) is set and controlled. We have therefore connected

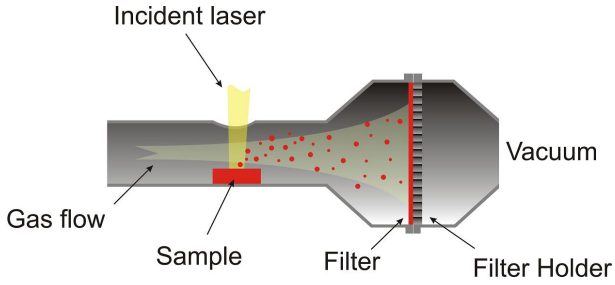

Figure 2.4: Scheme of the simple aerosol collection system. Showing the horizontal tube in which the sample is positioned and the vertical filter holder positioned at the end of the tube.

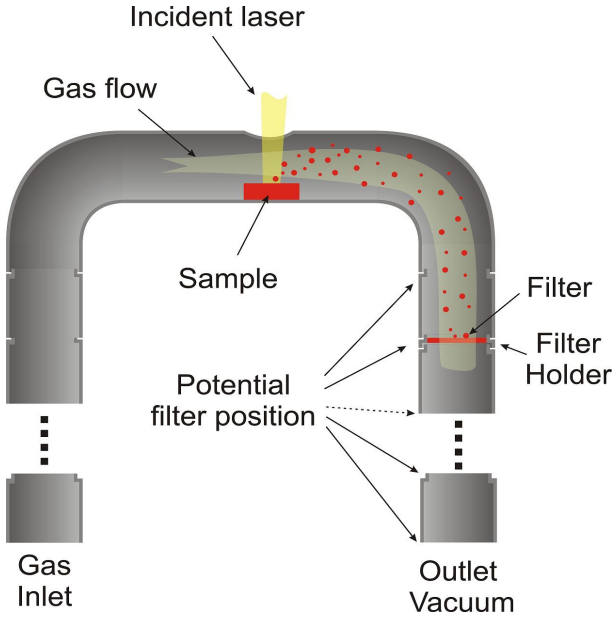

Figure 2.5: Scheme of the U-tube aerosol collection system, built to collect the aerosols of material with low temperature melting point. The different positions of the filter permit different (shorter or longer) paths before the collection, in order to achieve solidification of the particles.

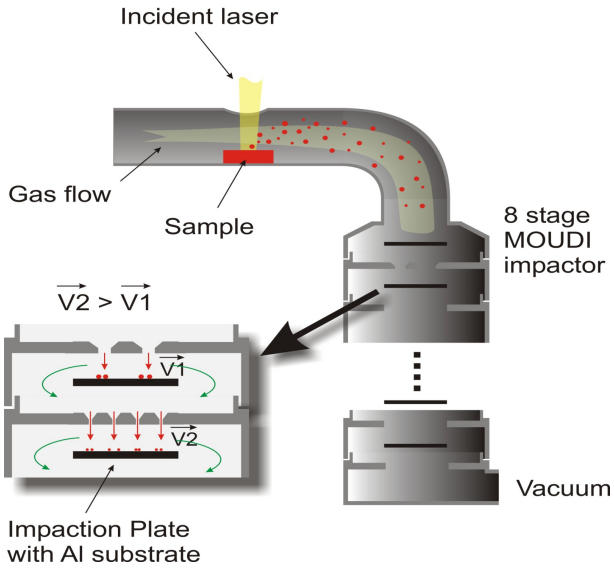

Figure 2.6: Scheme of the aerosol collection system, permitting through the MOUDI impactor the collection of the particles in 8 different size ranges of AED, as shown in Table 2.1 and on Al substrates.

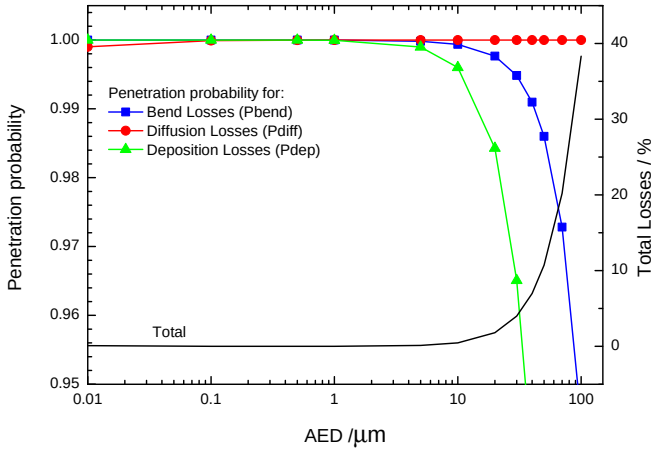

Figure 2.7: Aerosol losses in the L-tube collection system, calculated for standard conditions, for a 30 l/min laminar flow before entering the MOUDI impactor. Formula used are presented in Appendix A.

a flow-meter (Thermal Mass Flowmeter Model 4043 TSI Instruments). When using the MOUDI collection system the sample is posed in a L-tube of 22.5 mm internal diameter with a drilled opening of 12.25 mm diameter on the horizontal part, for the laser beam interaction. The flow necessary for the collection of the aerosols is generated, for all the three systems, by a pressurized inlet and a vacuum pump (BOC Edwards XSD-5) connected to the outlet.

The flow is set at 30 l/min, which corresponds in our different tubing systems to a velocity between 0.87-1.27 m/s. Stripping of the formed liquid layer should be excluded due to the low Weber numbers, which are two orders of magnitude smaller than 1 [15]. Aerosols losses in the tubing have also been calculated taking in account diffusion and inertia phenomena, and including the bends present. The losses account for less than 1% for particles smaller than 10 μm AED. The influence of deposition losses (in the bend and sedimentation in the tube) becomes relevant just for particles over 10 μm AED. These bigger particles (>10 μm) are, however, of less interest for health consequence related to a radioactive release. An example of the calculations applied and results are reported in Figure 2.7 for the last collecting system (L-Tube) and the formula used are shown in Appendix A. Furthermore a vertical system (shown in Figure 2.8), consisting of a 22.5 mm diameter tube with a small sample holder (diameter 5 mm) in the middle, has been constructed and tested to confirm losses in the bend. The results did not show significance discrepancy. Finally a CCD Camera (JVC TK-C1380) can be used to visualize the shot and to record a video of the experiment.

Table 2.1: Cut-off sizes for the MOUDI 100-371R impactor, nominal cut-off size is reported by the user guide for a flow of 30 l/min.

Stage	Nominal Cut-off Size (μm)
Inlet, 0	18
1	10
2	5.6
3	3.2
4	1.8
5	1.0
6	0.56
7	0.32
8	0.18

2.2.2. EXPERIMENTAL PROCEDURE

The samples tested are in the form of pellets. They must be at least 4 mm in diameter due to the dimension of the laser beam and to retain the molten material created during the laser shot. Their thickness can be minimized to a few mm as the interaction depth of the laser is small, the molten area extending typically less than 500 μm in depth. The system is self-containing avoiding the interaction of the material with the supports, as the molten region is contained in the pellets itself. The pellet is then posi-

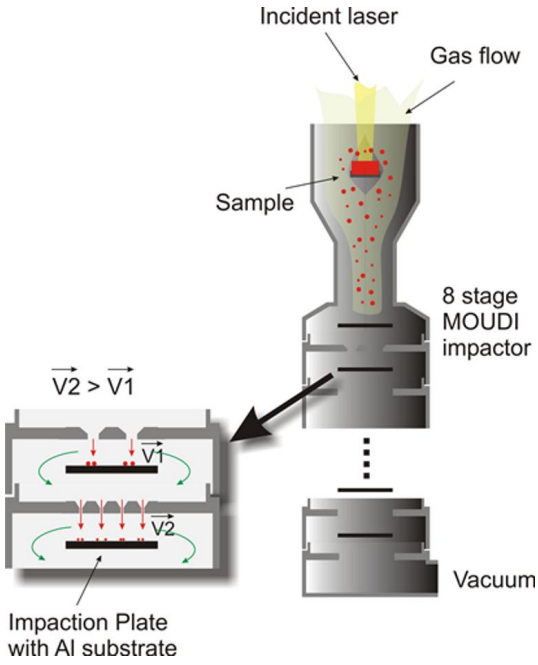

Figure 2.8: Scheme of the vertical aerosol collection system used to avoid losses in the bends.

tioned on the support, and the conditions of the test are chosen (temperature, gaseous atmosphere). The thermal transient is set as input to the PID controller through the function generator, the atmosphere in the cell is selected through the inlet connection, and the flow is then set to 30 l/min. The gas flow is at room temperature in these experiments, leading to a cold flow over the sample. Once the conditions are set the experiments are performed for the different collection systems with identical conditions. The filters and impactor stages are collected for post analyses, the sample as well may be analyzed before and after the test. This is done to obtain a better understanding of the reaction occurring during the experiments. In particular phenomena could be observed on the laser melted surface, such as changes in the sample composition and crystal structure, as well as segregation effects.

2.3. POST ANALYSES & RESULTS

Different post analyses techniques have been applied in order to perform a full characterisation of the collected aerosols (SEM/EDX, Raman Spectroscopy, ICP-MS). The techniques and the instrumentation performance have been tested on a wide range of different material classes, including metals (Co, W, Ta, Mo), salts (CsI, CsCl) and ceramics (ZrO_2). This has been carried out with the aim of proving the feasibility of the set-up for both the production and the characterisation of aerosols. In this section we will present the main results obtained by the application of the different post-analysis

techniques for the different material classes.

2.3.1. SIZE DISTRIBUTION BY SEM/EDX

Scanning Electron Microscope (by a SEM Vega Tescan model TS5130LSH or a FEI Philips XL 40) has been used on the filter substrates to analyse the size distribution of the collected particles. This has been also coupled with Energy Dispersive X-ray spectroscopy (EDX, using the same machines) to obtain also informations on the elemental composition of the aerosols. Some limits for the EDX measurements are however related to the interference of the polycarbonate filters, in particular for oxygen detection. This is due to the small dimension of the particles, which are usually smaller than the interacting electron beam depth, leading to interaction of the beam not only with the particles, but also with the substrate and not permitting a good quantitative analysis of certain elements. SEM and EDX analysis can be performed on the impactor plates as well, bringing some advantages and disadvantages. The particles are in fact collected on the aluminium substrates preferentially in the region below the nozzle position. This higher concentration of particles in one region and the use of the aluminium substrates permits on one hand a better elemental analysis through EDX (minimizing the beam interaction with the collecting substrate), on the other hand, due to a more extensive agglomeration of the particles, primary geometric particle diameter determination through SEM analysis results to be more difficult. Moreover it is not possible to analyse separately the aerosols in an agglomerate, losing information on differences between the particles.

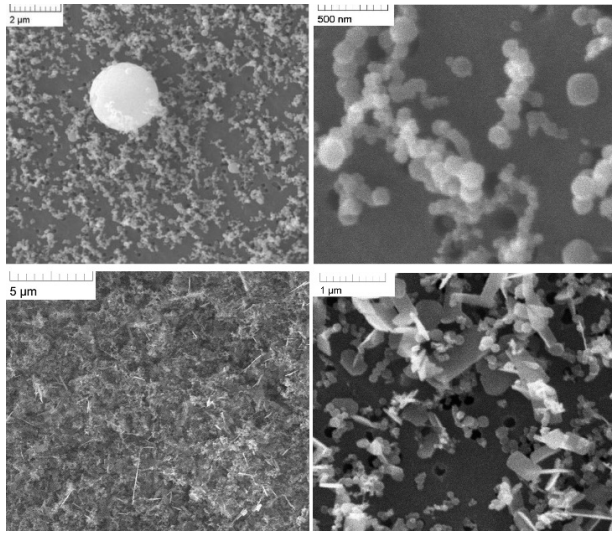

Figure 2.9: Examples of aerosols collected from metals. On top aerosols from a cobalt specimen: on the left micrometer sized spherical particles, on the right an example of agglomerated nanometric aerosols (collected on a filter substrate). On bottom aerosols from a Mo specimen, which have a high degree of agglomeration, and different shapes aerosols: spherical aerosols; and rectangular plates.

METALS

Extensive tests have been conducted on metals (Co, Mo, Ta), materials for which reliable thermal-physical properties are available, in order to analyse which variables influence aerosols characteristics. Some examples of the results from the SEM analyses on aerosols collected on filters (using the simple collector system) for the different materials are shown in Figure 2.9. Differences can already be noticed between materials of the same class. Here we analyse the differences between Mo and Co aerosols.

Mo gives mostly rise to aerosols in the form of rectangular plates (of ca. 1 μm length and 500 nm wide) due to strong recrystallization, also agglomerates of spherical particles were found, with a primary particle diameter ranging from μm to hundreds of nm. Moreover the aerosols for this specimen were collected in high amount both in air and Argon atmosphere, this is due to its comparable vapour pressure both in metallic and oxides form.

On the other hand for the Cobalt we were able to collect aerosols only when the experiments were conduct in air. In those experiments in fact the reaction of the Cobalt with air created oxides of higher volatility with respect to the metallic form. These aerosols could be divided in two classes by SEM analyses: the first includes spherical individual particles of a few μm diameter; the second instead are smaller particles in the nanometer range (50-300 nm). These last are found as agglomerates in fractal like structures (shown in Figure 2.9). The hypothesis on the formation process for these particles is that the smaller nanometric particles are formed by rapid condensation of the vapour, while the micrometer sized particles may originate from the liquid matrix, expelled by a mechanical shock wave induced by the laser impact or by shear force on the liquid surface. This hypothesis has also been proposed by Harper et al. [7] and Lee et al.[8], who suggested that the bigger micrometer particles are related to mechanical phenomena, while the smaller may be related to vapour condensation.

Finally from the EDX conducted on the aerosols and also on the melted laser area it was shown that oxides were formed, for both samples when the experiment were conducted in air atmosphere. From the experiments with Tantalum pellets finally, it was not possible to collect aerosols, this can be related to its low vapour pressure both in its metallic and oxide form.

SALTS

For the tested "salts" (CsCl and CsI, shown in Figure 2.10) individual spherical particles of 200-600 nm diameter were observed. Explanation of their formation can be derived by the theory of coalescence and collision rates from Friedlander [16]. "Salts" have in fact a lower melting temperature with respect to metals and ceramics. This may have brought the particles to coagulate in bigger individual spherical particles, as the collision time will be longer than than the coalescence time. In which case particles will coalesce almost on contact after collision. These particles, analyzed by EDX, in the majority of cases did not show any deviation from the initial composition of the pellets.

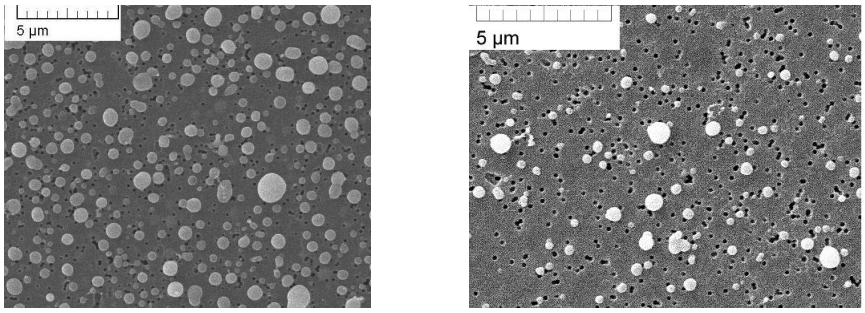

Figure 2.10: Examples of the aerosols collected from salts, CsCl (left) and CsI (right), showing spherical individual particles.

CERAMICS

ZrO_2 pellets were tested for the ceramic material class. For these aerosols (shown in Figure 2.11) similarity was found with the ones created from the Cobalt samples (presented in Figure 2.9). Spherical individual particles of a few μm diameter, and fractal like agglomerates of particles with a primary diameter in the nanometric range (50-300 nm) were detected.

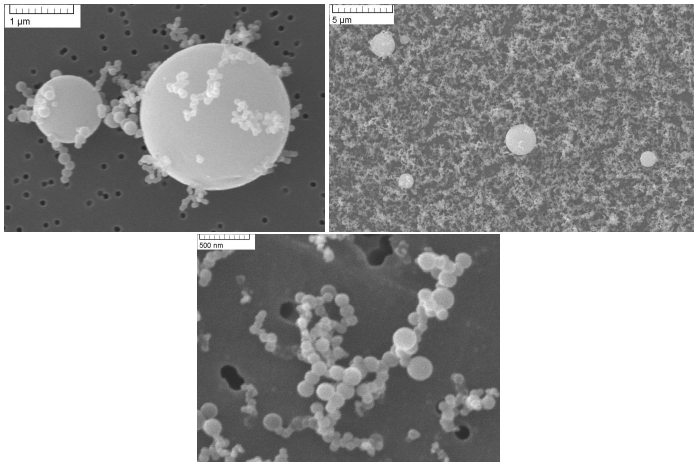

Figure 2.11: Examples of particles collected from a ZrO_2 pellet. On top-left aerosols presenting a fractal-like structure. On top-right micrometer sized spherical particles, which are generally present in a lower number with respect to the nanometer sized particles. They may be related to stochastic effect, such as mechanical shock which can formed due to the expulsion of bigger liquid droplets. On bottom an example of agglomerated nanometric aerosols. Their generation has been related to vapour nucleation/condensation.

Explanation of the formation of fractal-like agglomerates, also in this case, comes from the collision and coalescence theory (as reported by Friedlander [16]). These structures could form during the transport process to the filter, in which the particles

collide and agglomerate without coalescence. In fact ZrO_2 is a high temperature melting material, and as a consequence the particles will rapidly solidify from the vapour, and then collide and attach as agglomerates.

A good explanation of this process is given by Lehtinen et al. [17]: "In the initial stages of particle formation in high temperature gases, a large concentration of very small particles undergoes rapid coagulation. This often leads to fractal-like agglomerates, dendritic structures consisting of a large number of spheroidal primary particles. The size of the primary particles depends on the temperature profile and material properties. At high temperatures, coalescence occurs almost on contact, i.e. the coalescence time is much shorter than the collision time (determining the dimension of the primary particles). As the gas cools, the collision time becomes shorter than the coalescence time, which leads to the dendritic structures." In our system the hot ZrO_2 vapour is rapidly in contact with a cold gas (ca. 300 K), forming the nanometric primary particles by rapid nucleation/condensation, which will then agglomerate in fractal-like structures without coalescence during transport. While for the salts opposite behaviour was observed, as they may have a very rapid coalescence time, bringing the particles to coalesce almost in contact.

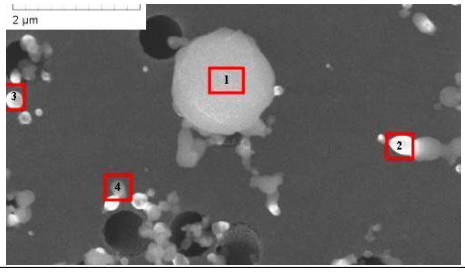

Position	O	Zr	Pd	Cs	I	Ba
1	79.01	14.86	0.64	0.59	0.77	4.14
2	72.13	/	/	14.11	13.76	/
3	76.59	/	/	11.33	12.08	/
4	76.14	/	/	11.39	12.47	/

Figure 2.12: Example of EDX analysis conduct on ZrO_2 with simulated fission products, showing in the smaller nanometric aerosols, the presence of high volatile elements (such as Cs, I) and in the bigger particle element coming form the matrix (such as Zr). All results present in the table are in atomic percent.

A MULTIPHASE MATERIAL

Another set of tests was conducted on simulated spent nuclear fuel pellets. These pellets were obtain by pressing ZrO_2 powder, which was used as a ceramic to replace UO_2, with small quantities of other chemicals (BaO, Pd, CsI), which are typical fission products. These pellets were tested as a first simulation of the fission product behaviour in the aerosols. The aerosols present similar characteristic for size distribution and shape to the one formed from ZrO_2. SEM/EDX analyses (shown in Figure 2.12) showed that

the elements with high volatility (such as Cs and I) are present in higher concentration in the nanometer particles, while the lower volatile elements (e.g. Zr, Ba) are present in higher concentration in the micrometer particles, which have a similar elemental composition to the original pellets. This could confirm our hypothesis on the aerosol formation processes: the bigger micrometer particles may come from mechanical phenomena expelling liquid material, which will lead to a similar elemental composition as to the matrix. The smaller particles instead may be related to vapour condensation, which will lead to enrichment in more volatile compounds.

2.3.2. PHASE AND CHEMICAL IDENTIFICATION BY RAMAN

Raman spectroscopy has been applied in order to analyse the chemical form of the aerosols. These analyses were conducted on the aerosols collected on the aluminium substrates from the MOUDI impactor. It was not possible to perform the Raman analyses on the filters due to the low concentration of particles, the high influence of the complex spectra of the polycarbonate material and fluorescence phenomena.

Raman spectroscopy has proven to be a complementary technique to EDX, the latter provides a quantitative information on the elements present, whereas the Raman provides informations on the chemical form, the oxidation state and crystal modification of the aerosols. A Raman spectrometer (Jobin Yvon T64000 spectrometer) with excitation source Ar^+ or Kr^+ coherent continuous wave laser (emitting at 488 nm and 514.5 nm for the Ar^+ laser, and at 647 nm, and 752 nm for the Kr^+ laser) is used in our experiments. Spectra are measured with a confocal microscope with difference magnification power (10x, 50x, 100x). The device is regularly calibrated with the T_{2g} excitation of a silicon single crystal, set at 520.5 cm^{-1}. Each substrate of the impactor plates is analyzed to evaluate differences in the composition of particles of different AED. Attention should be given to Raman analyses, for which artefacts can be introduce (e.g. coagulation of initial separated particles, partial vaporization of higher volatile elements) due to the Raman laser beam interaction during the measurements. For this reason the power applied and the time of the measurement must be chosen for every different sample material. Studies were conducted on the aerosols from the oxidized metals and ZrO_2 samples, while for the salts it was not possible, as the tested materials are not Raman active.

METALS

For the Mobyldenum and for the Cobalt aerosols, it was possible to observe both the oxidation state and the crystal modification (shown in Figure 2.13). For the Molybdenum aerosols the formation of MoO_3 was observed, mainly in the alpha phase (114, 128, 157, 216, 283, 336, 471, 657, 819, 995 cm^{-1}), as reported in [18]. Also the beta phase was visible, probably as a minor phase as just the more intense peaks were observed (414, 774 , 849, 904 cm^{-1} by comparison with Haro et al.[19]).

For Cobalt to obtain enough material for the Raman analysis we had to perform ten repetitive experiments collecting on the same aluminium substrates. This was due to the smaller amount of aerosols formed for every shot with respect to the

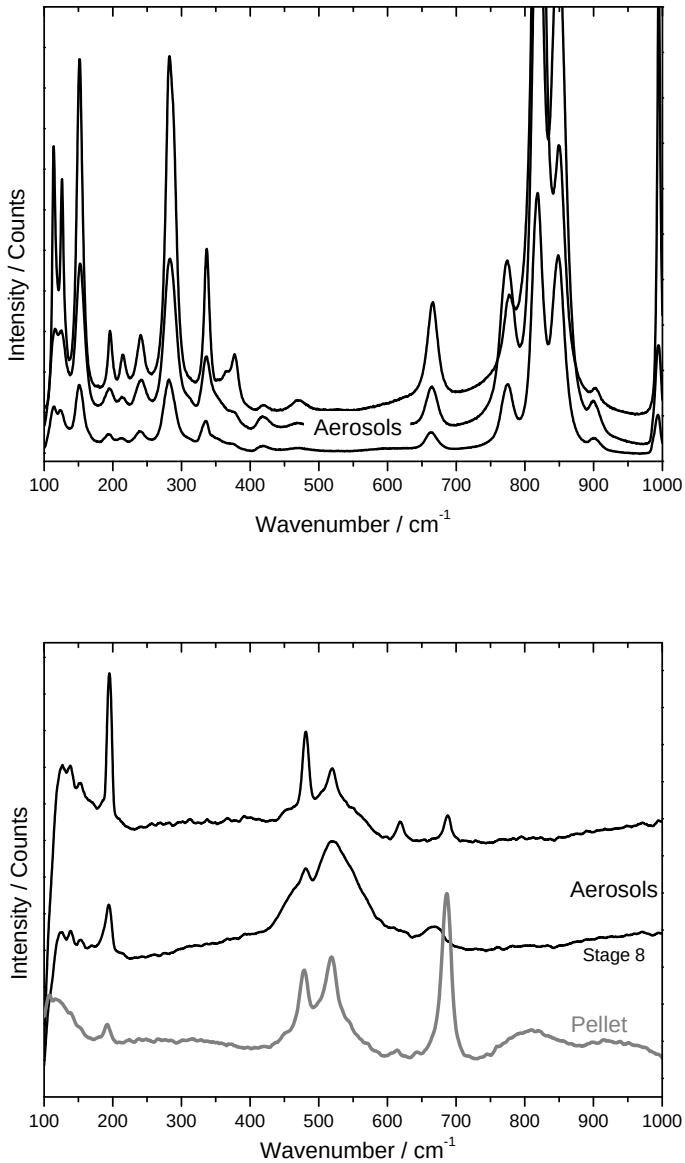

Figure 2.13: Example of Raman analysis conduct on aerosols collected on impactor stages for metals samples evaporated in air atmosphere. Top partiicles from Molybdenum sample, it was here possible to identify the typical peaks of MoO_3. Bottom particles from Cobalt sample, compared to the spectra of the shot pellet.

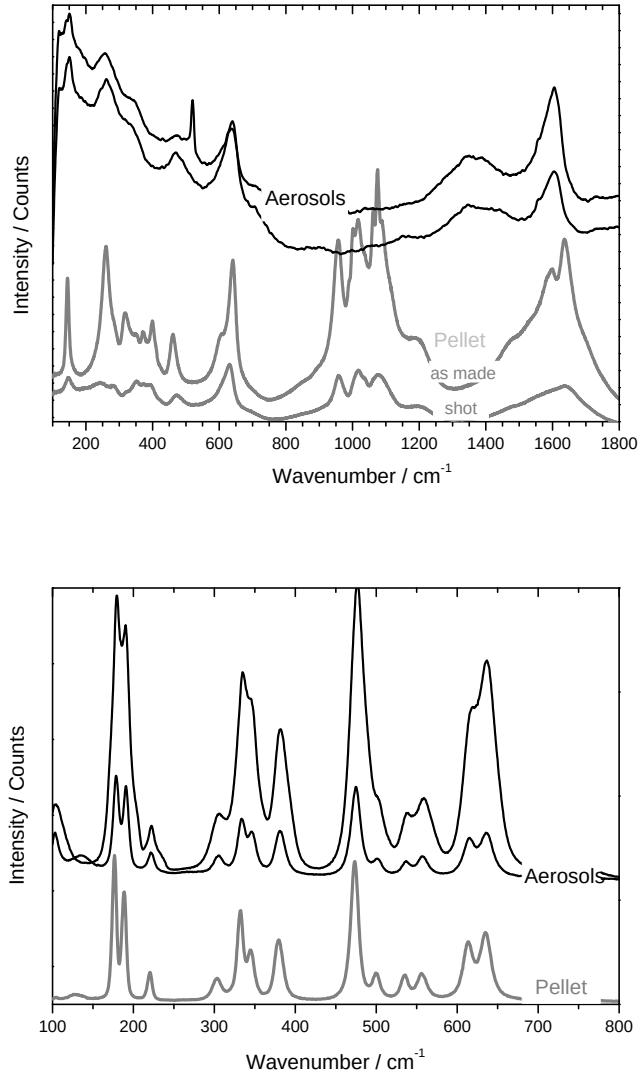

Figure 2.14: Example of Raman analysis conduct on aerosols collected on impactor stages for the ceramic materials. On top the ZrO_2 particles have a cubic phase structure, in contrast to the original pellet which showed a tetragonal structure. Small fraction of the cubic ZrO_2 in the spectra could be also observed on the pellets after the experiment. On the bottom a comparison of the spectra for the aerosols collected and pellet of ZrO_2 with simulated fission products dopants, which shows no visible modification. This demonstrates that Raman is useful to identify the chemical form, on the other hand for small inclusions of the other chemicals difference between aerosols seems not detectable.

Molybdenum experiments, corresponding to the difference in the compounds vapour pressure. The Raman spectra showed the presence of Co_3O_4 aerosols, although on stage 8 the presence also of CoO may be inferred (from the broadening of 488 cm^{-1} peak may be due to 455 cm^{-1} peak, and from the 675 cm^{-1} broad peak, as shown in [20]).

CERAMICS

For the aerosols collected from ZrO_2 pellets we compared the Raman spectra of the material before and after the experiment (shown in Figure 2.14). Even though the peaks for the aerosols are very broad (which may related to the nanometric dimension), it could be noticed that the aerosols and in minor extent the pellets after the shot, show the typical peaks of ZrO_2 in the cubic phase (such as the broad peaks at 600, 1400 and 1600 cm^{-1}), while the pellet, as made, show the peaks of tetragonal phase (e.g. peaks between 800 and 1200 cm^{-1} and double peak at 1600 cm^{-1}). This is due to the fact that the ZrO_2 pellets was stabilized in the tetragonal phase by inclusion of Y_2O_3. During the experiment instead the high temperature reached and the rapid quench will have stabilized the cubic phase. In the shot pellet also a minor part of the surrounding tetragonal ZrO_2 is detected, while for the aerosols the cubic phase seems the main crystal structure.

A MULTIPHASE MATERIAL

Finally for the simulated spent nuclear fuel it was not possible to identify the different chemical species, inserted as simulated fission products (as shown in Figure 2.14). The peaks correspond to the ones of the matrix ZrO_2 itself. Furthermore no big modifications could be seen with respect to the spectra of the starting, which correspond to the ZrO_2 monoclinic phase, as reported in [21].

2.3.3. CHEMICAL COMPOSITION ANALYSIS BY ICP-MS

An other technique applied to analyse the elemental compositions is Inductively Coupled Plasma Mass Spectrometry (ICP-MS), this has shown to be useful when analysing a multiphase material, such as the simulated spent nuclear fuel. For this analysis we produce solutions by washing in ultrasonic bath the aluminium substrates from the impactor, each stage separately (with ca. 20 ml ethanol or water), this permits to have a quantitative information on the fraction of each element present in the different stages, and so to have the elemental distribution also with respect to the AED size. The solutions are then acidified using suprapure grade HF (Merck, Darmstadt, Germany) and Aqua Regia, further purified by sub-boiling in-house and ultra-pure water produced in an UHQ water purifier (USF Elga, Ransbach-Baumbach, Germany). Standards are obtained from certified reference solutions (Inorganic Ventures, Christiansburg, USA and PerkinElmer, Rodgau, Germany) and diluted by weight. The quantification is done by external calibration. Calibration functions and valid measurement ranges for all analyzed elements have been established, furthermore a mixture of all elements to be determined was prepared from certified materials to establish the actual sensitivity for each element. The instrument was optimized for maximum sensitivity and uniform response over the whole mass range. A sequence

of measurements was created including an instrument blank, the standards, a quality control sample, a process blank, the to-measure samples. The standards and each sample are measured in triplicate. Only the most abundant, uninterferred isotope of elements with natural isotopic composition is measured, the resolution required to separate the isotope from interfering peaks was chosen for each isotope. The instrument used is an Element2 (Thermo Fischer Scientific, Bremen, Germany).

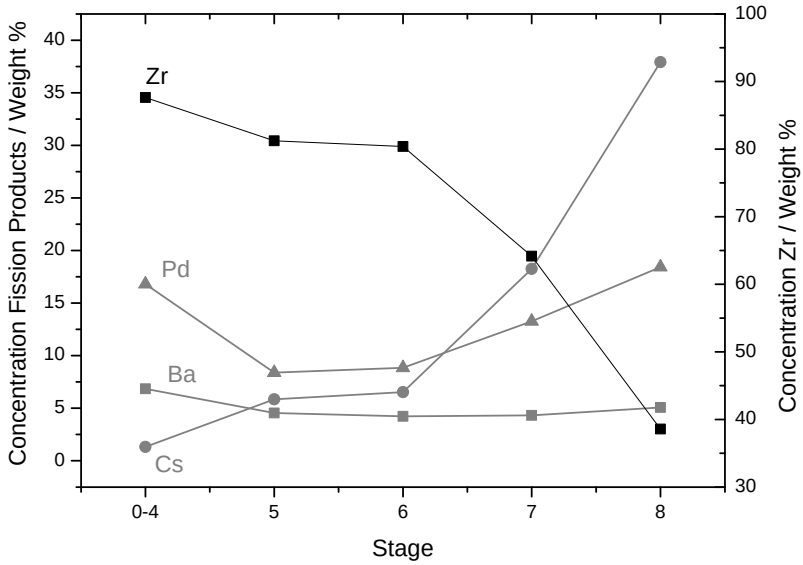

Figure 2.15: Result from the ICP-MS analysis on the aerosol formed from ZrO_2 simulated spent nuclear fuel, showing the mass concentration of each element collected on the impactor stages. It shows that the bigger particles are enriched in Zr (first stages, concentration of Zr to be read on right Y-axis). In the smaller particles, there is instead an increase of the concentration of the higher volatile elements (to be read on left Y-axis).

The results given are total amounts expressed as μg of each trace element per total mass dissolved and the uncertainty stated is the total expanded uncertainty U calculated according to ISO Guide to the Uncertainty in Measurement (GUM) with a coverage factor 2, which corresponds in our experiment to a relative error between 9-13% on the mass of the different elements, and on the composition under 25%. An interesting example of ICP-MS analysis was performed on the aerosol from the ZrO_2 simulated spent nuclear fuel in order to describe the elemental composition of the aerosols. From the analysis we observed that the majority of aerosols are collected on the 6^{th} stage, which has a nominal cut-off size of 560 nm AED. Furthermore by fitting of the total elemental mass pro stage measured by ICP-MS it is also possible to obtain size

distribution of the particles. A log-normal function was assumed, resulting in a AED mean value of ca. 700 nm and a standard deviation of 0.47, with a mode value of ca. 560 nm. For the elemental composition it can be noticed (as shown in Figure 2.15), that the Zr is present as main component in the first stage (circa 95% of the collected mass), its concentration drops down quickly after stage 6 to 40% in the last stage. On the other hand Cs and Pd present an opposite behaviour. This demonstrates that the higher concentration of higher volatile elements is present in the last stages, where the smaller particles are collected. This behaviour was also confirmed by EDX analysis on the aerosols from simulated ZrO_2 spent nuclear fuel collected on filters (Figure 2.12).

2.4. CONCLUSIONS

A new experimental set-up and experimental procedure have been developed for the production, collection and post-analyses of aerosols. The aim of the system is to provide data for the understanding of aerosol formation process and the variables influencing the aerosol characteristic through separate effect tests. Focus is posed on understanding the chemical reactions taking place in the experiments and on the elemental partition in the aerosols.

Production of the aerosol is performed in our set-up by a laser heating technique, which offers the best possibility for controlling the temperature transient and obtaining rapid and high temperature transients. In our set-up furthermore different variables influencing aerosol formation can be controlled (such as the atmosphere, influencing the chemical reaction, and temperature).

Tests have been conducted on different materials (ceramic, metals and salts) showing that the methodology and instrumentation are flexible for the production and collection of the aerosols, and a reliable and large set of data can be obtain from the post-analysis techniques. Since the set-up is built in a glove box it is also suitable for studies with radioactive and nuclear materials.

In the following chapters this system will be applied to study aerosols released from different radiological dispersions scenarios. This will include the study of the aerosols releases from radioactive sources used for commercial application (e.g. nuclear medicine, sterilization industry, etc). These sources are in fact feared to be used by terrorist groups for creating dirty bombs. Finally also studies with simulated spent nuclear fuel will be presented. These had the aim of studying the aerosols characteristics from scenarios, such as sabotage and accidents during transport of spent fuel or uncovering of spent fuel pond.

ACKNOWLEDGEMENTS

I would like to acknowledge the constructive contribution to this work: B. Cremer, K. Mayer, F. Naisse, S. Van Winckel, T. Wiss.

REFERENCES

[1] F.G. Di Lemma, J.Y. Colle, M. Ernsteberger, G. Rasmussen, H. Thiele, and R. J. M. Konings. RADES an experimental set-up for the characterization of aerosol release from nuclear and radioactive materials. *Journal of Aerosol Science*, 70:36–49, 2014.

[2] K. G. Andersson, T. Mikkelsen, P. Astrup, S. Thykier-Nielsen, L. H. Jacobsen, L. Schou-Jensen, S. C. Hoe, and S. P. Nielsen. Estimation of health hazards resulting from a radiological terrorist attack in a city. *Radiation Protection Dosimetry*, 131(3):297–307, 2008.

[3] S. Apikyan, D. Diamond, and V. Reshetin. Estimation of inhalation radiation doses associated with a ^{90}Sr dirty bomb event. In *Countering Nuclear and Radiological Terrorism*, NATO Security through Science Series, pages 143–150. Springer Netherlands, 2006.

[4] J. Magill, D. Hamilton, K. Latzenkirchen, M. Tufan, G. Tamborini, W. Wagner, V. Berthou, and A. von Zweidorf. Consequences of a radiological dispersal event with nuclear and radioactive sources. *Science & Global Security*, 15(2):107–132, 2007.

[5] H. Shin and J. Kim. Development of realistic RDD scenarios and their radiological consequence analyses. *Applied Radiation and Isotopes*, 67(7-8):1516–1520, 2009.

[6] K. G. Andersson, T. Mikkelsen, P. Astrup, S. Thykier-Nielsen, L. H. Jacobsen, S. C. Hoe, and S. P. Nielsen. Requirements for estimation of doses from contaminants dispersed by a dirty bomb explosion in an urban area. *Journal of Environmental Radioactivity*, 100(12):1005–1011, 2009.

[7] F. T. Harper, S. V. Musolino, and W. B. Wente. Realistic radiological dispersal device hazard boundaries and ramifications for early consequence management decisions. *Health Physics*, 93(1):1–16, 2007.

[8] S.D. Lee, E.G. Snyder, R. Willis, R. Fischer, D. Gates-Anderson, M. Sutton, B. Viani, J. Drake, and J. MacKinney. Radiological dispersal device outdoor simulation test: Cesium chloride particle characteristics. *Journal of Hazardous Materials*, 176(1-3):56–63, 2010.

[9] W. A. Zanotelli, G.D. Miller, and E.W. Johnson. Aerosol characterization from a simulated HCDA: 1979 annual report. 1981. NUREG/CR-2109, MLM-2790, R7 Accessed from http://www.osti.gov/bridge/servlets/purl/972223-KyjlCP/972223.pdf.

[10] K.-H. Leitz, B. Redlingshöfer, Y. Reg, A. Otto, and M. Schmidt. Metal ablation with short and ultrashort laser pulses. *Physics Procedia*, 12, Part B(0):230 – 238, 2011.

[11] Y. Ren, C.W. Cheng, J.K. Chen, Yuwen Zhang, and D.Y. Tzou. Thermal ablation of metal films by femtosecond laser bursts. *International Journal of Thermal Sciences*, 70(0):32 – 40, 2013.

[12] Y. Di Maio, J.P. Colombier, P. Cazottes, and E. Audouard. Ultrafast laser ablation characteristics of PZT ceramic: Analysis methods and comparison with metals. *Optics and Lasers in Engineering*, 50(11):1582 – 1591, 2012.

[13] Y. S. Touloukian and D. P. DeWitt. *Thermal radiative properties: metallic elements and alloys*. IFI/Plenum, volume 7 of thermal radiative properties edition, 1970.

[14] M.J. Welland, B.J. Lewis, and W.T. Thompson. A comparison of stefan and phase field modeling techniques for the simulation of melting nuclear fuel. *Journal of Nuclear Materials*, 376(2):229–239, 2008.

[15] S.P. Lin. *Breakup of Liquid Sheets and Jets*. Cambridge, first edition, 2003.

[16] S. K. Friedlander. *Smoke, Dust, and Haze: Fundamentals of Aerosol Dynamics*. Oxford University Press, 2 edition, 2000.

[17] K. E. J. Lehtinen, R. S. Windeler, and S. K. Friedlander. Theory of the onset of dendrite formation. *Journal of Aerosol Science*, 26(1001):51–52, 1995.

[18] G. A. Nazri and J. Julien. Far-infrared and raman studies of orthorombic MoO_3 single crystal. *Solid State Ionic*, 53-56:376–382, 1992.

[19] E. Haro-Poniatowskia, M. Jouanneb, J.F. Morhangeb, C. Julienb, R. Diamanta, M. Fernández-Guastia, G.A. Fuentesa, and J.C. Alonso. Micro-raman characterization of WO_3 and MoO_3 thin films obtained by pulsed laser irradiation. *Applied Surface Science*, 127-129:674–678, 1998.

[20] C. W. Tang, C. B. Wang, and S.H. Chien. Characterization of cobalt oxides studied by FT-IR, Raman, TPR and TG-MS. *Thermochimica Acta*, 473:68–73, 2008.

[21] G.G. Siu, M. J. Stokes, and Y. Liu. Variation of fundemental and higher-order raman spectra ZrO_2 nanograins with annealing temperature. *Physical Review B*, 59 (4):3173–3179, 1999.

3

CHARACTERISATION OF AEROSOLS FROM RDD SURROGATE COMPOUNDS PRODUCED BY FAST THERMAL TRANSIENTS

F.G. Di Lemma, J.Y. Colle, M. Ernstberger, and R.J.M. Konings

Experimental tests have been performed to characterize the aerosols representative for Radiological Dispersion Devices (RDD's, a.k.a. "dirty bombs") by applying to chosen surrogate compounds rapid high temperature transients, vaporizing the sample and forming aerosols mainly by rapid cooling of the vapour. The materials, which were tested in their non-radioactive form, have been chosen from the radioactive sources widely used in industries and nuclear medicine applications. Our analyses permitted the characterisation of the inhalable fraction of the aerosols released, and the study of the influence of cladding materials on the aerosol release and on its characteristics.

Parts of this chapter have been submitted and accepted for publication by the Journal of Nuclear Science and Technology (currently under revision).

3.1. INTRODUCTION

In the last years "dirty bombs" detonations have been of particular interest for international nuclear security analyses, due to the attention posed on terrorist attacks after $9/11^{th}$. "Dirty bombs" are bombs created by coupling a conventional explosive with a highly radioactive material with the aim of releasing radioactivity in the environment. Terrorist organizations are believed to be interested in such weapons to spread panic among the population and inflict economic damage. It should be emphasized, as reported by many authors (e.g. [1, 2]), that although RDD's do not have the aim of destroying a city or creating a high number of fatalities, they can have an important major long-term effect consisting of an increase of cancer rate mainly related to the inhalation of radioactive particles [2, 3]. To calculate the impact on the population of RDD's the quantification of the release (total mass and activity) and its description (size distribution, chemical composition and isotopic composition) is necessary (a.k.a. source term analyses). As reported by Andersson et al. [4] a better description of the source term is needed, as dispersion calculations are highly sensitive to the input parameters.

In the previous chapter (Chapter 2) we have shown the feasibility of laser heating to vaporize and analyse the aerosols released from different materials. The present study aims at studying the interactions occurring in the vapour phase influencing aerosol formation in the inhalable fraction. This is performed by vaporizing surrogate inactive materials used in radioactive sources that could be misused in RDD's, and by analysing the influence of other components of the radioactive source on the aerosol characteristics. In this particular study we have focused on evaluating the influence of the cladding materials on the aerosols release. These are materials used as containment and shield for the radioactive source, and have a high probability of reacting with the source. Following a detonation the cladding materials and the radioactive source will be partially dispersed in bigger fragments and blown away, while a part "could interact when in the vicinity of the fireball, as it could be entrained into the turbulent eddies within the fireball" [5]. Once in the fireball the material will be vaporized and could chemically interact in the gaseous phase. The tests consisted of separate effect studies, performed for a number of sources (Co, CsCl, Ir, and $SrTiO_3$) using different cladding materials (tungsten, and/or stainless steel). Finally attention has been focused on evaluating the chemical and elemental composition as function of the particles size (measured by AED, Aerodynamic Equivalent Diameter). The AED of particles is an important parameter influencing the aerosol transport behaviour in the environment and the risk associated with the inhalation of the particles.

The influence of other source components and environmental materials on the aerosol release from RDD's has been reported by several authors [5–7]. Lee and coworkers [6] studied the interaction of explosive and soil with a simulated CsCl source and found an effect on the release, such as the formation of mixed aerosols containing both carbonaceous materials and the simulated source material, or a different ratio of Cs and Cl in the aerosols. However, they could not assess the cause of such effects.

Harper et al. [5] tested simulated full-size devices for a wide range of source materials, and concluded that other surrounding materials (such as soil) can interact with the radioactive materials by agglomeration and/or coagulation and affect the size of the "radioactive" particles. Such a complete simulation of a RDD in an integral tests is not the goal of our experiments. The aim of our studies is instead a deeper understanding of the aerosol formation process, the identification of the chemical interactions taking place with other materials, and their influence on the aerosol characteristics, which can be performed in simplified controlled laboratory conditions.

3.2. EXPERIMENTAL

3.2.1. INSTRUMENTATION AND EXPERIMENTAL PROCEDURE

The set-up applied in our study has been described in detail in Chapter 2. In this paper we just summarize its main features for clarification. Fast laser heating is used to vaporize the samples and to form aerosols. With this technique extreme heating transients can be achieved, e.g. reaching temperatures higher than 3000 K, with heating rates higher than 30000 K/s. The vapour formed condenses then rapidly in the colder air environment (at room temperature), forming aerosols. These are collected by different systems and on different substrates, depending on the post-analyses to be performed. By using the MOUDI impactor for the collection of the aerosols it is possible to divide the particles by their AED. This enables us to perform characterisation of the particles as function of their size, and also to obtain their size distribution by weighing the substrates before and after the experiments. SEM/EDX (Vega Tescan model TS5130LSH or a FEI Philips XL 40) was applied for the analysis of the elemental composition, of the morphology and of the geometrical size. Raman spectroscopy (Jobin Yvon T64000 spectrometer) was applied for the identification of the particle phases. Such instruments and their application in our studies have been described in Chapter 2. The sample holder, used in these tests, consisted of a vertical tube in which the sample is posed on a same horizontal support, and the geometry and the distance between the source and collecting substrates were kept constant. This modification, with respect to the sample holder presented in Chapter 2, was performed to avoid aerosol losses in the bends.

Our analyses have shown that a complete simulation of the detonation process is not possible with this set-up, due to the impossibility of controlling and scaling the shock wave in our experiments (e.g. detonation shock waves have an impact pressure up to 450 GPa [8, 9]). However, this system is useful to simulate the process of rapid expanding hot gases involved in the detonation (up to approximately 5500 K in the microsecond range [8, 9]) and to study the gaseous interactions. Following an explosion high temperatures will be reached, which will be volatilize part of the source and of the cladding materials. This hot gases will be ejected in the cooler environment. In this scenario the gas will be in supersaturation conditions and homogeneous nucleation of aerosols will be the dominant process and the contribution of heterogeneous nucleation will be minimal. On the other hand, debris or fragments may act as sinks for the aerosols by agglomeration and producing micrometer particles which will

rapidly settle. The particles produced with our set-up in the nanometric size range have been compared to the results of integral tests by Lee et al. [6] and showed similar features. This suggests that our experimental set-up is able to produce representative aerosols in the nanometric size range, which are formed by homogeneous nucleation from the vapour phase released during dirty bomb detonations.

Moreover fast laser heating reproduced a bimodal aerosol size distribution, as observed also in integral tests [5–7]. Although the fractional release between these two size range cannot reproduce the scenario of a real detonation, the study and comparison of these aerosols can help in understanding the phenomena taking place, and the difference between solid and vaporized phase. The first peak of the size distribution (in the nanometric size range) is generated, as explained also in [10], by the condensation of the high temperature vapour released, followed by their agglomeration. The second peak (in the micrometer size range) has been related to mechanical shock, similarly to what observed in the precedent integral experiments [5–7]. In the integral tests the micrometer size particles were generated by the explosive blast, while in our tests this is related to a stochastic effect generated by the thermal shock on the unmelted brittle pellet or on the produced liquid layer, due to the rapid laser heating. Thus the impossibility to reproduce a real mechanical blast and the pressure encountered in a RDD detonation by the use of laser heating. As a result the quantities of these micrometer particles are representative of the particles ejected by the detonation blast, but by analysing and comparing them to the nanometric particles formed by the vaporization process important information can be derived.

3.2.2. SAMPLES

The materials tested were chosen from the most commonly used radioactive sources and tested in their natural isotopic composition. A list of the sources most commonly feared to be acquired by terrorists to create a RDD is shown in Table 3.1. From these the highest activity and the most available sources were tested. The source materials chosen were Co, CsCl, Ir, and $SrTiO_3$. The samples were pellets of 5 mm diameter, obtained by pressing commercial powders (from Alfa Aesar) by a hydraulic press. For Co also solid disks were tested [10], but no difference was observed for the aerosol characteristics.

Different laser pulses were tested to heat rapidly part of the samples surface. However, for the same conditions applied (square laser pulse 3000 W, lasting 60 ms) the temperature reached on the surface of the tested materials was different. This is due to the different thermodynamic and surface properties of the materials used. Temperature was measured by a rapid high temperature pyrometer, as described in Chapter 2. Finally the amount of material vaporized varied between the different materials tested, ranging from a few mg to tens of mg.

Powder mixtures, containing the cladding materials (tungsten and/or stainless steel) and the simulated source materials to be tested, have been pressed to create the

Table 3.1: Radionuclides of concern for RDD's production (as reported in [11]).

Radionuclide	Typical physiochemical form	Application	Activity
^{60}Co	Metal	Sterilisation irradiator, Nuclear Medicine	up to 400 000 TBq, up to 1000 TBq
^{90}Sr	Ceramic ($SrTiO_3$)	Thermoelectric generator	1000-10 000 TBq
^{137}Cs	Salt (CsCl)	Sterilisation irradiator, Nuclear Medicine	up to 400 000 TBq, up to 1000 TBq
^{192}Ir	Metal	Industrial Radiography	up to 5 TBq
^{226}Ra	Salt ($RaSO_4$)	Nuclear Medicine	up to 5 TBq
^{238}Pu	Ceramic (PuO_2)	Thermoelectric generator	up to 5 TBq
^{241}Am	Pressed ceramic powder (AmO_2)	Well logging source	up to 1 TBq
^{252}Cf	Ceramic (Cf_2O_3)	Well logging source	up to 0.1 TBq

samples for studying the influence of cladding on the radioactive aerosols. Powder mixtures have been chosen to have an quasi-homogeneous composition in the laser shot area because a complete simulation of a full-size source is not possible using our set-up, and the heating of such an inhomogeneous sample could introduce other variables in our studies, such as the preferential vaporization of one of the compounds. To test the influence of the cladding materials different compositions of the mixed compounds have been created, as the variety of commercial radioactive source assemblies prevent to define a unique source composition. We have tested first pellets with equal amount (in mass) of the materials, and subsequently we also tested the influence of an excess of one of the compounds. This was done because the contribution in the vapour phase of cladding and source materials can vary depending on the RDD design, and the explosion characteristics [5].

A summary of the samples tested is presented in Table 3.2. Successive tests on the same material showed that the aerosol characteristics are reproducible under same experimental parameters. Therefore, most experiments were performed once, due to the difficulty of working in a glove box and extensive time necessary for post-analyses.

Table 3.2: Samples tested in our studies, and the cladding materials applied.

Sample	Claddings	Composition (%wt.)
Co	Tungsten	50/50, 30/70;
	Stainless Steel	50/50, 25/75;
	Mixture	33/33/33; 22/71/7
	(Source, W, SS)	
CsCl	Tungsten	50/50, 25/75;
	Stainless Steel	50/50;
	Mixture	33/33/33, 25/50/25.
	(Source, W, SS)	
Ir	Stainless Steel	50/50.
$SrTiO_3$	Tungsten	50/50, 87.5/12.5;
	Stainless Steel	50/50;
	Mixture	33/33/33, 25/50/25.
	(Source, W, SS)	

For the cladding materials, tungsten has been chosen as it is one of the shields applied in nuclear medicine. Stainless steel is applied also in nuclear medicine as a second shield coupled with tungsten, or it is used as unique cladding for metallic sources in sterilization plants or for radiography. The choice of the cladding material to apply in our studies with the difference source was made keeping in mind their application in the industry or in the medical facilities. For example as Co and CsCl are used both in sterilization and medical facilities, the cladding materials tested were both tungsten,

stainless steel and a mixture of the two. Also testing of tungsten alone (without stainless steel) was performed, although this not used in real applications, in order to understand the separate effect of this material on the aerosols characteristics. Finally for $SrTiO_3$, a radioactive source used for thermal generators, a wide range of cladding materials was applied in the past. These consist mainly of a first tungsten or lead shields, followed by a stainless steel container (as reported in [12, 13]). In our tests tungsten and stainless steel were tested as cladding materials, to be consistent with the other tests.

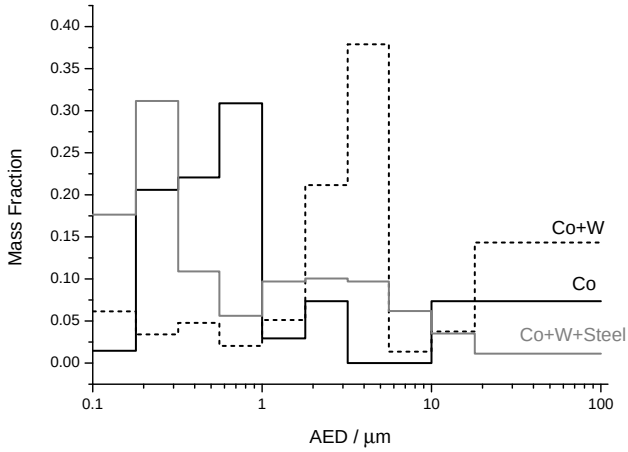

Figure 3.1: Aerosol size distribution for the Co sample and its mixture with the cladding materials, obtained by weighing the MOUDI impactor plates before and after the experiments.

3.3. RESULTS

3.3.1. CO

Results from the test on Co were already presented in Chapter 2 as this was one of the materials applied in the feasibility studies. Here some new results are presented that are important for the source term evaluation. The Co aerosols collected from our experiments show a classical bimodal size distribution (Figure 3.1). A first concentration maximum is found for particles with an AED>10 μm, the other is found around 400 nm. By fitting the first peak of the distribution with a log-normal curve, we obtain for the mean mass diameter μ=780 nm and its standard deviation (σ=680 nm). Applying the MOUDI impactor for the collection of the particles, the particle morphology as function of the AED could be studied (as shown in Figure 3.2). It has been observed that spherical micrometer particles are mainly collected in the first stages (with bigger AED cut-off size, which are seen as the first maximum of the size distribution), while the nano-particle agglomerates are collected in the last stages with smaller AED cut-off

size (which correspond to the peak in the nanometric range).

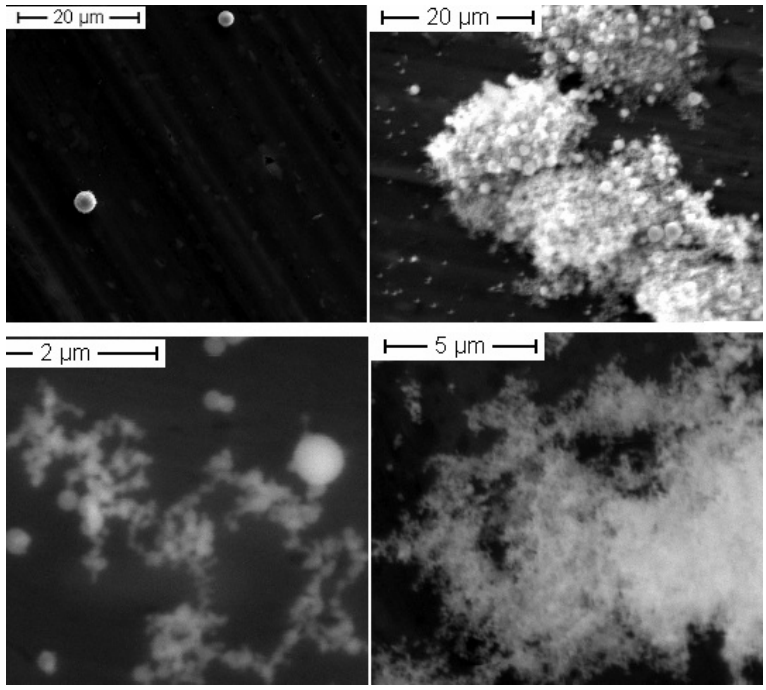

Figure 3.2: Examples of particles from the Co sample. Showing the different type of particles: in the first stages (top-left, with cut off sizes 1.8<AED <18 μm) individual spherical particles were found; in stage 5 (top-right, with a cut off size of AED 1 μm) agglomerated particles were observed (a magnified image of these agglomerates is shown on the bottom-left). The nanometric agglomerates are found finally on the last stages (stage 6-8 as shown in the bottom-right AED<0.56 μm).

This different morphology, as explained, depends on the formation mechanism. The micrometer-sized particles are related to the dispersion of part of the liquid layer due to mechanical forces or shear forces generated by the thermal shock from the rapid laser energy transfer to the melted sample surface. The smaller nanometric particles are formed by a rapid quenching of the vapour released in contact with the colder gaseous environment at room temperature. These particles will not coagulated to form bigger primary particles but will instead agglomerate in complicated structures (fractal-like structures), as explained by Friedlander's theory of collision and coagulation [14]. These agglomerates will then fold on themselves (as shown in Figure 3.4) due to the high number of primary particles.

3.3.2. CO AND THE CLADDING

Post-analyses of the mixed samples showed that the cladding materials did not influence the characteristic morphology of the aerosols. A shift of the peak in the

nanometric size range to bigger size was observed for the sample in presence of tungsten (corresponding in the size distribution to a shift of μ=4.3 μm, with σ=480 nm), as shown in Figure 3.1. This is related to the higher aerosol total mass release observed in this experiment. This higher quantity of vaporized material results in higher agglomeration rates, as an higher concentration of primary particles will be present in the system. As a result agglomerates will be generated, shifting the peak to bigger AED (μ=4.3 μm). These higher total mass release observed in presence of tungsten was caused by the higher vapour pressure of tungsten oxide in comparison to cobalt and its oxides. Moreover tungsten has a strong tendency to oxidation with respect to cobalt, as shown by their Ellingham diagrams, which could enhance the difference in their release.

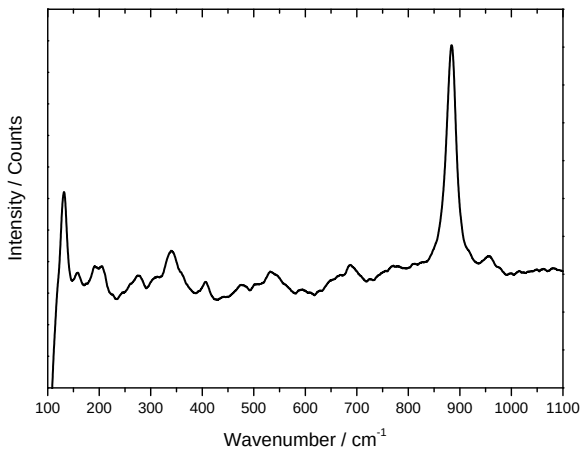

Figure 3.3: Raman spectrum measured for mixed cobalt-tungsten particles. Showing all the typical bands of $CoWO_4$, as reported in [15–17].

The Raman spectroscopy analyses of the nanometric particles (0.18<AED<1 μm indicated also a chemical interaction between tungsten and cobalt (as observed in Figure 3.3) resulting in the formation of $CoWO_4$ (our spectra were compared with the ones reported in [15–17]). The formation of $CoWO_4$ could also be inferred by the EDX analyses, which showed a Co/W ratio of 1 in these agglomerates. A different elemental composition was observed throughout the impactor stages in this test by SEM/EDX. Particles rich in tungsten were collected mostly in the stages with AED<0.32 μm, as nanometric agglomerates. In these stages also cobalt-tungsten mixed particles with Co/W ratio ca. 1 were observed (as shown in Figure 3.4). It was not possible to observe tungsten oxides by Raman spectroscopy indicating that the main compound vaporized could be $CoWO_4$ (209 w, 275 vw, 340 m, 408 w, 536 w, 686 m, 768 w, 881 s cm^{-1}) and not WO_3 (133 w, 268 m, 328 w, 712 m, 806 s cm^{-1}, as reported in [18]). The

mixed Co/W aerosols were also observed in the stages with 0.56<AED<1.8 μm. While separated spherical particles and irregularly shaped particles of the individual starting materials, containing predominantly cobalt, were observed in the stages with bigger AED (1.8<AED<18 μm, as observed in Figure 3.4).

Also for tests conducted with cobalt and stainless steel an elemental partitioning in the different size ranges was observed. Single spherical particles were observed in the stages with cut-off size 3.2<AED<18 μm. In these stages it was possible to observe isolated particles containing just Co or the cladding material (Fe, Cr). Agglomerates were found in the further stages with a progressively smaller primary particle diameter until nanometric agglomerates appeared on the stage 6 (Cut-off size AED of 0.56 μm). These particles contained Fe and Cr, while cobalt was present as a minor component. Raman analyses showed for these stages the presence of just steel-related phases, such as magnetite, ferrite or chromite (comparing our spectra with the ones of Hanesh [19]). This indicates that the stainless steel is the main material vaporized in these tests.

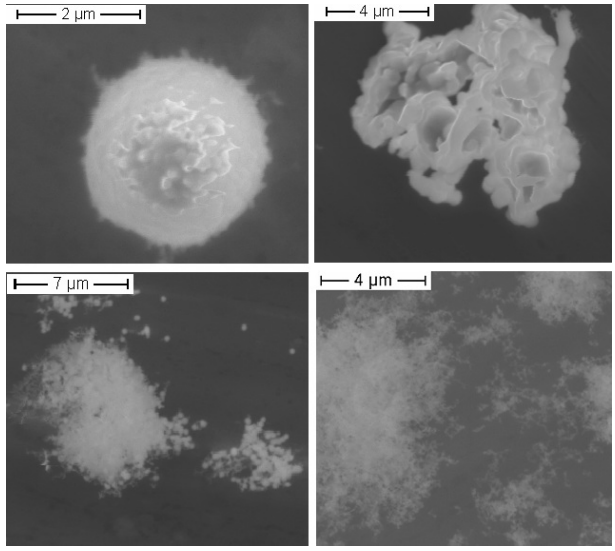

Figure 3.4: Examples of oarticles from mixed cobalt-tungsten sample (50/50% wt.). Showing the different particles collected: top, aerosols collected from the first stages (1.8<AED<18μm), isolated big particles and an externally mixed agglomerates; bottom, mixed agglomerates containing Co and W, in the smaller particles higher content of W was detected by SEM/EDX. The following EDX results show the average concentration together with the maximum value detectable.

Stages	AED (μm)	Average concentration (%wt.)	Maximum concentration (%wt.)	
0-4	1.8<AED <18	Co 78.5, W 21.5	Co 98.9, W 1.1	Co 8.0 W 92.0
5-8	0.18<AED <1.8	Co 20.9, W 79.1	Co 49.3, W 50.7	Co 7.4, W 92.6

The mixture of cobalt, tungsten and stainless, intended to simulate a multiple

cladding system, showed finally a peculiar behaviour. Low concentrations of tungsten were detected by EDX on all the impactor stages (<4%$_a$), and by Raman spectroscopy it was not possible to detect chemical compounds containing W. The bands in the Raman spectrum were solely related to phases formed from steel (such as magnetite, ferrite or chromite [19]). This mixture had a behaviour as if only stainless steel was present. This could indicate that the tungsten is not vaporized in these tests but retained in the pellet. To check for this possibility analyses of the pellet by EDX after the test were performed. These showed a higher concentration of tungsten in the laser shot area with respect to the un-melted material. All of this indicates that tungsten is retained in the pellet, possibly by the formation of a stable alloy with iron and chromium. This alloy could prevent the tungsten vaporization. Consequently the cobalt, the source material, behaved similarly to the case in which only stainless steel was present as cladding material, and was found as isolated particles in the first stages. Finally in these tests the size distribution shows only a peak in the smaller nanometric size range (Figure 3.1, μ=256 nm σ=504 nm), which can be explained by the fact that a high melting material (stainless steel) was vaporized as the major compound, which was quenched quickly to solid particles with a small diameter.

Summarizing the results for the cladding-source interaction, we could observed that:

- Tungsten had a strong effect on the release, changing the size distribution and creating a new compound.
- Stainless steel did not interact with the simulated source material and was the main material observed in the aerosols.
- Finally when the mixture of tungsten and stainless steel as cladding materials was tested the sample behaved as if only stainless steel was present. Tungsten was observed to be retained in the pellet, not participating in the aerosols formation process.

3.3.3. CsCl

The aerosol characterisation from this material was presented in Chapter 2. This material presented the highest aerosol total mass release of the sources tested in this study. This is related to the highest vapour pressure of this compound with respect to the other sources tested. Again the size distribution of the collected aerosols showed a bimodal shape, the peak in the nanometric size range corresponding to a log-normal size distribution, with μ=873 nm and σ=511 nm.

Analysis by Raman spectroscopy was not possible as first order vibrations are not allowed due to the crystal symmetry of CsCl. Additional tests with different levels of humidity were also performed (ca. 20, 50, 90% relative humidity at room temperature) and for these Raman analyses were carried out to verify the presence of hydrates or hydroxide. These should show a broad peak between 3000-3700 cm^{-1}. However this

peak could not be detected, indicating that CsOH was not formed in these tests. This could be due to the low saturation value of water in air at room temperature.

3.3.4. CsCl AND THE CLADDING

The influence of the cladding on the aerosol characteristics has been studied, testing tungsten and a mixture of tungsten and stainless steel also for the CsCl sample. The cladding material did not influence the characteristic morphology of the aerosols, but a higher mass release was detected in presence of tungsten, similar to the cobalt experiments. This higher mass release is related to the higher temperature reached in presence of tungsten, because it adsorbs better the laser light with respect to CsCl (as it has an higher emissivity), and it acts as a thermal conductor. Also in this experiment the higher release leads to a shift of the peak in the accumulation mode (nanometric size range) to bigger AED (μ=1.6 μm, σ=600 nm), which can be explained by the faster agglomeration rates, due to the higher concentration of primary particles.

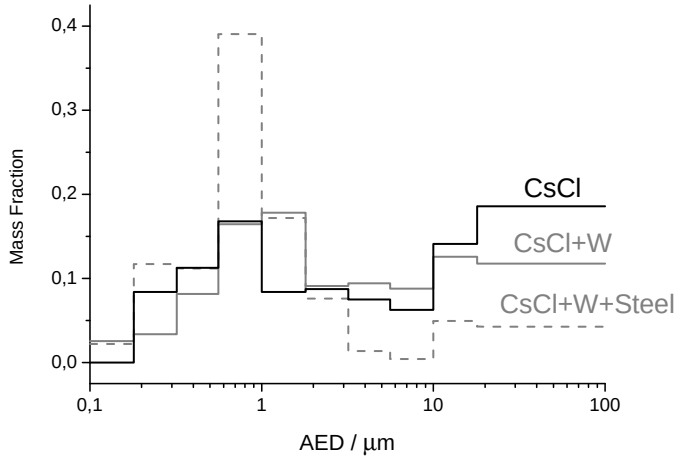

Figure 3.5: Aerosol size distribution for the CsCl sample and its mixture with the cladding materials, obtained by weighing the MOUDI impactor plates before and after the experiments. The size distribution refers to a CsCl+W+Steel mixture (25/50/25 composition), with may explain the minimal shift of the peak to μ=1.11 μm (σ=600 nm).

An influence of the tungsten cladding material was observed also for the elemental partitioning studied through-out the impactor stages:

- The first stages (3.2<AED<18 μm) showed isolated particles containing either CsCl or W.
- In the middle stages (0.56<AED<3.2 μm) mixed agglomerates containing both compounds were found.

- While in the last stages (0.18<AED<0.56 μm) particles with a high concentration of W were observed.

Also a clear difference in the Raman spectra could be observed between the difference stages, confirming a chemical partitioning: the stages 7-8 (0.18<AED<0.56 μm) contain principally WO_3 whereas the AED stages with cut off size 0.56<AED< 1 μm revealed complex and different spectra (as shown in Figure 3.6 for the stages 5 and 8, with cut-off AED of 1, and 0.18 μm). New bands at 320, 700-780 and 900 cm^{-1} were detected. For the stages with cut-off size 1<AED<0.56 μm (as shown in Figure 3.6 for stage 5) the comparison of the Raman spectra appeared difficult. The aerosols collected revealed the bands of WO_3 (using literature data by Haro et al. [20]) as a major phase: the most intense absorptions (133 w, 268 m, 328 w, 712 m, 806 s cm^{-1}) correspond to WO_3, indicating a higher concentration of this compound. A minor contribution from another phase (low intensity bands) was observed, and this phase was attributed to Cs_2WO_4 aged in air. Because the Raman spectrum of Cs_2WO_4 was not reported in literature, we measured the reference spectra of the pure compound (obtained from INTERFINE CHEMICALS) as well as the compound aged in air (hydrated in the atmospheric environmental conditions) in this work.

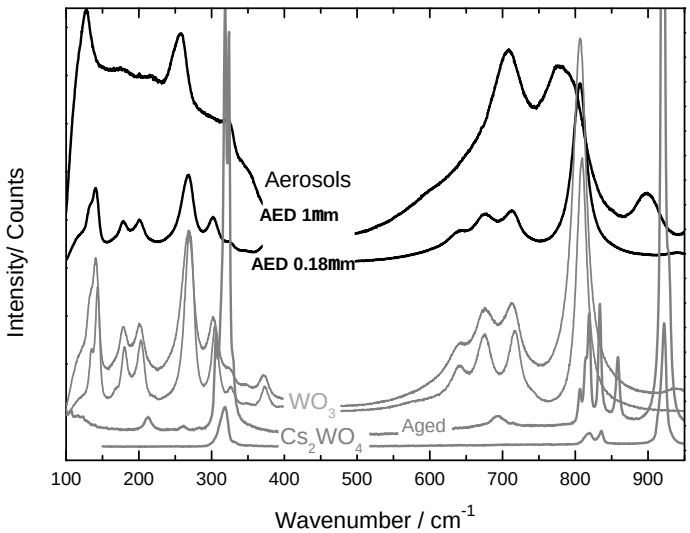

Figure 3.6: Results from the Raman analyses on the aerosols produced from a mixture of CsCl and W showing a chemical partitioning over the different stages. Smaller particles show the presence of WO_3. The middle stages show some modification in the spectra (e.g. 320, 700-780 and 900 cm^{-1} bands) that are related to the formation of a new chemical compound.

The mixture of CsCl with tungsten and stainless showed similar behaviour as

observed for the case of cobalt, i.e. tungsten was not detected in the particles. Increasing the tungsten content (from 33%$_w$ to 50%$_w$ as shown in Table 3.2) in the sample did not significantly increase the tungsten concentration detected by SEM/EDX in the particles, indicating that tungsten was always the minor compound vaporized. Stainless steel related phases were instead observed by EDX in all size ranges, while Cs and Cl were observed mainly in the first stages (3.2<AED<18 μm), and attached to bigger particles of stainless steel. On the other hand the vaporized stainless steel seems not to interact chemically with the CsCl. Variation of the chemical composition of the aerosols was not detected by Raman spectroscopy, and the only species observed were stainless steel related phases. However, when increasing the tungsten content in the tested sample (from 33%$_w$ to 50%$_w$ as shown in Table 3.2) it was possible to observe some Raman bands that could not be assigned to stainless steel phases and which showed similarity with the Cs_2WO_4 spectrum. From this we can conclude that tungsten is mainly retained in the pellet in presence of stainless steel, and by increasing the tungsten concentration it is possible to force the vaporization of a small amount of tungsten, mainly in the form of a new chemical compound (possibly Cs_2WO_4).

Summarizing the results for the cladding-source interaction for CsCl samples, we observe that:

- Again tungsten seems to have an high effect on the release, leading to a higher total aerosol mass collected, changing the size distribution and creating a new compound.

- When the mixture of cladding materials was tested the sample behaves as if just stainless steel was present. When an excess of tungsten was present in the sample, it was possible to detect a new phase in the aerosols (possibly Cs_2WO_4).

3.3.5. IR

The Ir sample showed a strong resistance to oxidation. The vapour pressure of this material, both in the metal and oxide form, is lower than for all the other tested compounds. This resulted in the lowest quantity (total mass) of aerosols collected. The aerosols revealed similar morphology to the other test materials: micrometer spherical particles and nanometric agglomerates in fractal-like structures. The size distribution was difficult to measure due to the low mass collected which resulted in high uncertainties due to the detection limit of the balance.

Analysis of these particles by SEM/EDX showed a low content of oxygen in all the particles. Raman spectroscopy of the collected particles also did not reveal the characteristic bands of IrO_2, and showed high fluorescence. All of this may suggest that the sample is vaporized as metallic Ir, as in fact this fluorescence behaviour is reported for Ir metal in [21]. On the other hand when the pellet was analysed by Raman spectroscopy, the bands of IrO_2 could be detected on the laser melted area (as reported in [22]). The discrepancy between aerosols and the oxidation state of the pellet can be

explained by the fact that the oxidation occurs during the cooling of the pellet when aerosols are no longer released. Moreover, iridium oxides are reported to decompose to the metal [23] in the temperature range of our experiments.

3.3.6. IR AND THE CLADDING

For this sample only stainless steel was tested, as this is the main cladding applied with iridium. The aerosols did not show major morphology differences. The main material vaporized was again stainless steel, which was found throughout all the stages. Ir was detected just in the first stages (3.2<AED<18 μm), and was collected as big spherical isolated particles or as externally mixed particles with Fe and Cr.

The possibility of a chemical interaction between these materials has been excluded by Raman analyses, which showed only the bands of the oxidized steel phases. It can be concluded that Ir has not a high release during our experiments, and does not interact chemically with the cladding material tested. This results in the low total mass released.

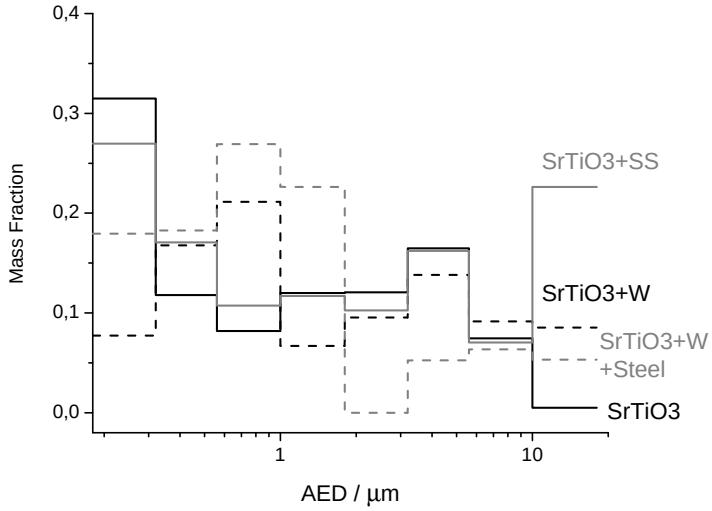

Figure 3.7: Aerosol size distribution for the $SrTiO_3$ sample and its mixture with the cladding materials, obtained by weighing the MOUDI impactor plates before and after the experiments.

3.3.7. $SRTIO_3$

For $SrTiO_3$ a similar morphology and size distribution of the aerosols was found compared to the other material tested (Figure 3.7, μ=470 μm), showing big micrometer-sized spherical particles and agglomerates of smaller nanometric particles. Moreover on the pre-stage (AED>18 μm) also solid fragments were observed, related to the

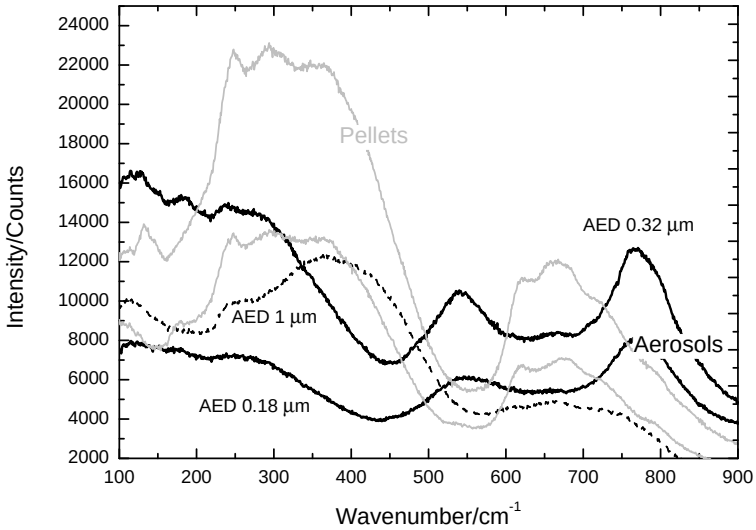

Figure 3.8: Raman spectra for the $SrTiO_3$ aerosols and pellets, showing the difference between the bulk material and the first order bands related to the nanometric aerosols. In particular, the spectrum of the particles in stage 5 (AED of 1 μm) are similar to the bulk material, indicating that this effect becomes evident only for smaller particles.

ejection of pieces of the un-melted material from the pellet. This phenomenon may be caused by high stress in the brittle pellet, caused by the thermal shock imposed by the laser pulse.

EDX analyses of the particles showed no sign of dissociation of the initial compound, the particles containing always Sr and Ti in equal amount. Finally Raman spectroscopy permitted to observe differences between the pellet and the collected aerosols (as shown in Figure 3.8): the first showed the typical broad bands of $SrTiO_3$ crystal (as reported in [24] at ca. 200-500 and 600-750 cm^{-1}), while the aerosols showed bands related to first order vibrations (broad bands at ca. 550 and 800 cm^{-1}). As explained in literature [25, 26] defects, size effects or strains can break the symmetry of the crystal and allow the detection of first-order Raman bands. Moreover for the particles with cut-off size AED of 1 μm the spectrum was similar to that of $SrTiO_3$ crystal. This shows that this effect is less visible for particles with bigger dimension and is related to the nanometric dimension of the particles in the lower stages of the MOUDI impactor.

3.3.8. $SrTiO_3$ AND THE CLADDING

The test with cladding materials showed similar results as in the experiments performed for the other sources. The morphology of the particles was not influenced by

the presence of the cladding material, while the chemical composition of the aerosols showed modifications. For this experiment the total aerosol mass released was not influenced by the cladding material and the total mass released was similar for all the experiments. Finally again a shift of the peak in the nanometric size range was observed in presence of tungsten (Figure 3.7, μ=750 μm) but not when stainless steel was tested.

When tungsten was included in the sample as cladding material the formation of a new compound was detected by Raman spectroscopy (shown in Figure 3.9, from the band at 922 cm^{-1} as compared with the data for $SrWO_4$ by Zhao et al. [27]). Moreover an elemental partitioning was observed in presence of tungsten:

- Nanometric particles, collected in the lower stages (0.18<AED<0.56 μm), were enriched in the cladding material. These showed the bands of WO_3 by Raman spectroscopy.

- In the intermediate stages (0.56<AED<1 μm) mixed particles were found. These showed by Raman analyses the bands related to a new compound.

- Finally in the bigger particle (AED>1 μm) the isolated initial compounds were detected by EDX. The particles containing either the source material or the cladding material.

On the other hand when stainless steel was included in the sample, no chemical interaction with the source material was observed. In this case phases related to the cladding material (stainless steel) was collected as the main compound of the aerosols throughout all the stages. The Raman spectra showed just the bands of the steel related phases in all the stages. In the pre-stage of the impactor aerosols containing the initial isolated compounds were detected.

Finally when the stainless steel and tungsten were present together as cladding materials, a low content of tungsten was detected in the collected aerosols. The aerosols showed similar features as for the stainless steel cladding test.

The results for the $SrTiO_3$ can be summarized as follows:

- Tungsten shows a chemical interaction with the source material, and in that case a chemical partitioning with the AED was observed.

- Stainless steel on the other hand did not interact with the simulated source material and steel-related phases were the main materials detectable in the aerosols.

- The tungsten was retained and not vaporized when the mixture of cladding materials was tested. The sample behaves as if only stainless steel was present.

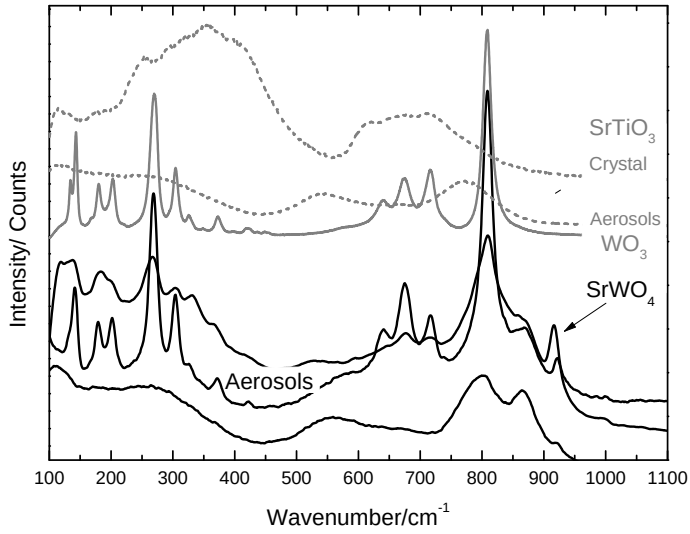

Figure 3.9: An example of Raman spectra for the aerosols collected from a $SrTiO_3$ sample with tungsten showing chemical partitioning with AED. In the smaller particles the bands of WO_3 can be observed. The formation of $SrWO_4$ can be inferred by the band at 922 cm^{-1}

3.4. DISCUSSION AND CONCLUSIONS

It should be emphasized that mass and size distribution of the air-borne material are the main parameters for the evaluation of the effects of a RDD explosion. Integral experiments [5, 6] using explosives showed that the particles released from such events could be divided in big micrometer particles (related to the mechanical impact of the explosion), and smaller nanometric particles (related to vaporization process resulting from the high temperature created). The smaller particles are generally the most dangerous as they are air-borne and inhalable and can be transported over larger distances. Release related to vaporization of the sample is consequently the main feature to be investigated for risk assessment. In our experiments these particles are produced by vaporization of the sample using a laser heating technique, which permits to obtain rapid-high-temperature transients and mimic the RDD temperature conditions. The particles are formed by a rapid quench of the vapour released from the sample in a cooler air environment. Thus it is possible to study the vaporization process and the influence of interaction with other materials on the aerosol characteristics. However, it is also clear that the conditions of a real detonation cannot be simulated by the system, due to the impossibility to reproduce an explosive wave in our set-up.

In our tests we have observed a bimodal size distribution similar to that reported in literature for integral experiments [5, 6]. Micrometer particles were collected together

with nanometric particles in our experiments, related to the ejection of material by the mechanical shock of the laser shot. This can be liquid material from the laser melted area which creates spherical micrometer particles, or solid irregular-shaped fragments generated from the un-melted pellet. It was possible with our tests to investigate the different characteristics of the particles in these two size range, although the fractional release between the two types of aerosols cannot reproduced that of a RDD detonation.

In our studies different release characteristics were observed for the different sources studied:

- CsCl showed the highest total mass released. The aerosols collected had the same chemical composition as the initial sources.
- Co aerosols were collected in lower mass with respect to CsCl, and the particles were mainly composed of cobalt oxides.
- Ir revealed the lowest vaporization, due to low vapour pressure and high oxidation resistance. Particles were collected in the metallic form.
- $SrTiO_3$ showed a similar morphology and mass release as cobalt, but the aerosols collected kept their initial composition.

Our test focused also on the effect our source-cladding interaction on the aerosol release. The results can be summarized as follows:

- CsCl particles were collected only in bigger AED when in presence of stainless steel. In presence of tungsten a different chemical partitioning with AED was observed. The bigger particles were isolated aerosols containing or CsCl or W. In the middle stages mainly mixed compound aerosols were found, and the formation of Cs_2WO_4 was observed. Finally in the smaller AED the main aerosol species were related to W compounds. The total mass released was higher in presence of tungsten.
- Co was found in low quantity in the aerosols when in presence of stainless steel. In presence of tungsten, cobalt forms $CoWO_4$ aerosols. These were collected in all the stages of the impactor, also in the one with the smallest AED.
- Ir was found just with AED>3.2 μm when in presence of the cladding material.
- $SrTiO_3$ showed a chemical reaction when W was used as cladding material with the formation of new compound. No interaction with stainless steel was observed.

From these results it can be concluded that the presence of stainless steel does not lead to a chemical interaction with the tested source materials. Moreover the aerosols containing the simulated radioactive materials are concentrated in the higher AED, leading to a lower probability of inhalation in the lungs. Tungsten instead seems to have a substantial effect, as an increase in the total mass release was observed. This

was related to the creation of more volatile compounds but also by a heat transfer mechanism typical for our set-up. Although in this case a shift to bigger AED has been observed, it was minimal not affecting the risk by inhalation in the lungs (AED<10 μm). In all cases (except iridium), tungsten showed a chemical interaction with the source materials, creating new chemical compounds (tungstates). This chemical interaction has a strong effect on the aerosol formation process as a compound with different thermo-physical is created. This could result in a change of the coagulation and collision rates, which could concentrate the radioactive source material in a particular size range. Consequently it must be considered in the evaluation of the radiological consequences of a RDD explosion.

Finally when the two cladding materials were tested together, retention of tungsten was observed in the sample by formation of an alloy with iron and chromium. This prevented its interaction with the source material in the gaseous phase, and the samples tested behaved as if only if stainless steel was present. This effect is probably typical for our experiments in which the source material and the cladding materials were mixed as powders, thus easing the alloy formation and preventing vaporisation of W. It must be investigated if this reaction could occur in a real RDD explosion.

Finally, we can compare our findings to the observations of the integral tests. In the tests of Harper et al. [5] no chemical reactions were observed, and the soil entrained in the fireball was observed to interact with the radioactive materials only by agglomeration and/or coagulation, affecting the size of the "radioactive" particles. However we should point out that minor chemical analyses were performed on the particles, which does not exclude chemical interactions. On the other hand in the tests of Lee et al. [6] on CsCl the effect of chemical interaction on the source was clearly observed (such as a different ratio of Cs and Cl in the aerosols), without identifying the cause of this effect. Our work clearly shows the importance of detailed characterisation of the aerosols and that these separate effect studies are useful to effectively study the aerosol formation mechanisms from the vapour phase, the chemicals reactions, and moreover observe their different influence on the aerosol characteristics.

We can conclude that with our tests we were able to study the vaporization-condensation process occurring in dirty bombs detonations in controlled laboratory conditions. In particular we could produce and investigate the nanometric particles of greatest interest for the risk assessment of RDD explosions. An important outcome of our work is the observation of the possibility of an elemental and chemical partitioning with AED of the particles produced when interaction with the cladding material of the source occurs. This can influence the assessment of the extension and level of the contaminated area using radioactive dispersion codes which needs to be included in the description of the source term for such calculations. Our tests thus emphasize the importance of studying not only the cladding materials of the source, but also other materials of interest that could chemically or physically interact with the source material.

REFERENCES

[1] J. Medalia. "dirty bombs": Technical background, attack prevention and response, issues for congress. Technical Report R41890, Congressional Research Service, 2011. Last access from internet 20/01/2014: http://www.fas.org/sgp/crs/nuke/R41890.pdf.

[2] H. Shin and J. Kim. Development of realistic RDD scenarios and their radiological consequence analyses. *Applied Radiation and Isotopes*, 67(7-8):1516–1520, 2009.

[3] J. Magill, D. Hamilton, K. Latzenkirchen, M. Tufan, G. Tamborini, W. Wagner, V. Berthou, and A. von Zweidorf. Consequences of a radiological dispersal event with nuclear and radioactive sources. *Science & Global Security*, 15(2):107–132, 2007.

[4] K. G. Andersson, T. Mikkelsen, P. Astrup, S. Thykier-Nielsen, L. H. Jacobsen, S. C. Hoe, and S. P. Nielsen. Requirements for estimation of doses from contaminants dispersed by a dirty bomb explosion in an urban area. *Journal of Environmental Radioactivity*, 100(12):1005–1011, 2009.

[5] F. T. Harper, S. V. Musolino, and W. B. Wente. Realistic radiological dispersal device hazard boundaries and ramifications for early consequence management decisions. *Health Physics*, 93(1):1–16, 2007.

[6] S.D. Lee, E.G. Snyder, R. Willis, R. Fischer, D. Gates-Anderson, M. Sutton, B. Viani, J. Drake, and J. MacKinney. Radiological dispersal device outdoor simulation test: Cesium chloride particle characteristics. *Journal of Hazardous Materials*, 176(1-3):56–63, 2010.

[7] Z. Prouza, V. Beckova, I. Cespirova, J. Helebrant, J. Hulka, P. Kuca, V. Michalek, P. Rulik, J. Skrkal, and J. Hovorka. Field tests using radioactive matter. *Radiation Protection Dosimetry*, 139(4):519–531, 2010.

[8] W. D. Reinhart, T. F. Thornhill, L. C. Chhabildas, W. G. Breiland, and J. L. Brown. Temperature measurements of expansion products from shock compressed materials using high-speed spectroscopy. *International Journal of Impact Engineering*, 35:1745–1755, 2008.

[9] R. Simpson, L. Fried, F. Ree, and J. Reaugh. Unraveling the mystery of detonation. *Science and Technology Review*, June:12–18, 1999.

[10] F.G. Di Lemma, J.Y. Colle, M. Ernstberger, H. Thiele, G. Rasmussen, and R.J.M. Konings. Rades an experimental set-up for the characterization of aerosol release from nuclear and radioactive materials. *Journal Aerosol Science*, 70(5):36–49, 2014.

[11] K. G. Andersson, T. Mikkelsen, P. Astrup, S. Thykier-Nielsen, L. H. Jacobsen, L. Schou-Jensen, S. C. Hoe, and S. P. Nielsen. Estimation of health hazards resulting from a radiological terrorist attack in a city. *Radiation Protection Dosimetry*, 131(3):297–307, 2008.

[12] W. J .F. Standring, M. Dowdall, M. Sneve, O.G. Selnæs, and I. Amundsen. Assessment of environmental, health and safety consequences of decommissiong radioisotope thermal generatator (RTGs) in Northwest Russia. Technical report, Staten stralevern, Norwegian Radiation Authory, 2005.

[13] R. Heard. IAEA action to improve the management of disused sealed radioactive sources (DSRS) including RTGs, 2008. Presentation to CEG – 23 to 24 April, 2008.

[14] S. K. Friedlander. *Smoke, Dust, and Haze: Fundamentals of Aerosol Dynamics*. Oxford University Press, 2 edition, 2000.

[15] S. Thongtem, S. Wannapop, and T. Thongtem. Characterization of $CoWO_4$ nanoparticles produced using the spray pyrolysis. *Ceramics International*, 35(5):2087–2091, 2009.

[16] U. Sujana-Kumari, P. Suresh, and A.V. Prasada-Rao. Grinding-assisted solid-state metathetic synthesis of divalent transition metal tungstates. *International Research Journal of Pure and Applied Chemistry*, 3(1):1–9, 2013.

[17] J. Ruiz-Fuertes, D. Errandonea, S. López-Moreno, J. González, O. Gomis, R. Vilaplana, F. J. Manjón, A. Muñoz, P. Rodr´-Hernández, A. Friedrich, I. A. Tupitsyna, and L. L. Nagornaya. High-pressure Raman spectroscopy and lattice-dynamics calculations on scintillating MgWO: Comparison with isomorphic compounds. *Physical Review B*, 83(21):214112–214123, 2011.

[18] Wu W., Yu Q., Bao J. Lian J., Liu Z., and Pei S.S. Tetragonal tungsten oxide nanobelts synthesized by chemical vapor deposition. *Journal of Crystal Growthring*, 312: 3147–3150, 2010.

[19] M. Hanesh. Raman spectroscopy of iron oxides and (oxy)hydroxides at low laser power and possible applications in environmental magnetic studies. *Journal of international Geophysics*, 177:941–948, 2009.

[20] E. Haro-Poniatowski, M. Jouanne, J.F. Morhange, Diamant R. Julien, C., M. Fernández-Guasti, G.A. Fuentes, and J.C. Alonso. Micro-raman characterization of WO_3 and MoO_3 thin films obtained by pulsed laser irradiation. *Applied surface Science*, 127-129:674–678, 1998.

[21] R.T.M Downs. The RRUFF project: an integrated study of the chemistry, crystallography, Raman and infrared spectroscopy of minerals, 2006. 19^{th} General Meeting of the International Mineralogical Association.

[22] A.V. Korotcov, Tiong K.K. Huang, Y.S., and D.S. Tsai. Raman scattering characterization of well-aligned RuO_2 and IrO_2 nanocrystals. *Journal of Raman spectroscopy*, 38:737–749, 2007.

[23] R. Sanjinds, A. Aruchamy, and F. Lévy. Thermal stability of sputtered iridium oxide films. *Journal of the Electrochemical Society*, 136(6):1740–1743, 1989.

[24] V. I. Merkulov, J.R. Fox, H. C. Li, W. Si, A.A. Sirenko, and X.X. Xic. Metal–oxide bilayer Raman scattering in $SrTiO_3$ thin films. *Applied Physics Letters*, 72(25):3291–3293, 1998.

[25] Y.L. Du, G. Chen, and M.S Zhang. Investigation of structural phase transition in polycrystalline $SrTiO_3$ thin films by Raman spectroscopy. *Solid State Communications*, 130:577–580, 2004.

[26] F.A Rabuffetti, H.S Kim, J.A. Enterkin, Y. Wang, C. H. Lanier, L.D. Marks, K.R. Poeppelmeier, and P.C. Stair. Synthesis-dependent first-order Raman scattering in $SrTiO_3$ nanocubes at room temperature. *Journal of Chemistry of Materials*, 20: 5628–5635, 2008.

[27] X. Zhao, T. L. Y. Cheung, X. Zhang, D. H. L. Ng, and J. Yu. Facile preparation of strontium tungstate and tungsten trioxide hollow spheres. *Journal of American Ceramic Society*, 89(9):2960–2963, 2006.

4

FISSION PRODUCT PARTITIONING IN AEROSOL RELEASE FROM SIMULATED SPENT NUCLEAR FUEL

F.G. Di Lemma, J.Y. Colle, G. Rasmussen, and R.J.M. Konings

Aerosols from the vaporization of simulated nuclear spent fuel (simfuel) were produced by the laser heating techniques, presented in the previous chapters, and characterised by a wide range of post-analyses. In particular attention has been focused on determining the fission products behaviour in the aerosols. This could help in a better determination of the source term and consequently of the risk associated with release from spent fuel sabotage or accidents. Different simulated spent nuclear fuels were tested with burn-up up to 8%$_a$. The results from the aerosols characterisation were compared with studies of the vaporization process by experiments with the Knudsen Effusion Mass Spectrometer and thermochemical equilibrium calculations, as these studies permit to understand the aerosol gaseous precursors and the gaseous interactions taking place during the aerosol formation process.

Parts of this chapter have been submitted to Journal of Nuclear Materials.

4.1. INTRODUCTION

Release from nuclear fuel has been extensively investigated for reactor accident scenarios [1–6], however less work has been conducted on the release from spent fuel during storage or transport. This topic has acquired interest in view of the Fukushima accident. This event has shown the importance of the safety of spent fuel ponds. Although studies on the safety of spent fuel pools were previously performed (e.g. by the Nuclear Regulatory Commission), these events were believed to be unlikely and no specific measures were considered [7–9]. Following the Fukushima accident new studies have been performed, such as the one of the Nuclear Regulatory Commission [10]. This last study concluded that the spent fuel is only susceptible to a release within a few months after de-fueling, and that a more favourable loading pattern (avoiding dense packaging) and the improvement of the mitigation strategies could significantly reduce potential releases. Another scenario, which could lead to aerosolization of spent fuel, is related to release during transport of spent fuel casks due to accidents. In this frame a study was performed by Dykes and Machiels [11], which concluded that the probability of such accidents is less than $5*10^{-6}$. However no assessment of the release was performed. Finally even though malicious actions are tried to be ruled out through security measures, it is important to understand the effects of such attacks on spent nuclear fuel. As proposed by Alvarez et al. [12], and demonstrated by the September 11^{th}, terrorist attacks are a tangible threat. Magill et al. [13] assessed the consequences for such events but considered a hypothetical respirable fraction for such releases. Studies on the aerosol release from such events need to be conducted, as performed by Molecke et al. [14, 15] in the past. Their experiments consisted of explosive aerosolization tests using HEDD (High Energy Dispersive Devices) on simulated nuclear reactor rods and of the analyses of the particles released.

The present study aims at describing the aerosol release from spent nuclear fuel under different release scenarios, simulating events in which air contact with overheated spent fuel can occur, such as spent fuel sabotage or accidents during transport or storage. The particles size distribution is studied, as it is needed to evaluate the consequences of a Radiological Dispersion Events (RDE's), for example to assess the extension and levels of the contaminated area. The AED (Aerodynamic Equivalent Diameter) of the particles strongly influences the aerosol transport behaviour, but also the probability of aerosol inhalation of the exposed population. It is thus important to understand the size range in which the high activity elements will be concentrated. Focus is posed in our studies on analysing the fission product partitioning as function of the particles AED. The ultimate goal is the understanding of the mechanisms influencing the aerosol formation. To achieve this, separate effect experiments have been performed analysing different variables (e.g. burn-up). These results have been finally coupled with studies of the gaseous aerosol precursors. The gaseous release has been obtained from thermochemical equilibrium calculations and experiments using the Knudsen Effusion Mass Spectrometer (described previously in [16, 17] and in detail in Appendix B). These studies permit in fact to understand the interactions of the gaseous phases during aerosol formation processes.

4.2. INSTRUMENTATION AND EXPERIMENTAL PROCEDURE

The set-up applied in our studies has been described in in Chapter 2. Laser heating was used in these studies to vaporize the samples and to simulate a radioactive release. Laser heating to simulate such events was applied only in a few studies beforehand [18, 19] for simulating accidental scenario related to reactor power transients. This technique was chosen in the present experiments for various reasons, such as limiting interactions between the sample holder, the heating elements and the sample, avoiding radioactive contamination of the heating components, reaching extreme temperature transients, but especially to have repeatable temperature on the sample. This was achieved by applying a PID controller to the laser power. In Figure 4.1 a comparison of the PID temperature regulation performed for ZrO_2 and UO_2 samples is presented. It can be noticed that the ZrO_2 samples need a high laser power, prolonged in time, to obtain a quasi-square temperature transients compare to UO_2 samples. This is related to the higher emissivity of the UO_2 samples with respect to ZrO_2. Difficulties were however found while heating the UO_2 samples due to cracking, which influenced the PID regulation causing instability in the control. The breaking of the sample cannot be avoided and is related to the high thermal shock, due to the low thermal conductivity of UO_2. A custom-made Teflon ring was used to contain the sample and obtain a stable and reproducible heating and vaporization. Once the pellet was correctly heated, aerosols were formed by condensation of the release gases in the cooler air environment and collected for post analyses.

In these experiments the aerosols produced were analysed applying different techniques, presented in in Chapter 2, as these permit to study the morphology, the elemental and the chemical composition of the aerosols. Finally, by applying a MOUDI impactor for the collection of the particles, analyses of the size distribution and of the aerosols characteristics as function of their AED size could be performed. The elemental composition was analysed by ICP-MS as function of the particles' AED, by washing separately in solution the aluminium substrates of the various MOUDI impactor stages. However experimental difficulties, such as high counts in the blank (as for Ba, Zr) or low counts in the measured solutions (as for La, Nd), did not permit the quantification of some elements in the different tests. Finally for some of the experiments Sr, Pd and Zr trends could not be clearly observed. This can be related to ejection on the first stages of inhomogeneous pellets fragments with high concentration of such elements, which will lead to fluctuation of their trends through out the stages. We finally coupled the aerosol characterisation analyses with the results from thermochemical equilibrium calculations (performed by Factsage software, described in [20, 21]) and KEMS (Knudsen Effusion Mass Spectrometry) experiments. This was performed to identify the gaseous release, and to understand the gaseous interactions influencing the aerosol formation process. The KEMS was described in [16, 17]. It consists of a Knudsen cell coupled with a quadrupole mass spectrometer (with mass range of 1-512 amu). The cell is heated by a tungsten coil, and can be operated in vacuum or

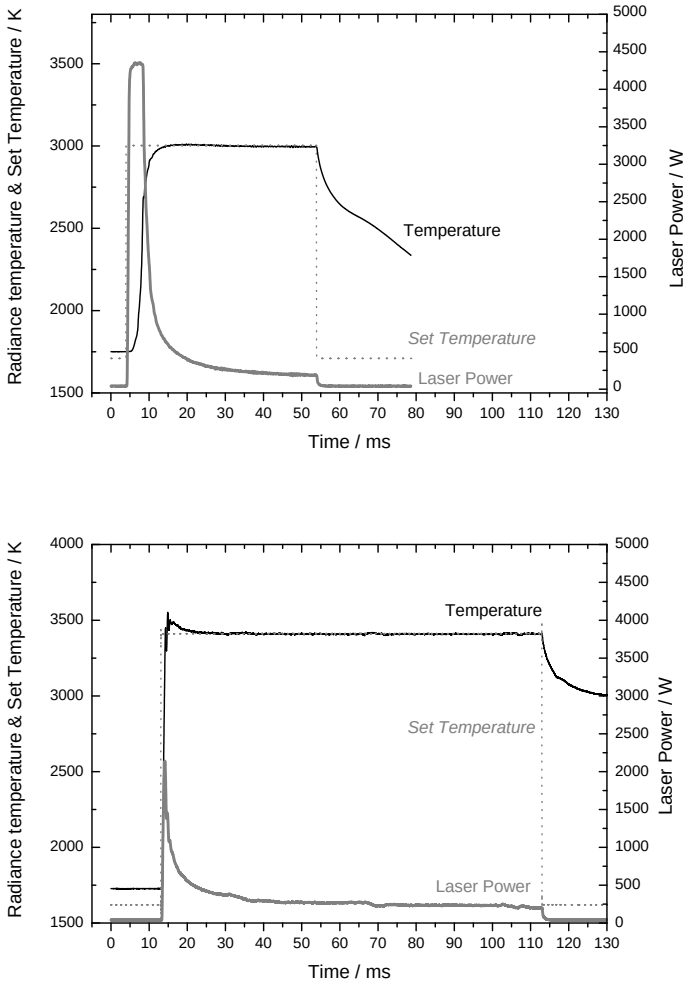

Figure 4.1: PID control on temperature for two different samples: Top ZrO_2; Bottom UO_2. It is possible to observed the higher radiance adsorbance of UO_2, which permits together with a low thermal conductivity, to obtain high temperature with low laser power and short time with respect to ZrO_2.

with a small flow of different gases (e.g. oxygen, reaching in our experiments a oxygen pressure between 1-10 Pa). The molecular beam effusing from the cell is directed and collimated into the ion source of a quadrupole mass spectrometer, in order to detected the gaseous species release as function of the temperature. Calibration of the system was performed by vaporizing, together with the sample, also a known quantity of silver. More details on this system are presented in Appendix B.

Table 4.1: Description of the samples used and of the aims of the test. For the AECL samples the data were obtained from Lucuta et al. [22–24].

Sample	Matrix	Fission Products	Aim	Description
$SFUO_2$	UO_2	$8.58\%_{wt}$	Burn-up effect	not sintered
$SFUO_2$ 1200	UO_2	$8.58\%_{wt}$	Sintering effect	sintered in furnace at 1200 °C in Ar/H_2
AECL 301	UO_2	$2.551\ \%_{wt}$	Burn-up effect	sintered in furnace at 1650 °C
AECL 800	UO_2	$7.01\ \%_{wt}$	Burn-up effect	sintered in furnace at 1650 °C
UO_2/CeO_2	UO_2	/	Pu behaviour in the aerosols	different compositions 85/15, 40/60, 60/40 %a.

4.3. SAMPLES

Different simulated spent nuclear fuels were tested to study the aerosol release for accidental and sabotage scenarios. Samples tested were composed of a matrix of UO_2 and controlled quantities of non-radioactive isotopes, intended to simulate the fission products produced in-pile. Simfuels are used to replicate the composition and micro-structure of irradiated fuel, and consequently to study different properties of spent fuel avoiding the high cost and difficulty of handling such materials. In our experiments different simfuels were used (as summarized in Table 4.1), applying both in-house made simfuels and simfuels produced by AECL in an industrial-like process. The in-house made samples were obtained by mixing commercial powders, pressing them by a hydraulic press and then sintering the obtained pellets. However during the sintering process loss of CsI could not be avoided, also when using a rapid sintering method (such as the Spark Plasma Sintering, SPS). The CsI loss was confirmed also by SEM/EDX and ICP-MS analyses on the samples before and after sintering. Therefore it was decided to perform first sintering with all the chemical compounds expect CsI, which was added after sintering. This was performed by re-pulverizing the sintered pellet, mixing it with the CsI powder and pressing this mixture in a new pellet.

Table 4.2: Composition of the tested materials, as calculated by Origen (parameter reported), and described for the AECL samples in [24].

Simfuel samples		$SFUO_2$	AECL 301	AECL 800
Parameters used in Origen				
Enrichment/%		4	none	none
Burn up/ $\%_a$		6	3	8
Years in Spent pool		1	0	0
Elements	Chemical (SF/AECL)	Weight concentration (%)		
U	UO_2	91.42	97.449	92.990
Zr	ZrO_2	0.50	0.336	0.777
Mo	Mo/MoO_3	0.45	0.356	0.980
Pd	Pd/PdO	0.21	0.147	0.652
Ba	$BaO/BaCO_3$	0.23	0.150	0.433
Y	Y_2O_3		0.040	0.075
Sr	SrO	1.38	0.223	0.531
Ce,Pu	CeO_2	4.51	0.304	0.717
La,Am,Cm	La_2O_3	0.38	0.113	0.367
Ru,Tc	Ru/RuO_2	0.33	0.360	1.026
Rh	Rh_2O_3		0.028	0.038
Nd,Pm,Sm	Nd_2O_3	included in La_2O_3	0.494	1.418
I	CsI	0.07		
Cs	Cs_2ZrO_3	0.53		

Information on the production of the AECL samples can be found in [22–24]. In these samples the high volatility elements such as Cs, I, and Te were not inserted. The

fission product inventory was calculated by ORIGEN software, and the parameters applied for the calculations are shown in Table 4.2. This table presents also the chemical compounds used to simulate the different fission products and their relative weight concentrations in the different simfuels tested.

We also tested some inactive samples containing ZrO_2 instead of UO_2 as matrix compound, as a first test on the behaviour of compounds with different volatility in a ceramic matrix (reported in Chapter 2). Finally for a better evaluation of the behaviour of plutonium in the aerosols separate experiments were performed with mixed samples containing UO_2 and CeO_2. CeO_2 was applied as an inactive ceramic material to simulate PuO_2, due to similar properties, as reported in [25, 26]. These separate effect experiments were performed with mixtures of the powders not pretreated in the furnace, in order to avoid any prior solid solution formation and consequently to know how much material was vaporized from the initial compounds inserted.

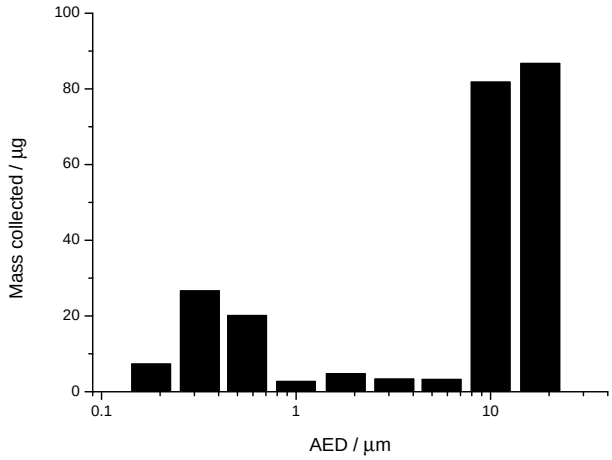

Figure 4.2: Example of particles size distribution for the tested simfuels obtained from the ICP-MS analysis, showing a bimodal size distribution.

4.4. POST-ANALYSES

4.4.1. AEROSOL CHARACTERISATION

Similar aerosol features were found for all the samples tested. No differences in the aerosol characteristics were observed between ZrO_2 samples, UO_2 compacted powders and industrial UO_2 pellets. The aerosols had a bimodal size distribution (an example of which is shown in Figure 4.2) and can be divided in two classes: big spherical micrometer particles or fragments, which were collected as a first peak in the bigger AED (AED>10 μm), and smaller agglomerates of nanometric particles,

corresponding to the second peak in the nanometric AED size range (as shown in Figure 4.3). Two different formation processes have been related to these two different morphologies, as explained in [27–29] and in the previous chapters. The bigger particles are formed by the ejection of liquid particles from the melted layer or solid material from the pellet, due to mechanical shock related to the laser heating. The nanometric particles are instead formed from the condensation of the vaporized material. These particles then agglomerate in complicated structure due to the high number of primary particles formed.

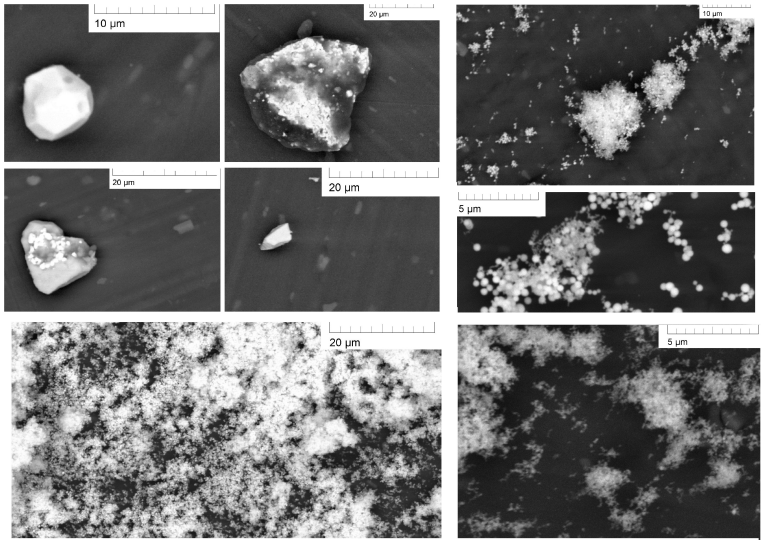

Figure 4.3: Example of the aerosol collected for the simfuel (sample AECL800), similar morphology was observed for all the samples tested

An important outcome of the post-analyses was the observation that the "fission products" concentration varies with the particles size. This was observed by SEM/EDX as function of the geometrical particle size, when the particles were collected with filters and as function of the AED when the particles were collected by the MOUDI impactor. In particular a higher concentration of the high volatile compounds was found in the smaller size particles with respect to the bigger size. The bigger particles were instead enriched in the low volatile elements such as the matrix elements (Zr, or U) or also Ba and Ce. Explanation of this partitioning can be related to the aerosol formation mechanism [29]. The bigger particles formed by the ejection of the pellet melted layer or solid fragments will be enriched in the matrix and low volatile elements, which are retained in the pellet. While the smaller particles, formed by the condensation of the vapour, will be enriched in the higher volatile elements [27–29]. In all the particles mostly U could be observed. Cs, and I were usually detectable in the smaller AED together in a ratio Cs/I of 1 for both $SFUO_2$ and ZrO_2 samples. Moreover also Cs without I was detected for the $SFUO_2$. Two different sources were identified for

Cs release for this sample, being the Cs released from CsI and from Cs_2MO_x (M= Metal, such as Zr, Mo etc). This second Cs release it caused by dissociative vaporization of Cs_2ZrO_3, as CsO and ZrO_2 [30], as this compound was inserted in the simulated fuel, or could be related to the formation of Cs_2MoO_4 as predicted from the thermochemical calculations. In fact another element detected in the smaller particles was Mo, although it was difficult to determine its chemical form (Cs_2MoO_4 or MoO_3). Finally the different "fission products" concentration between the samples did not influence the aerosols characteristics.

The "fission products" elemental size partitioning was confirmed also by the ICP-MS analyses of the solutions obtained from washing separately each impactor stage, as described in Chapter 1. From these analyses different trends were observed for the different simulated fission products. To summarize the results from all the experiments (an example is shown in Figure 4.4) we can conclude that:

- U, Ce, Zr, Y, La, Nd showed a similar trend, diminishing from the bigger to the smaller AED.
- The Ba concentration was quite stable throughout the stages, but it should realised that the Ba is difficult to measure by ICP-MS due to the contamination from the environment.
- The more volatile fission products such as Cs and also Ru and Mo were enriched instead in the smaller AED (as shown in Figure 4.5). The high volatilization of these metallic fission products, which are generally thought to be retained in the pellet, is related to the oxidising conditions applied in our experiments. These will lead to the formation of Ru and Mo oxides, which have a higher volatility and will be released in the vapour.
- It is finally worth to notice that a similar behaviour for Pd and Rh was observed in the experiments with the AECL simfuel. These are usually considered in the middle class volatile elements. Their concentration was observed to increase with decreasing AED, reaching a peak in Stage 6/7 (Cut off sizes AED 0.56-0.32 μm) and decreasing again in stage 8 (AED 0.18 μm).

We have also analysed the pellet by SEM/EDX as this can give important information on the vaporization process. By comparing the melted and unmelted region we could again confirm the ICP-MS results. It was observed that the low volatile elements (such as Ba, La, Ce) were retained in the pellet after the laser pulse, while CsI and the metallic (Ru, Mo) elements were depleted confirming their vaporization. These metals compounds were found before the laser heating experiments in the pellet as metal alloys precipitates (containing Ru, Mo, Pd) due to their insolubility in the matrix, as also reported in [22, 31].

Finally to test if a different size partitioning could occur in the aerosols between U and Pu, experiments were performed with UO_2 and CeO_2 powder mixtures with different concentrations (85/15, 40/60, 60/40 %a.). From all these experiments it was

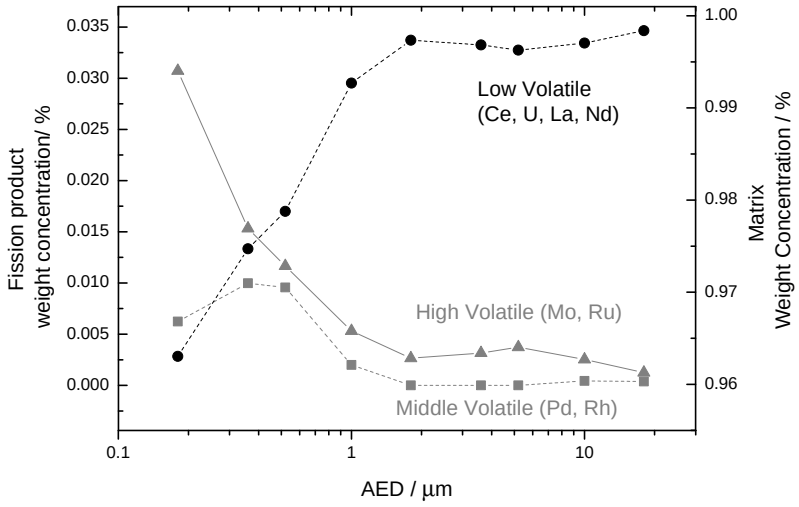

Figure 4.4: Example of aerosols concentration trends for the elements in the different volatile class, as function of the AED, for the AECL simfuels.

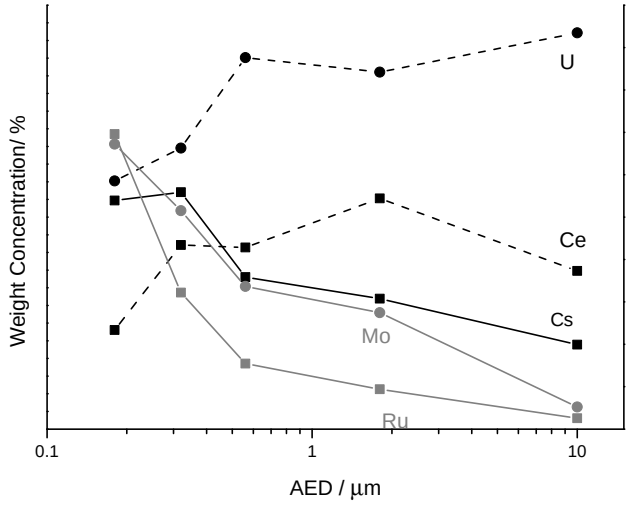

Figure 4.5: Example of aerosols concentration trends for the matrix elements and high volatile class, as function of the AED. The quantitative proportion between the compounds are not respected preferring a clear view of the trends, which shows the relation with the different release and aerosol formation processes.

observed that the main species vaporized was UO_x. The content of Ce was found to be small in the smaller AED, its concentration raising in the particles with bigger AED. This effect was confirmed by the analysis of the pellet in the melted area, which showed that this area was enriched in Ce. This again demonstrates that the different volatility of the compounds can have an effect on the aerosol size in which the radioactive elements are found.

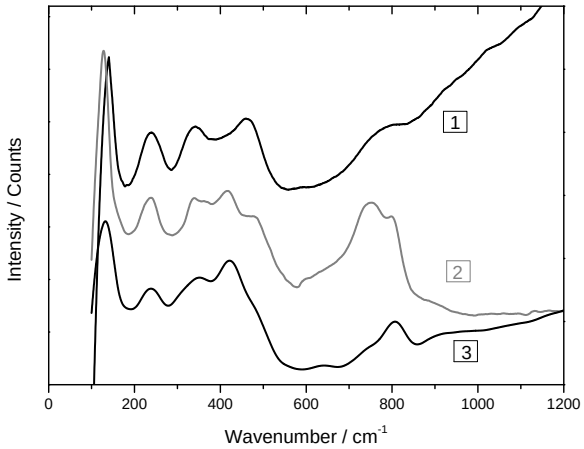

Figure 4.6: Comparison of the RAMAN spectras of the aerosols collected, from $SFUO_2$ simfuel (1,3) and UO_2 (2), showing for the $SFUO_2$ simfuel UO_{2+x} aerosols possible due to competing oxidative process with the fission products, while for the UO_2 sample the formation of U_3O_8 solid phase is evident.

The Raman spectroscopy analyses of the aerosols did not permit to identify the fission products, as these are a minor phase. This demonstrates the importance of applying different techniques in analysing the aerosol release, as SEM/EDX and ICP-MS have instead permitted to detect low elemental concentrations in the aerosols and their trends. On the other hand Raman spectroscopy enables us to observe the difference oxidation state of uranium in the aerosols. Raman spectroscopy showed that the aerosols released from the UO_2 pellets were clearly oxidized to U_3O_8 in all the analysed stages (as shown in Figure 4.6), based on a comparison with literature data [32–34]. This was also observed for the mixed sample with UO_2/CeO_2, in which the main compound released was U_3O_8 and the CeO_2 was retained in the pellet. We also tested the effect of sintering of the UO_2 pellets on the aerosols Raman spectra. However having performed the sintering in reducing condition (Ar/H_2 environment) the starting pellet material was UO_{2-x}. This seems to have an effect on the aerosols oxidation state which showed the formation of UO_{2+x}. Kinetics effect may have limited the oxidative process, reducing the gaseous release of UO_3 and the formation of the solid phase of U_3O_8. We also observed that for the simfuels (as for $SFUO_2$) the presence of the fission

products has also an effect on the aerosols Raman spectra. They showed the characteristics spectra of UO_{2+x} and not U_3O_8, also when the pellet was not sintered. The fission products, such as Mo, could have affected the oxidation of the pellet and reduced the release of UO_3 due to a competing oxidation process. This effect was also confirmed by comparing the results with the Raman spectra from the AECL samples, in which Mo was inserted already in the oxide form. In this case the aerosols presented just the U_3O_8 Raman bands.

4.4.2. EQUILIBRIUM VAPORIZATION STUDIES

KEMS measurements and thermochemical equilibrium calculations were performed to understand the gaseous aerosol precursors and chemical interaction occurring in the gaseous phase under equilibrium conditions. The KEMS experiments were conducted in vacuum and under a constant O_2 flow. The thermochemical equilibrium calculations were performed with a constant pressure ($1*10^5$ Pa), one with the O_2 fixed activity to 0.21 to simulate the vaporization process in air environment (as in our laser heating experiments), and the other in absence of O_2 in the environment, the oxygen potential was thus imposed by the release from the simfuel. The choice of using a fixed pressure calculations was consistent with the conditions in our system as we vaporize a small amount of material in a comparatively very large vessel kept at constant pressure and air environment. Thus the gases are free to expand in the cell environment.

The KEMS experiments revealed similar release patterns for all the samples. At low temperature (900-1200 K) the gaseous release of I and Cs was detected, followed by the gaseous release of Pd, Ba and Sr (as shown in Figure 4.7). Finally the low volatile species such as U, Ce, La, Nd, and Zr were detected at high temperature. Cesium was detected as the Cs^+ ion, which is the product of the fragmentation and ionisation of molecular species at the electron energy applied. We assign the peak at the lowest temperature to gaseous CsI because it is consistent with the CsI^+ and I^+ ion signals. In some cases we were able to observe a second release peak for Cs around 1100 K in the $SFUO_2$ experiment (as shown in Figure 4.7), which was not observed for the I^+ signal. This could be related to the vaporization of ternary oxides compounds, such as Cs_2ZrO_3, which vaporizes incongruently to CsO and ZrO_2 [30], or of Cs_2MoO_4, which vaporises congruently [35]. The latter compound was predicted to be the stable by the thermochemical equilibrium calculations, also with no O_2 excess. This confirms the SEM/EDX observations of the aerosols that suggest a second source for the Cs release than CsI. Moreover by the KEMS experiments and the thermochemical calculations we could observe the chemical form of the released gases, Pd as metal, Sr and Ba as oxides, as also the Lanthanides and the Actinides.

In our KEMS experiments also the influence of an oxidising environment was studied (by a O_2 flow in the cell). The most obvious difference with the experiments in vacuum was the release of MoO_3, and the lower temperature release of UO_x. No substantial differences were observed for the other elements, including ruthenium. Evidently

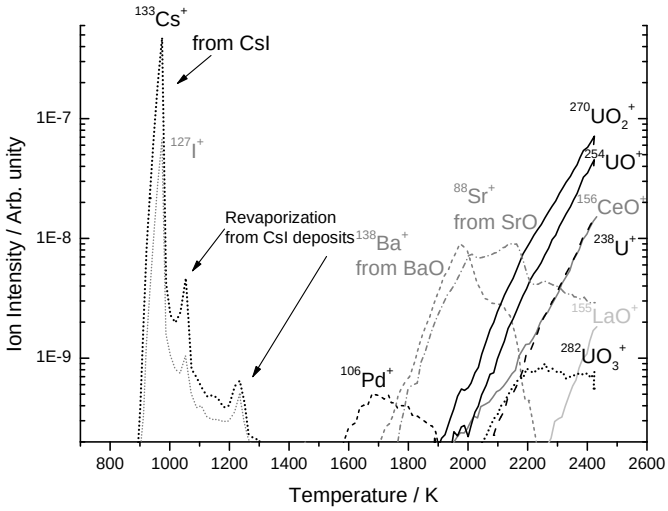

Figure 4.7: An example of KEMS for simfuel, showing the high volatile elements and lower volatile compounds released in vacuum conditions. In oxidative condition a shift to lower temperature of the release of U species could be observed, and also the release of Mo oxides.

the oxygen potential imposed by the oxygen flow was too low for oxidation to gaseous RuO_x species to occur. The release of the metallic fission products in oxidative conditions was however also predicted by the thermochemical equilibrium calculations. Moreover these calculations showed that in presence of O_2 for the $SFUO_2$ sample the presence of Mo can give rise to release of free I_2 by the breaking the CsI bond, as a results of the formation of Cs_2MoO_4. This different behaviour between Mo and Ru, and their reaction with CsI will be studied further in Chapter 5 by separate effect experiments on CsI-Ru and CsI-Mo mixtures.

4.5. DISCUSSION

In this work we simulated the aerosols release from spent nuclear fuel with the aim of understanding the fission product partitioning as a function of aerosol size (AED). The principal question addressed was whether the highly active radioisotopes can be concentrated in the small particles, as this influences the risk evaluation for the population because these particles can be transported over long distances and penetrate deep in the lungs if inhaled.

In our tests indeed a size partitioning of the elements as function of their AED size was observed. For all the tested samples we observed that the highly volatile fission products are enriched in the smaller particle fractions, while the non-volatile elements are concentrated in the bigger particles (first impactor stages with bigger AED>1 μm).

This effect can be related to the aerosol formation mechanism. The smaller particles are formed by the rapid condensation of the vapour and are thus enriched in the high volatile elements. The bigger particles are created by ejection of liquid or solid material from the pellet, and are thus enriched in the low volatile elements retained in the matrix. The size partitioning trends observed can be summarized as follows:

- U containing aerosols were found in all AED size fractions as the main constituent of all the aerosols, which is not surprising as it is constituting at least 91% w. of the sample. Raman spectroscopy showed that the chemical form of the uranium aerosols is U_3O_8 or UO_{2+x}.

- Cs was observed in the smaller particles (high volatile element trend). It was generally detected together with I in a ratio of approximately 1, as it was insert as CsI in the simfuel. However, we observed a second source for Cs release as SEM/EDX analysis showed aerosols containing Cs but no I. Thermochemical equilibrium calculations predicted the possibility of a separated gaseous release of Cs and I due to reaction with Mo to form a new compound, Cs_2MoO_4. Alternatively, the second release could be related to the vaporization of Cs_2ZrO_3, as CsO and ZrO_2.

- Ru and Mo, which are present in the fuel in the metallic form, were released in the aerosolization experiments in air. It was observed by ICP-MS measurements that they are concentrated in the particles in the smaller size fraction and that partitioning follows the trend of high volatile elements, such as Cs. This is related to their increase volatility due to the formation of oxides in an air environment. Their release could not be observed in the KEMS in vacuum condition, while Mo but not Ru volatilisation was observed in the KEMS experiments with O_2 flow.

- The Pd concentration showed an increase with decreasing particles size, reaching a maximum and then decreasing again in stage 8. A similar size distribution was also observed for Rh, as they are assigned to the same volatility class. Pd was released in the metallic form, as predicted by the thermochemical equilibrium calculations.

- Ce was enriched in the bigger particles which shows that they are preferentially retained in the matrix. From the separate effect studies on the behaviour of Pu in the aerosols (in which Ce was used as Pu simulate) size partitioning between the two elements was observed. Ce was concentrated in the bigger size ranges with respect to U, which was the main phase (in the form of U_3O_8) in the smaller AED particles.

- Nd, La, Sr, Y, Zr, and Ba were difficult to evaluate due to their low concentration in the aerosols. By coupling the results from different experiments it was possible to assess their behaviour. They showed the trend of the low volatile element class (or matrix elements), decreasing their concentration with smaller particles size. Oxide form were predicted from the thermochemical equilibrium studies and observed in the KEMS experiments.

Molecke et al. [15] also studied the fission product enrichment in the aerosols and their respirable size fraction. They performed explosive aerosolization tests on simulated spent nuclear rods, composed of a zircalloy cladding and simulated spent nuclear fuel pellets. However their simulated spent fuels contained only a limited number of fission products (CsI, RuO_2, SrO, Eu_2O_3), which were chosen as representative for the different fission products volatile classes. They concluded that Cs was enriched in the respirable fraction, similar to our results. Furthermore they assessed that the hypothesis of 5% aerosolization in the respirable fraction for spent fuel obtained in calculations by Luna et al. [36] was conservative, as they found that <2% of U was found in the respirable fraction. In our tests a higher concentration of the particles in the respirable fraction was observed, due to the impossibility with the laser impact set-up to perform a scaled explosive fragmentation of the sample. On the other hand our studies provided a more complete investigation of the behaviour of the different fission products in the aerosols, analysing both the particles and the gaseous release by separate experiments and calculations. Thus providing a better understanding of the vaporization process and of the chemical reactions taking place and of their influence on the aerosol characteristics.

Finally we must discuss the difference between simfuel and irradiated fuel and its effect on our observations. The main distinction is related to the differences in the fuel microstructure. In the simfuels the added fission products are predominantly present at the grain boundaries, with the exception of the elements that can dissolve in the UO_2 matrix under equilibrium conditions, such as Zr and the rare earths. Release from simfuel thus takes predominantly places via the high diffusivity grain boundary network. In irradiated fuel, a significant fraction is, however, present in the fuel grains, as atoms dissolved in defects, defects clusters, voids or gas inclusions. Release and vaporization from irradiated fuel is thus more complex, involving also slow diffusion of atoms and gas inclusions in the fuel matrix, and the enhancement of grain boundary diffusion due to the accumulation of fission gas bubbles at these sites [37]. Comparison with the KEMS experiments on irradiated fuel in vacuum [38] shows that in that material the release takes place in much broader temperature ranges, the maximum release peak appearing generally at higher temperature (for CsI >1200 K). Hiernaut et al. [38] also studied oxidising conditions, which revealed a shift of the release to lower temperature which was caused by the oxidation of the uranium dioxide matrix, but also in this condition the release of volatile elements continues up to high temperatures. Thus the use of simfuel instead of irradiated fuel will mainly affect the quantities of the fission products released into the gas phase, but not significantly the aerosol formation processes from the gaseous phase.

4.6. CONCLUSIONS

Our studies have shown the importance of coupling different techniques for the evaluation of the aerosols' release. The equilibrium vaporization studies provide information on the release behaviour and on the aerosols gaseous precursors. In

particular these techniques were able to predict the chemical forms of the aerosols, the influence of different environments on the release and to understand the chemical reactions that lead to the formation of new compounds. The laser aerosolization experiments provide the possibility of studying the effect of kinetics, due to the rapidity of our experiments, and the aerosol characteristics (such as the size distribution, the morphology, the elemental partitioning with size, and the chemical composition of the main released phase). A good agreement was obtained between the predicted gaseous aerosol precursors and the aerosols in this study. Finally we must stress the need of separate effect experiments, as complementary to the irradiated nuclear fuel release studies, for a better understanding of the aerosol formation mechanism and of the gaseous release process (e.g. different sources for the gaseous release, chemical reactions, etc.).

From these experiments we can conclude that oxidising conditions for the aerosolization experiments, simulating scenarios in which overheated fuel is in contact with air, will lead to the release of also the metallic fission products (e.g. Ru and Mo). These will concentrate in the smaller AED particles size, together with CsI. This effect can have a high influence on risk associated to the inhalation of aerosols released from spent nuclear fuel, as these elements are highly radio-toxic. Moreover the thermochemical equilibrium calculations show an important effect of the release of the metallic fission products, as they can influence the release of free molecular iodine. These reactions will be further investigated in Chapter 5. On the other hand we observed that Pu, for which a high health risk is associated with its incorporation by inhalation, will be concentrated in the particles with bigger AED. This can have an effect on the risk related to the inhalation of this radio-toxic element. Finally we determined the uranium chemical form in the aerosols to be U_3O_8 and/or UO_{2+x}. These chemical compounds are classified in the low soluble class, but their solubility is higher with respect to the starting material UO_2 [39], moreover the small dimension of these particles (AED <0.18 μm), will lead to faster dissolution kinetics and further increase of their solubility [40]. Thus these particles will constitute also a high risk for the population.

Finally this study has demonstrated a partitioning of the different radioactive elements as function of the AED in the aerosols released from spent nuclear fuel. This is important to consider in simulation codes for Radioactive Dispersion Events (such as ARGOS [41], RODOS [42], HOTSPOT [43]). Currently these codes consider as input the total activity of the source and the quantity dispersed in the respirable fraction, and calculate from these data a homogeneous partitioning of the source activity in the different size ranges. From this assumption the extension and level of the contaminated area are calculated. Our results, showing the redistribution of the radioactive fission products as function of particles size, demonstrate the need of implementing a non-homogeneous activity distribution as input for these codes for spent fuel as the partitioning of the elements is different.

ACKNOWLEDGMENTS

F.G.D. would like to acknowledge the constructive contribution to this work: O. Beneš, B. Cremer, M. Ernstberger, M.A. Hernandez Ceballos, V. Rondinella, M. Sierig, J. Somers, D. Staicu, V. Typleck.

REFERENCES

[1] H.J. Allelein, A. Auvinen, J. Ball, S. Guntay, L.E. Herranz, A. Hidaka, A.V. Jones, M. Kissane, D. Power, and G. Weber. State of the art report on aerosols. Technical report, NEA, Nuclear Energy Agency, 2009.

[2] F.C. Iglesias, B.J. Lewis, P.J. Reid, and P. Elder. Fission products release mechanism during reactor accident conditions. *Journal of Nuclear Materials*, 217:166–172, 1999.

[3] M.P. Kissane. On the nature of aerosols produced during a severe accident of a water-cooled nuclear reactor. *Nuclear Engineering and Design*, 238:2792–2800, 2008.

[4] W. Krischer and M.C. Rubinsten. *The Phébus fission product project.* Elsevier applied science, 1992.

[5] L.E. Herranz, J. Ball, A. Auvinen, D. Bottomley, A. Dehbi, C. Housiadas, P. Piluso, V. Layly, F. Parozzi, and M. Reeks. Progress in understanding key aerosol issues. *Progress in Nuclear Energy*, 52:120–127, 2010.

[6] P.D.W. Bottomley, B. Clément, T. Haste, D. Jacquemain, M. Powers, D.A. Schwarz, B. Teisseire, and R. Zeyen. Final seminar of the Phébus FP programme. *Annals of Nuclear Energy*, 61:1–230, 2013.

[7] A. Andrew Barto, Y.J. Chang, K. Compton, H. Esmaili, D. Helton, A. Murphy, A. Nosek, J. Pires, F. Schofer, and B. Wagner. Consequence study of a beyond-design-basis earthquake affecting the spent fuel pool for a U.S. Mark I boiling water reactor. Technical report, Office of Nuclear Regulatory Research, US Nuclear Regulatory Commission, 2013.

[8] T.E. Collins and G. Hubbard. Technical study of spent fuel pool accident risk at decommissioning nuclear power plants. Technical Report NUREG-1738, ISTP report 141, 2001.

[9] IAEA. Health and environmental aspects of nuclear fuel cycle facilities. Technical report, IAEA, 1996.

[10] Nuclear Regulatory Commission Office of Nuclear Regulatory Research. Spent fuel pool beyond-design-basis earthquake consequence study. In *Regulatory Information Conference (RIC)*, volume Poster, 2014.

[11] A. Dykes and A. Machiels. Criticality risks during transportation of spent nuclear fue:l revision 1. Technical report, EPRI, Electric Power Research Institute, 2008.

[12] R. Alvarez, J. Beyea, K. Janberg, J. Kang, E. Lyman, A. Macfarlane, G. Thompson, and F.N. von Hippel. Reducing the hazards from stored spent power-reactor fuel in the united states. *Science and Global Security*, 11:1–51, 2003.

[13] J. Magill, D. Hamilton, K. Latzenkirchen, M. Tufan, G. Tamborini, W. Wagner, V. Berthou, and A. von Zweidorf. Consequences of a radiological dispersal event with nuclear and radioactive sources. *Science and Global Security*, 15(2):107–132, 2007.

[14] M. A. Molecke, J.E. Brockmann, D.A. Lucero, M. Steyskal, and M.W Gregson. Spent fuel sabotage test program, surrogate and fission product aerosol results. In 47^{th} *Annual Meeting of the INMM*, volume SAND2006-5556C, Paper 116, 2006.

[15] M. A. Molecke, J. E. Brockmann, L. A. Klennert, M. Steyskal, M. W. Gregson, W. Koch, O. Nolte, W. Brücher, G. G. Pretzsch, B. A. Autrusson, and O. Loiseau. Spent fuel sabotage testing: depleted uranium oxide aerosol results. *Packaging, Transport, Storage and Security of Radioactive Material*, 19(2):95–101, 2008.

[16] J.P. Hiernaut, J.Y. Colle, Jonnet J. Pflieger-Cuvellier, R., J. Somers, and C. Ronchi. A Knudsen cell-mass spectrometer facility to investigate oxidation and vaporisation processes in nuclear fuel. *Journal of Nuclear Materials*, 344:246–253, 2005.

[17] J.P. Hiernaut, P. Gotcu, J.Y. Colle, and R.J.M. Konings. Thermodynamic study of actinides and lanthanides during total vaporisation of a very high burn-up UO_2 fuel. *Journal of Nuclear Materials*, 378:349–357, 2008.

[18] C. S. Viswanadham, K. C. Sahoo, T. R. G. Kutty, K. B. Khan, V. P. Jathar, S. Anantharaman, Arun Kumar, and G. K. Dey. Laser pulse heating of nuclear fuels for simulation of reactor power transients. *Pramana - Journal of Physics*, 75(6):1267–1272, 2010.

[19] W. A. Zanotelli, G.D. Miller, and E.W. Johnson. Aerosol characterization from a simulated HCDA: 1979 annual report. 1981. NUREG/CR-2109, MLM-2790, R7 Accessed from http://www.osti.gov/bridge/servlets/purl/972223-KyjlCP/972223.pdf.

[20] C.W. Bale, P. Chartrand, S.A. Degterov, G. Eriksson, K. Hack, R. Ben Mahfoud, J. Melancon, A.D. Pelton, and S. Petersen. Factsage thermochemical software and database. *Calphad*, 26(2):189–228, 2002.

[21] C.W. Bale, E. BÃ©lisle, , P. Chartrand, S.A. Decterov, G. Eriksson, K. Hack, I.-H. Jung, Y.-B. Kang, J. Melancon, A.D. Pelton, C. Robelin, and S. Petersen. Factsage thermochemical software and databases â€“ recent developments. *Calphad*, 33 (2):295–311, 2009.

[22] P.G. Lucuta, B.J. Palmer, H. Matzke, and D.S. Hartwig. Preparation and characterization of simfuel- simulated candu high-burnup nuclear fuel. In *Proceedings of Second International Conference on CANDU fuel*, pages 132–146, 1989.

[23] P.G. Lucuta, R.A. Verrall, H. Matzke, and B.J. Palmer. Microstructural features of simfuel- simulated high-burnup UO_2-based nuclear fuel. *Journal of Nuclear Materials*, 178:48–60, 1996.

[24] V. V. Rondinella and Hj Matzke. Leaching of simfuel in simulated granitic water: comparison to results in demineralized water. *Journal of Nuclear Materials*, 238: 44–57, 1996.

[25] H. S. Kim, C.H. Joung, B.H. Lee, J.Y. Oh, Y.H. Koo, and P. Heimgartner. Applicability of CeO_2 as a surrogate for PuO_2 in a MOX fuel development. *Journal of Nuclear Materials*, 378:98–104, 2008.

[26] A.K. Tyagi, B.R. Ambekar, and M.D. Mathews. Simulation of lattice thermal expansion behaviour of $Th_{(1-x)}Pu_xO_2$ (0.0<x<1.0) using CeO_2 as a surrogate material for PuO_2. *Journal of Alloys and Compounds*, 337(1-2):277–281, 2002.

[27] S.D. Lee, E. G. Snyder, R. Willis, R. Fischer, D. Gates-Anderson, M. Sutton, B. Viani, J. Drake, and J. MacKinney. Radiological dispersal device outdoor simulation test: Cesium chloride particle characteristics. *Journal of Hazardous Materials*, 176(1-3):56–63, 2010.

[28] F. T. Harper, S. V. Musolino, and W. B. Wente. Realistic radiological dispersal device hazard boundaries and ramifications for early consequence management decisions. *Health Physics*, 93(1):1–16, 2007.

[29] F.G. Di Lemma, M. Ernstberger Colle, J.Y., G. Rasmussen, H. Thiele, and R. J. M. Konings. RADES an experimental set up for the characterization of aerosol release from nuclear and radioactive materials. *Journal of Aerosol Science*, 416(1-2):166–172, 2013.

[30] M.A. Basu, R. Mishraa, S.R. Bharadwaja, A.S. Kerkara, K.N.G. Kaimala, S.C. Kumarb, and D. Dasa. Thermodynamic stability of Cs_2ZrO_3 by Knudsen effusion technique. *Journal of Alloys and Compounds*, 314(1-2):96–98, 2001.

[31] T. Muromura, T. Adachi, T. Takeishi, Z. Yoshida, T. Yamamoto, and K. Ueno. Metallic phases precipatated in UO_2 fuel. I phases in simulated fuel. *Journal of Nuclear Materials*, 151:318–326, 1988.

[32] G.C. Allen, I.S. Butler, and N. Anh-Tuan. Characterisation of uanium oxides by micro-raman spectroscopy. *Journal of Nuclear Materials*, 238:17–19, 1987.

[33] D. Manara and B. Renker. Raman spectra of stoichiometric and hyperstoichiometric uranium dioxide. *Journal of Nuclear Materials*, 321:233–237, 2010.

[34] C. Jegou, R. Caraballo, S. Peuget, D. Roudil, L. Desgranges, and M. Magnin. Raman spectroscopy characterization of actinide oxides (U,Pu)O_2: Resistance to oxidation by the laser beam and examination of defects. *Journal of Nuclear Materials*, 405:235–243, 2010.

[35] M. Yamawaki, T. Okaa, M. Yasumoto, and H. Sakurai. Thermodynamics of vaporization of cesium molybdate by means of mass spectrometry. *Journal of Nuclear Materials*, 201:257–260, 1993.

[36] R.E. Luna, K.S. Nuehasuser, and M.G. Vigil. Project source terms for potential sabotage events related to spent fuel shipments. Technical report, Sandia National Laboratories, 1999. http://pbadupws.nrc.gov/docs/ML0106/ML010650451.pdf.

[37] R.J.M. Konings, W. Thierry, and O. Beneš. Predicting material release during a nuclear reactor accident. *Nature Materials*, 14(March), 2015.

[38] J.P. Hiernaut, T. Wiss, D. Papaioannou, R.J.M. Konings, and V.V. Rondinella. Volatile fission products behavior during thermal annealing of irradiated UO_2 fuel oxidised up to U_3O_8. *Journal of Nuclear Materials*, 372:215–225, 2008.

[39] A.F. Eidson. The effect of solubility on inhaled uranium compound clearance: A review. *Journal of Health Physics*, 67(1):1–14, 1994.

[40] J.R. Cooper, G.N. Stradling, H. Smith, and S.E. Ham. The behaviour of uranium-233 oxide and uranyl-233 nitrate in rats. *International Journal of Radiation Biology*, 41(4):421–433, 1982.

[41] ARGOS. Computer software CBRN whitepaper. decision support for emergency management, 2008. Accessed from www.pdc.dk/Argos/downloads/ARGOS_whitepaper.pdf.

[42] RODOS. RODOS: Decision support system for off-site nuclear emergency management in europe, 2000. Accessed from http://www.rodos.fzk.de/Overview/moreinfo.html.

[43] HotSpot. NARAC: Hotspot 2.07.2, computer software, 2011. Accessed from https://narac.llnl.gov/HotSpot/HotSpot.html.

5

A SEPARATE EFFECT STUDY OF THE INFLUENCE OF METALLIC FISSION PRODUCTS ON CsI RADIOACTIVE RELEASE FROM NUCLEAR FUEL

F.G. Di Lemma, J.Y. Colle, O. Beneš, and R.J.M. Konings

The chemistry of cesium and iodine is of main importance to quantify the radioactive release in case of a nuclear reactor accident, or sabotage involving irradiated nuclear materials. We studied the interaction of CsI with different metallic fission products such as Mo and Ru. These elements can be released from nuclear fuel when exposed to oxidising conditions, as in the case of contact of overheated nuclear fuel with air (e.g. in a spent fuel cask sabotage, uncovering of a spent fuel pond, or air ingress accidents). Experiments were performed by vaporizing mixtures of the compounds in air, and analysing the produced aerosols in view of possible gas-gas and gas-aerosol reactions between the compounds. These results were compared with the gaseous species predicted by thermochemical equilibrium calculations and experimental equilibrium vaporization tests using Knudsen Effusion Mass Spectrometry.

Parts of this chapter have been submitted and accepted for publication by the Journal of Nuclear Materials (currently under revision).

5.1. INTRODUCTION

High standards in safety is a key pillar for the civil application of nuclear technology and is necessary for its acceptance by the public. For these reasons extensive research has been performed on the radioactive effects following accidents involving nuclear fuel. Iodine and cesium release has been especially studied due to their volatility and radiological health effects. Moreover in recent years low-volatile metallic elements (e.g. ruthenium and molybdenum) have gained interest, following the observation of their substantial radioactive release during accidents involving oxidising conditions [1]. In these scenarios volatile oxide species such as RuO_3, RuO_4, or MoO_3 can be formed. With our experiments we aim at evaluating the interaction of CsI with these fission products and its effect on the radioactive release. CsI has been chosen as this compound is believed to be one of the stable forms in which Cs and I can be found in the fuel during normal operation [2–4] and a main species released from the fuel under accidental conditions.

Many studies have been conducted on the release of radioactive species as gases or aerosols during accidental conditions (e.g. [5–12]). The technical report "state of the art report on nuclear aerosol" from NEA (Nuclear Energy Agency) of the OECD (Organisation for Economic Co-operation and Development) is an important and complete reference, summarizing the experiments and most important findings on nuclear aerosol release [6]. Following the first studies after the Three Mile Island accident, it was generally accepted that iodine would be present in the reactor coolant system as caesium iodide, and it was suggested it could be partly emitted in volatile form in the containment [13]. Ruthenium and Molybdenum release was generally not investigated, as these elements were thought to be retained in metallic form in the fuel. An important progress in understanding radioactive release was achieved by the Phébus-FP project (1993-2012, [1, 5]). This was an integral test consisting of a scaled PWR, in which core degradation was performed until radioactive release was achieved. With respect to the chemical speciation of iodine the Phébus-FP results showed that "caesium iodide is not the only likely species. The presence of gaseous iodine in the containment model of the Phébus experiments led to the hypothesis that a fraction of the iodine was emitted into the containment in a gaseous form." [13]. Moreover in some tests a higher release of the less-volatile elements was found, such as Ru and Mo [1]. After this project new experimental programs have been launched to try to solve some of new questions that arose, such as the possible reaction of iodine with other chemicals in the reactor, and the release of ruthenium and molybdenum in highly oxidising conditions.

In this context, the interaction of CsI and Mo was investigated by IRSN (Institut de Radioprotection et de Sûreté Nucléaire) in the GAEC (Generation of AErosol in the primary Circuit) facility. CsI and MoO_3 were vaporized in a furnace, and the gaseous species and the aerosols produced were analysed. These studies [14, 15] showed that caesium molybdates were formed due to gaseous reactions. This would lead to the release of gaseous iodine. In the framework of the International Source Term Program

(ITSP) also parallel studies have been performed in a new facility (CHIP, CHemistry of Iodine in the Primary circuit) with the aim of identifying the chemical elements that react with iodine in the primary cooling system after a core degradation accident [16, 17].

Studies of the ruthenium behaviour have focused on its release from UO_2 fuel or simulated ZrO_2 fuel [18–20], and less attention has been given to its interaction with other chemicals. An interesting study was performed by Mun and coworkers [21, 22]. They investigated the interaction of Ru with containment surface materials (stainless steel and paint) to evaluate the possible retention by these materials. Also Holm et al. [23] studied the ruthenium interaction with containment surfaces, focusing on aluminum, copper and zinc. In other experimental tests conducted by Hózer et al. [20] and Vér et al. [24], the interaction of Cs and Ru was studied. Experiments were conducted in a vertical furnace and a thermal gradient quartz tube was used to collect RuO_2, followed by an absorbing NaOH solution to collected the gaseous RuO_x species released. From these experiments they concluded that the presence of Cs could delay the Ru maximum release and lower its concentration in the absorber.

It is thus evident that knowledge of the gas-gas and gas-aerosol reactions in the binary CsI-Mo and CsI-Ru systems in air is important. Our work presented here has the aim of understanding the effect of such reactions on the radioactive release from nuclear fuel and on the aerosol characteristics. These studies help predicting better the source term of spent fuel in accidental events during its storage or transport, and also understanding better the chemical reactions taking place in a reactor during accidental scenarios. In our experiments we have first analysed the aerosol formation for the low volatile fission products and CsI in oxidising conditions, then of their mixtures to understand the effect of their interaction on the aerosol characteristics and finally on the iodine release. The results from the experiments have been compared to the analyses of the vaporization process by thermochemical equilibrium calculations and Knudsen Effusion Mass Spectrometry (KEMS) experiments. These permitted the understanding of the reactions taking place in the gaseous phase and to identify the aerosol precursors.

5.2. EXPERIMENTAL

The aerosol generating set-up applied in our study has been already described in details elsewhere in Chapter 2, and in this paper we summarize some of its important features. Laser heating is used to heat the sample to high temperature, partially melting and vaporizing it. The formed vapour condenses rapidly, forming aerosols, in the chosen cooler environment; in this study air at 1 bar pressure and ca. 23 °C. The time necessary to heat the material from room temperature to the maximum "steady state" is much shorter than the dwell time at high temperature (transients ca. 2 ms, dwell at high temperature ca. 28 ms). Since during heating the melting temperature is exceeded, and the sample will melt rapidly, the vapour generated from ablation of the solid will be minimal. Moreover laser ablation can be excluded for our experiments

due to the low energy density of the laser pulse applied (e.g. tenths of milliseconds with an infrared wavelength).

The aerosols are then collected by different systems, depending on the post-analyses to be conducted (e.g. SEM/EDX, ICP-MS, Raman spectroscopy). Collecting substrates used were Millipore filters or aluminum foils. These latter were used as substrates for the plates of the 8-stage MOUDI impactor (MSP Corporation model 110R). With the impactor we can separate the particles by their AED (Aerodynamic Equivalent Diameter). This permits to analyse the particles separately for different AED size range and consequently to gain information as function of the particle dimensions. An important modification has been made in the set-up compared to our earlier description, consisting of a vertical sample holder to avoid losses in the bends.

The results obtained from the aerosol characterisation have been compared with experiments performed by Knudsen Effusion Mass Spectrometry (KEMS), and with thermochemical equilibrium calculations, performed by FactSage software [25, 26] using the HSC thermodynamic database [27]. These studies were performed to evaluate the gaseous speciation in equilibrium conditions, which helps understanding the chemical interactions and the gaseous aerosol precursors. The KEMS has been described by Hiernaut et al. [28], and it consists of a Knudsen cell coupled with a quadrupole mass spectrometer (with mass range of 1-512 amu). The cell is heated by a tungsten coil, and can be operated in vacuum or with a small flow of different gases (e.g. oxygen). The molecular beam effusing from the cell is directed and collimated into the ion source of a quadrupole mass spectrometer, in order to detect the gaseous species as function of the temperature. Calibration of the system was performed by vaporizing a known quantity of silver, done together with the sample.

The samples tested were pellets obtained by pressing commercial powders (from Alfa Aesar). Pellets of 5 mm were obtained for CsI, Mo, Ru, and for their mixtures. Rapid laser pulses were used to heat and vaporize the pellets. The temperatures reached were different even when applying the same conditions (square laser pulse 3600 W lasting 30 ms), due to the different thermal and surface properties of the tested materials. The pellet surface temperature was measured by fast high temperature pyrometer, as described in Chapter 2 .

In our tests we have used a simplified composition for the samples, and only mixtures of CsI with one metallic fission products (Mo, Ru) have been studied, realising that in the nuclear fuel the chemical form of these elements will be different and more complex. Ru and Mo are present in the fuel in the form of metallic precipitates together with other noble metals, forming the called ϵ-phase (an alloy containing mainly Mo, Ru, Tc, Rh, Pd). The composition of these precipitates changes during reactor operation, following the fission product yields and the oxygen potential in the fuel [29]. The choice of studying the interaction of only Mo and Ru with CsI, was related to the their higher affinity with oxygen, the interest on their release following the results of the Phébus experiments [1] and the possibility of forming mixed compounds with differ-

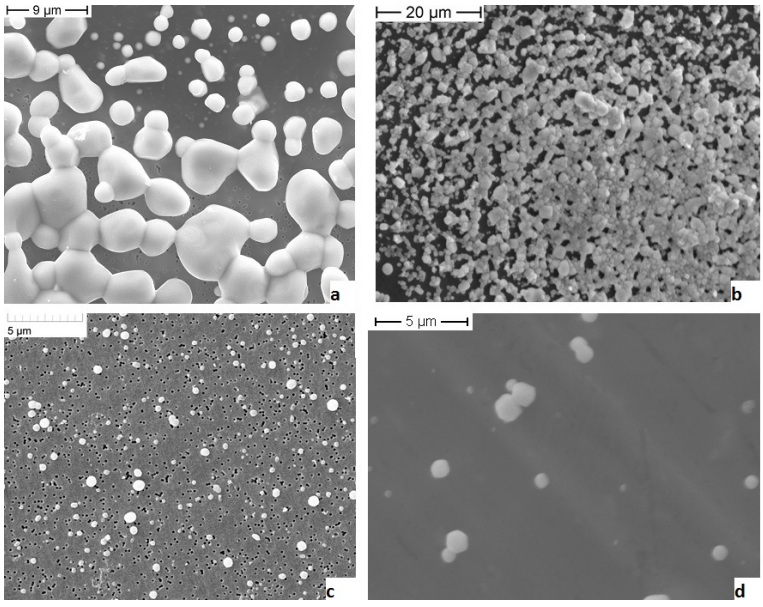

Figure 5.1: SEM image of CsI particles collected on filters (a) and aluminum substrates (b), showing high degree of necking. Influence of the collecting substrate can be noticed for the sample.

ent properties (Cs_2XO_4), which can influence the release of iodine from CsI. The latter compound has been chosen as it has been suggested to be one of the stable forms in which Cs and I can be found in the fuel during normal operation and a main species released from the fuel under accidental conditions.

5.3. RESULTS FOR THE INDIVIDUAL COMPOUNDS

5.3.1. CsI

The aerosols collected were spherical individual particles ranging from 400 nm to micrometer dimension (geometric diameter). Strong necking was observed for these particles. This is related to the theory of coalescence and collision rates [30], which states that when the collision time is smaller than the coalescence time, particles will collide without coagulation forming chain agglomerates. On the other hand when the collision time is longer than the coagulation time, particles will coagulate almost in contact forming bigger spherical particles. Finally, when the collision time is smaller than the coalescence time and this difference is small an intermediate status occurs, leading to the formation of agglomerates with necks, as observed in our experiments (Figure 5.1).

The particles were also analysed by EDX and their composition showed a Cs/I ratio of 1. This indicates that dissociation of this compound during the laser heating did not occur. Just for one test (a square laser pulse of 2500 W for 100 ms, obtaining

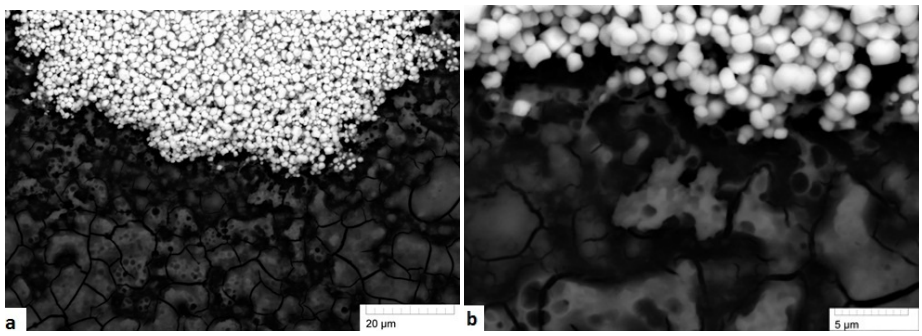

Figure 5.2: CsI particles collected on MOUDI Impactor for the test presenting incongruent vaporization of the compound. On the left (a) CsI particles collected on Cs-rich deposit. On the right (b) a zoom of the liquid layer showing porosity and some brighter areas enriched in I.

a maximum surface temperature of 1400 K) compound dissociation was detected (as observed in Figure 5.2). Since the vaporization of Cs and I as separated species has been calculated to appear in equilibrium condition at very high temperature, we attribute this to the presence of water and the formation of (hydrated) CsOH that leads to low-temperature incongruent vaporization (as reported in [31]). It has been hypothesized that this phenomenon could be related to hydration of the sample due to the storage in not controlled conditions.

5.3.2. MOLYBDENUM AND RUTHENIUM

The results of the aerosol tests for molybdenum were already presented in Chapter 2 . These showed different aerosols morphologies: individual big micrometer spherical particles and agglomerates of smaller nanometric particles were collected, but also nanometric rectangular plates (formed due to high degree of recrystallization in the orthorhombic phase). Raman spectroscopy revealed that the main compound of the aerosols was MoO_3, confirming the formation of the orthorhombic crystal structure.

SEM analyses of the tests performed on ruthenium showed two classes of aerosols based on their morphology. Individual big micrometer spherical particles and string-like agglomerates of smaller nanometric particles were collected (as shown in Figure 5.3), similar to the molybdenum aerosols. They can be related to different formation phenomena [6, 30, 32–34]. The bigger particles are formed by the ejection of the molten material due to thermal-mechanical effects. The nanometric particles are formed from the nucleation and condensation of the released vapour. These nanometric particles agglomerate strongly during transport due to Brownian diffusion and turbulence, forming fractal-like structure. For molybdenum it was not possible to observe clearly these fractal-like structures. In fact Molybdenum gave rise to more primary particles due to the higher quantity of material released and the Mo aerosols fold themselves with increasing primary particles number. These fractal-like agglomerates

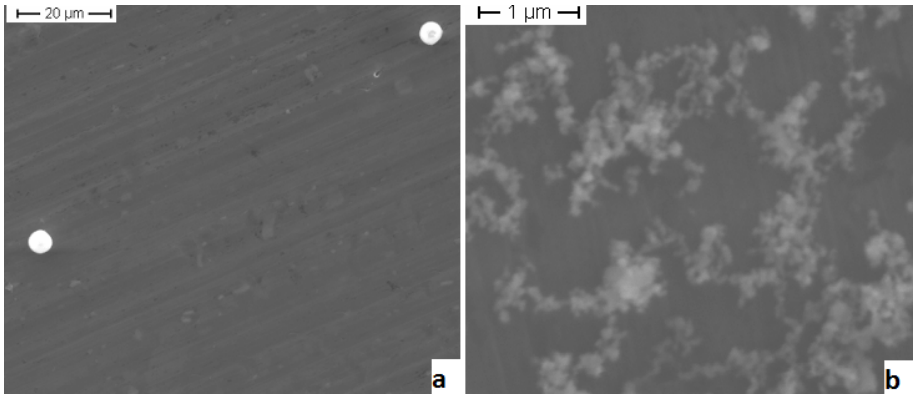

Figure 5.3: Ruthenium particles collected on aluminum substrates by the MOUDI impactor, showing spherical micrometer particles (a) and chain agglomerates of nanometric dimension (fractal-like structures, b).

were collected in the smaller AED size range, while the bigger spherical particles were collected on the first stages of the impactor (with the bigger AED>1 μm). These bigger particles are not the focus of our study because they they are not related to the vaporization process. Elemental and morphological analyses have been performed as a comparison to the nanometric particles, while no Raman spectra were collected for these particles.

The Raman spectra of the collected aerosols showed the bands of RuO_2 (Figure 5.4). This suggests that the ruthenium is vaporized in the oxide form, similar to molybdenum. We observed that the oxidation also occurs on the pellet surface and that the release can thus be enhanced due to the formation of the oxide in the melted layer (as observed also in Chapter 2), as the oxide has a higher volatility with respect to the metallic form.

The Raman spectra of the ruthenium aerosols were compared to those reported for ruthenium oxide films by Meng et al. [35], and showed very similar features. They revealed some modifications with respect to the bulk material (pellet), in particular a broadening and a red-shift of the Raman bands. This shift can be explained by the phonon confinement theory [35, 36], and can be related to the nanometric dimension of the particles. This theory indicates that "if the medium surrounding a nano-grain does not support the vibrational wavenumbers of a material, the optical and acoustic phonons get confined within the grain of the nanostructured material. This leads to interesting changes in the vibrational spectrum of the nanostructured material as compared to that of the bulk....Theoretical models and calculations suggest that the confinement results in asymmetric broadening and shift of the optical phonon Raman line..."[36]. These effects were in fact stronger for the smaller particles collected by the MOUDI impactor on stage 8 with a cut-off size of AED 0.18 μm (gray line) than for the one collected on stage 7 with a bigger AED (with a cut-off size of 0.36 μm, black line).

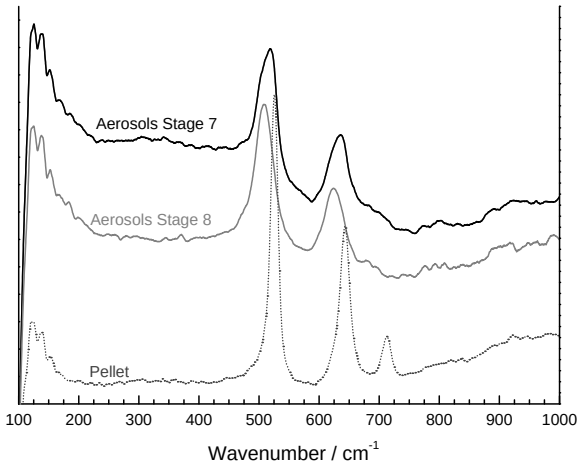

Figure 5.4: Raman spectra measured on the laser-melted pellet and on the aerosols collected on the aluminum substrates. They show the band of RuO_2 and a shift and broadening of the bands for the aerosols, related to the size effect. These effects were stronger for the smaller particles collected by the MOUDI impactor on stage 8 (cut-off size of AED 0.18 μm gray line) than for the one collected on stage 7 with a bigger AED (cut-off size of 0.36 μm, black line).

Table 5.1: Summary of the main results from the aerosol characterisation and thermochemical equilibrium vaporization calculations.

	CsI	Mo	Ru
Laser vaporization	• Particles present high-degree of necking	• Nanometric complex agglomerates	• Fractal like agglomerates
	• Chemical form CsI from EDX analyses	• Chemical form MoO_3 from Raman spectroscopy	• Chemical form RuO_2 from Raman spectroscopy
Equilibrium calculations*	• Cs and I congruent vaporization	• MoO_3 is the main vapour specie released	• RuO_x contribution to the vapour phase is f(T)

* Parameters applied for all calculations were a fixed pressure of 10^5 Pa and fixed O_2 activity at 0.21, using the equilibrium module of Factsage.

Thermochemical equilibrium calculations were performed with the equilibrium

module of FactSage software, a fixed pressure of 10^5 Pa and fixed O_2 activity at 0.21 were used. These conditions have been chosen as our experiments consist of the vaporization of a small amount of material in a comparatively very large vessel at atmospheric pressure in which air flows. In the experiments the gases are free to expand in the vessel environment and then condense, generating the particles. The gaseouse species at equilibrium over the sample tested were analysed as function of the temperature, to predict the gaseous aerosol precursors. A summary of the results obtained is shown in Table 5.1. For Mo the main vapor species is MoO_3 which was also the main aerosol compound detected by Raman spectroscopy. The calculations showed a more complex vapour chemistry for ruthenium as various gaseous oxides will be formed, RuO_3, RuO_4 and RuO_2. Their contribution to the gaseous phase will change as function of temperature. The detection of RuO_2 in the Raman spectra of the aerosols is related to the decomposition of these different gaseous oxides to the most stable Ru oxide solid form (RuO_2).

5.4. RESULTS FOR THE MIXTURES

5.4.1. THE CSI+MO MIXTURE

The tested pellets had a composition of 33 %wt. CsI and 67 %wt. Mo. This composition was chosen as representative for reactor conditions, taking into account that Mo is formed as a fission product but is also constituent of stainless steel (3162), used as structural material (a similar ratio was applied in the experiment "Essai 3" by [14]). The samples were heated by a rapid laser pulse (3600 W for 30 ms) and reached a temperature of 3000-3500 K. These temperatures are higher than those reached with same conditions in tests on pure CsI, which were performed for comparison and is related to the presence of Mo. Molybdenum adsorbs the laser light better and acts as a thermal conductor, distributing the heat to the CsI powder dispersed in the pellet. The higher temperature leads to higher total mass release with respect to the test using only CsI.

AEROSOL MORPHOLOGY AND COMPOSITION

SEM analyses of the collected particles showed several features (as shown in Figure 5.5). On one hand separated aerosols of the starting compounds were found (CsI and MoO_3). These showed similar features as observed for the individual components tested. They were generally collected as spherical particles on the first stages of the MOUDI impactor (Stage 0-2 with bigger AED>5.2 μm) and in the smaller AED as agglomerates. The aerosols collected were predominantly CsI particles with a Cs/I ratio of 1 in these first impactor stages. Mo was also collected on the first stages as spherical individual particles, and after stage 3 (with AED<3.6 μm) in higher quantity in string-like agglomerates. These agglomerates were formed by nanometric particles, which similarly to the pure component aerosols, folded themselves in irregular agglomerates after stage 4 of the MOUDI impactor (AED<1.8 μm).

On the other hand, in the smaller AED (from stage 4 of the MOUDI impactor) also aerosols of irregular shape were found. SEM/EDX analysis showed the presence of the three elements (Cs, I, Mo). The concentrations of these elements were variable, not

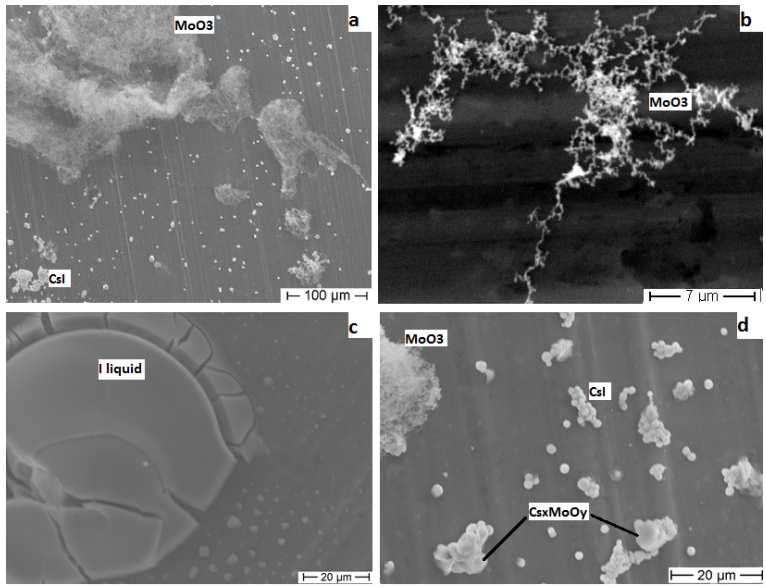

Figure 5.5: SEM/EDX analyses of the CsI+Mo particles collected on MOUDI impactor. On the top left (a) an overview of the particles collected; on the top right (b) the fractal-like agglomerates; on the bottom left (c) the liquid layer enriched in iodine. On the bottom right (d) the spherical bigger CsI particles, the nanometric agglomerates of MoO_3 and the irregular agglomerates containing Cs_2MoO_4 were observed.

permitting an identification. The formation of these mixed aerosols, which contained Cs/I>1, could be a first indication of the formation of caesium molybdate. Another sign of reaction of CsI and MoO_3 was the observation of a deposit of free I in stage 7 (AED of 0.36μm, as shown in Figure 5.5, c) according to equation 5.1:

$$2CsI_{(s)} + Mo_{(s)} + 2O_{2(g)} = Cs_2MoO_{4(s)} + I_{2(g)} \tag{5.1}$$

Raman analyses were also conducted on the collected particles and revealed the chemical composition of the aerosols. For the interpretation of the spectra a comparison has been made with literature data and a standard of Cs_2MoO_4 (INTERFINE CHEMICALS, purity of 99.9%). The results showed the presence of two different aerosols species (as observable in Figure 5.6), as also already inferred from the SEM/EDX analyses. The spectra of the aerosols are in fact a convolution of two compounds when compared with the standards measured:

- MoO_3 (gray solid line), in agreement with literature sources [37, 38].
- Cs_2MoO_4 (gray dashed line), comparable with the data from Lacoue-Negre [14] and our standard.

The MoO_3 aerosols were formed by the vaporization of the Mo in an oxidizing environment, while the cesium molybdates are the result of the interaction of this compound

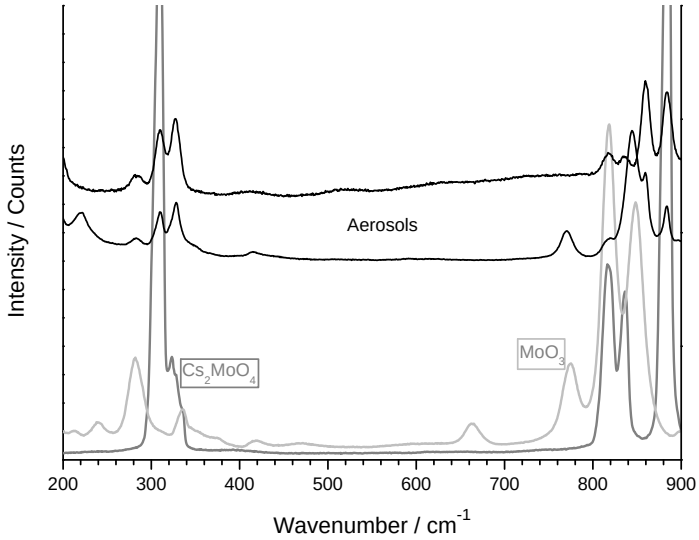

Figure 5.6: Raman spectra obtained for CsI+Mo aerosols collected on the different stages of the MOUDI impactor. This has been compared with the standards measured. The particles showed the typical peaks of MoO_3, but also the presence of caesium molybdates compound spectra.

and CsI. CsI aerosols, which were detected by SEM/EDX, could not be detected by Raman spectroscopy as the vibrations of this compound are Raman inactive.

Finally the pellet surface has been analysed after the laser vaporization to obtain additional information on the vaporization process. The results from the SEM/EDX analysis showed a lower concentration of iodine in the laser heated area. This again demonstrates an in-congruent and preferential vaporization of iodine and suggests that the reaction already partially took place during the heating stage.

THE VAPORIZATION PROCESS

The results of the thermochemical equilibrium simulations, performed with the FactSage software, confirm the formation Cs_2MoO_4 according to reaction 5.1. The formation of this compound is favoured up to high temperature. Moreover it can be observed from equation 5.1, that the formation of Cs_2MoO_4 can lead to a release of molecular iodine $(I_{2(g)})$.

The equilibrium calculations, used to predict the solid phases and gaseous species in an air environment under equilibrium conditions, were performed with a fixed pressure of 10^5 Pa and fixed O_2 activity at 0.21. The chemical composition chosen for the calculations was the one used in our experimental tests 33%wt. CsI and 67%wt.

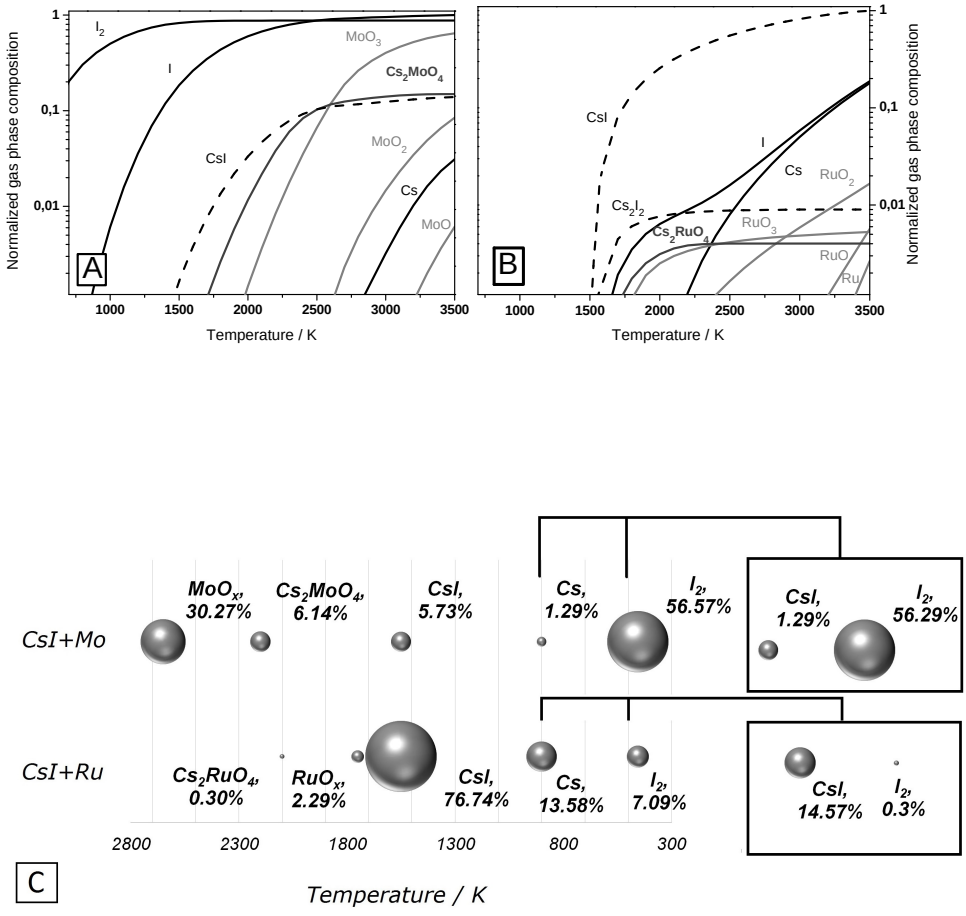

Figure 5.7: Results from the thermochemical equilibrium calculations, showing the chemical composition of the vapour phase as function of the temperature for the two mixtures tested (top) and the total molar concentration of the chemical species in the vapour (bottom). The vapour composition has been used to predict the particles formed. These graphs show the different behaviour for CsI+Mo and CsI+Ru mixtures. The influence of Mo on CsI release will bring to a low temperature release of $I_{2(g)}$ and $I_{(g)}$ in excess (which is incongruent to the one of $Cs_{(g)}$ release), due to the formation of Cs_2MoO_4. For CsI+Ru instead the figure indicates that the formation of Cs_2RuO_4 do not strongly influence the incongruent vaporization of $Cs_{(g)}$ and $I_{(g)}$.

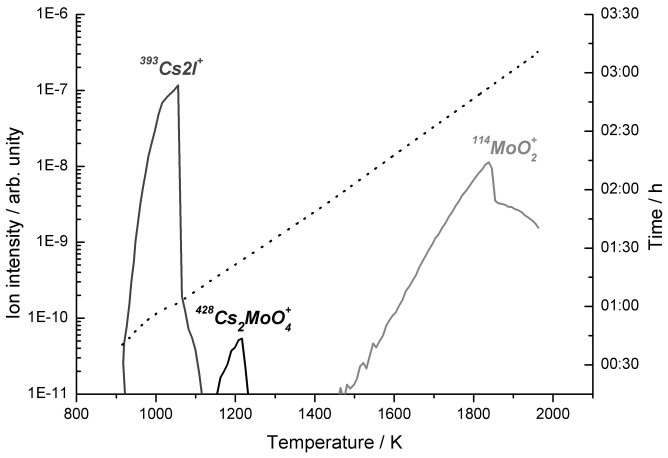

Figure 5.8: Results from the KEMS tests performed on the mixture of CsI+Mo powder. Tests were performed in oxidising condition with a constant flow of oxygen. The mass spectrometer showed the release of Cs_2I^+ shown as representative of the $CsI_{(g)}$ release, followed by the release of $Cs_2MoO_4{}^+$ related to the $Cs_2MoO_{4(g)}$, and finally of the $MoO_2{}^+$ representing $MoO_{3(g)}$ release. This behavior are in good agreement with the thermochemical equilibrium calculations. The fragmentation of the species is related to the electron energy applied for ionization in the mass spectrometer 34 ev.

Mo. The calculations showed that under equilibrium conditions that I_2, Cs_2MoO_4, and MoO_3 are the stable phases, while CsI was not. However, in our tests we performed a rapid quench and non-equilibrium conditions are likely to be achieved. For this reason we have approximated the composition of the aerosols from the calculated cummulative released vapour species in an air environment. Figure 5.7 (a) shows the gas phase composition as function of the temperature (normalized with respect to the maximum value of the total molar release), as obtained from the equilibrium calculations.

The aerosols composition, shown in Figure 5.7 (c), has been obtained by integrating the gaseous molar release over the complete temperature range of the laser vaporization experiments (up to 3500 K, as measured by the pyrometer). This has been performed as the kinetics of gas phase reactions are fast, thus the gaseous species release will be quenched from the gaseous phase to the solid phase, maintaining their chemical composition. In Figure 5.7 the different compound concentrations are presented together with the temperature at which the solid phase is believed to be formed from the gaseous species released (e.g. $MoO_{3(s)}$ from $MoO_{3(g)}$, $MoO_{2(g)}$, $MoO_{(g)}$). As shown in Figure 5.7 (a,c), these calculations confirmed the influence of the CsI-Mo reaction on the release of free $I_{2(g)}$. In these calculations it has been hypothesized that $Cs_{(g)}$ and $I_{(g)}$ will recombine during condensation forming $CsI_{(s)}$. However an excess of I can be observed (related to a low temperature release, as shown in Figure 5.7, a).

This gaseous excess release will then condense to $I_{2(s)}$, which can explain the deposit collected in the laser vaporization experiments on stage 7 of the MOUDI impactor. The release of excess iodine is related to the formation of Cs_2MoO_4 as shown in reaction 5.1. Our calculations, using the vapour composition to predict the aerosols compositions, are in good agreements with the the aerosol characterisation, showing the presence of CsI, MoO_3, Cs_2MoO_4 aerosols and a deposit of I_2. Calculations of the gaseous species released in a constant volume were performed as well and showed in this case no major difference in the release trends.

Finally experiments using KEMS were performed by heating the powder mixture under a controlled flow of oxygen (its vapour pressure was in the range of 1-10 Pa). The release from the mixture was monitored by the mass spectrometer. From this experiment we could confirm the formation and vaporisation of Cs_2MoO_4 in the gaseous phase. The release pattern followed the results of the thermochemical vaporization calculations, showing a first release of $CsI_{(g)}$, followed by the release of the formed $Cs_2MoO_{4(g)}$, and finally of the $MoO_{3(g)}$ (as shown in Figure 5.8).

5.4.2. THE CSI+RU MIXTURE

The pellets were made of equal quantities of CsI and Ru (50/50 %wt.) first, a simplified composition to test the effect of Ru on the release and aerols formation processes In a second experiment the Ru content was increased to 63 %wt. This was performed to collect more RuO_x in order to try to understand thechemical partitioning as a function of the aerosol size for this mixture. The samples were heated by a rapid laser pulse (3600 W for 30 ms). Similar to the CsI+Mo mixture the laser heating brought the sample to a higher temperature compared to CsI only, leading again to higher total mass released, due to the presence of the metal. Aerosols were collected with the MOUDI impactor for post-analyses and again an air environment was used in the experiments.

MORPHOLOGICAL AND CHEMICAL ANALYSIS

The particles collected showed similar features as the mixed sample containing Mo. Fractal-like agglomerates together with big micrometer spherical particles were collected. The bigger particles contained the starting phases. In these tests the aerosols collected were mainly formed by CsI, while ruthenium was collected in all the aerosols in low concentration. This is probably due to its lower volatility with respect to CsI. The only aerosols containing high concentration of Ru were collected on the first stages as crystallized liquid or as individual spherical particles. The formation of these particles can be again related to the ejection of the liquid surface by thermal-mechanical shock. Increasing the Ru content in the pellet did not change drastically this low release. Finally also the EDX analysis confirmed that ruthenium has been preferentially retained in the sample, showing in fact a higher concentration of ruthenium in the pellet melted area.

In the MOUDI stages with smaller AED (<3.6 μm) particles containing Cs and Ru were detected by EDX, similar to the mixed samples test with Mo. To understand if this

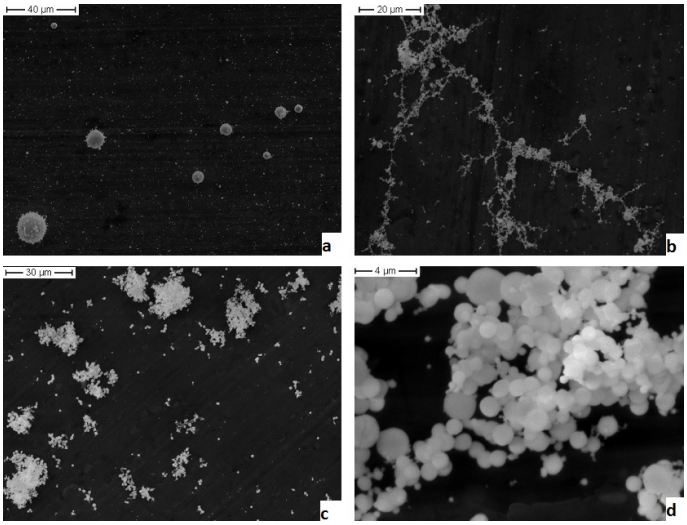

Figure 5.9: Particles collected on the MOUDI impactor plates, for the CsI-Ru mixed pellets. On the top left (a) the bigger spherical particles containing Ru, on the top right (b) agglomerates structures of Ru, on the bottom (c-d) CsI spherical aerosols.

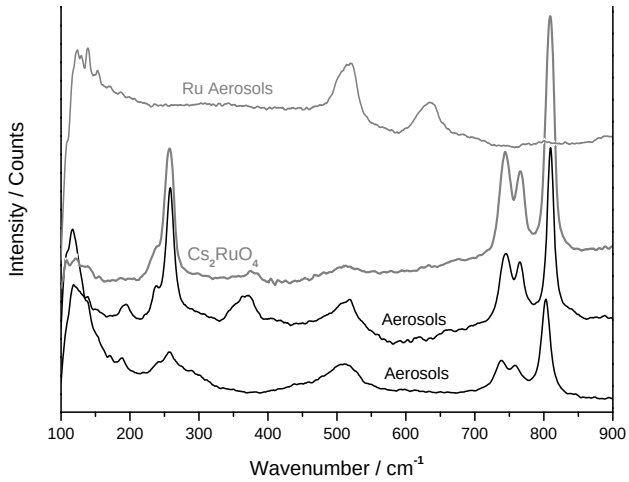

Figure 5.10: Raman spectra collected from the aerosols collected on MOUDI impactor plates for the CsI-Ru mixed sample. The aerosols presents the peak of RuO_2 but also the clear contribution of Cs_2RuO_4 to the spectra.

could be related to the formation of a mixed compound, we analysed the aerosols by Raman spectroscopy (as shown in Figure 5.10). The analyses showed the presence of new bands in the 700-900 cm^{-1} range compared to the initial mixture, which indicate the formation of a mixed compound such as Cs_2RuO_4. In literature no Raman spectrum is present for this compound, but because the iso-structural Cs_2MoO_4 also shows vibrations between 800-900 cm^{-1}, we inferred the formation of Cs_2RuO_4. To demonstrate this a standard of Cs_2RuO_4 was synthesized, following the procedure described by Ball et al. [39], the details of which are reported in [40]. The results clearly confirmed that Cs_2RuO_4 was formed in the aerosols collected in our experiments.

VAPORIZATION PROCESS

The thermochemical equilibrium calculations indicate that Cs_2RuO_4 is formed. This leads again to the formation of free gaseous iodine (as shown in reaction 5.2). This reaction is however favoured just under 1400 K. This, together with the low yield of this reaction, leads to the formation of a low excess of $I_{(g)}$ (<0.3% moles with respect to $Cs_{(g)}$, as shown in Figure 5.7). The formation of solid Cs_2RuO_4 thus has a small influence on the incongruent vaporization of $Cs_{(g)}$ and $I_{(g)}$.

$$2CsI_{(s)} + Ru_{(s)} + 2O_{2(g)} = Cs_2RuO_{4(s)} + I_{2(g)} \tag{5.2}$$

Our vaporization calculations were performed with constant pressure and oxygen activity, with the same parameters applied for the CsI+Mo mixture. The aerosol composition was obtained, as for the precedent sample, by integrating the gaseous molar release up to the temperature of our experiments and approximating the solid composition from that of the vapour. The vapour composition over the sample (CsI/Ru 37/63 %wt.) as function of the temperature is shown in Figure 5.7 (b). These calculations indicate that $CsI_{(g)}$ will be the main phase released during our experiment. At higher temperature gaseous RuO_x species (RuO_3, RuO_4, RuO_2, RuO) will be formed but the released quantity of these oxides will be very low. This explains the small quantity of ruthenium aerosols detected in our experiments. Due to the small excess of free iodine released (as shown in Figure 5.7 (b) from 700 to 1900 K), it was not detected in our tests.

Also for this tests calculations with constant volume were performed and showed that the result could be quite different for these two different conditions. Contrary to what was observed in our experiments, high release of Ru gaseous species (RuO_3, RuO_4, RuO_2, RuO) was predicted with constant volume, together with a small release of CsI. This shows that although the experiments are performed in a closed cell, the fact that the environment is kept at room conditions and not influenced by the insertion of a small amount of gases at high temperature, will permit the free expansion of the gases in the experiments with minimum difference to a free environment.

In the KEMS experiments with this powder mixture the formation of $Cs_2RuO_{4(g)}$ was not observed. This could be due to the low yield of the formation of this compound, as calculated by the thermochemical equilibrium calculations.

Table 5.2: Summary of the main results from the aerosol characterisation and equilibrium vaporization experiments and calculations for the mixture compounds.

	CsI+Mo	CsI+Ru
Composition	33/67%wt.	50/50%wt., 37/63%wt.
Laser vaporization		
	• Particles with Cs/I ratio ≥1/1 by EDX analyses	• Particles with Cs/I ratio 1/1 by EDX analyses
	• MoO_3 particles by Raman spectroscopy	• RuO_2 particles by Raman spectroscopy
	• Cs_2MoO_4 particles by Raman spectroscopy	• Cs_2RuO_4 particles by Raman spectroscopy
	• Deposit of Iodine detected	• No deposit of Iodine
KEMS experiments		
	• Formation of Cs_2MoO_4 detected	• Formation of Cs_2RuO_4 not-detected

* Parameters applied for all calculations were a fixed pressure of 10^5 Pa and fixed O_2 activity at 0.21, using the equilibrium module of Factsage.

5.5. DISCUSSION AND CONCLUSIONS

Our study has shown that the metallic fission products molybdenum and ruthenium can react with CsI in oxidising conditions. This leads to the formation of free (molecular) iodine as a result of the breaking of the CsI bond, due to the formation of new chemical compounds (Cs_2XO_4). For the case of CsI and Mo, this will have a substantial impact as an increase of the iodine gaseous release was observed both in the calculations and also in the experiments. On the other hand Cs will be trapped in the less volatile compounds Cs_2MoO_4 or Cs_2RuO_4 with respect to CsI, but this effect was much smaller in case of Ru. The SEM/EDX analyses and the thermochemical equilibrium calculations have shown that the new compound (Cs_2RuO_4) forms with low yield and it has a small contribution to the total release. Since its vapour pressure is similar to that of the RuO_4, this will not lead to substantial differences in the radioactive release of ruthenium.

For the CsI-Mo sample the experiments showed a dependence of the chemical

composition as function of the particles AED diameter. The smaller particles were mainly composed of MoO_3 agglomerates, while the bigger particles contained mainly CsI. In the middle AED range finally the Cs_2MoO_4 compound was detected. This chemical size partition must be considered when assessing the radiological effects of an environmental release. The size of the particles is in fact one of the most important parameter influencing the air-borne transport and thus the health risks associated with their inhalation. Finally the low release of Ru in the experiments with mixed CsI-Ru powder, did not permit to evaluate such behaviour.

Precedent studies conducted by Gouello et al. and Vér et al. [16, 24] have shown the possibility of reaction of Cs with metallic fission products during nuclear reactor accidental scenarios. Gouello et al. observed the formation of cesium molybdates from CsI and MoO_3 vapours in steam [16] during simulated accidental conditions using a thermal gradient tube, indicating that the reaction could have an effect on the iodine release. Vér et al. observed a delay on the release of Ru when Cs was present [24], and related this to the formation of cesium ruthenate, but its formation was not demonstrated directly. Our laser heating experiments for CsI-Mo and CsI-Ru mixtures in air have clearly demonstrated that these intermediate compounds (Cs_2XO_4) are also formed during very rapid thermal transients in air indicating that the kinetics of the reactions are favorable under these conditions as well. In the case of CsI-Mo we have also observed the concomitant formation of free iodine. Finally, KEMS equilibrium measurements performed in our study on the same mixtures in air showed the formation of Cs_2XO_4 only in case of CsI-Mo mixtures in air, whereas our thermochemical calculations confirmed the stability of both compounds under equilibrium conditions.

These experiments revealed the rapid kinetics of the metal-cesium reactions in air, even in absence of steam, thus demonstrating the importance of these gaseous reactions. From the agreement between the results by the laser heating of the samples and the results for the vapour phase calculated at equilibrium conditions we can conclude that in these studies near-equilibrium conditions were attained. Thal local equilibrium conditions can be obtained with laser heating was previously demonstrated by phase field simulations performed by Welland et al. [41]. On the other hand the quenching of the vapour is a rapid process, limited by reaction kinetics, and agreement with the solid phase predicted by the themochemical calculations is less obvious. Therefore we have used the vapour composition to explain the chemical form of the aerosols collected in our experiments.

It can be concluded that with our experiments we were able to study the size partitioning of the chemical compounds, which could influence the risk associated with the inhalation of such particles in case of a spent fuel pool dry-out or accident during transport of spent nuclear fuel. The formation of Cs_2MoO_4 will lead to formation of Cs-containing particles of smaller AED and release of molecular iodine.

ACKNOWLEDGMENTS

FDL would like to acknowledge the important contribution to this work: D. Bottomley, B. Cremer, M. Ernstberg, K. Mayer. This work is supported by the 7^{th} Framework Program of the European Commission.

REFERENCES

[1] W. Krischer and M.C. Rubinsten. *The Phébus fission product project.* Elsevier applied science, 1992.

[2] J.D. Lambert and K.K. Kadyrzhanov. *Safety Related Issues of Spent Nuclear Fuel Storage.* Springer, 11 edition, 2007.

[3] I. Yoshihiko. Nuclear fuel elements. *JP patent document 55-27939/A/*, page 3, 1980. http://inis.iaea.org/search/search.aspx?orig_q=RN:12596472.

[4] R.J.M. Konings, W. Thierry, and O. Beneš. Predicting material release during a nuclear reactor accident. *Nature Materials*, 14(March), 2015.

[5] P.D.W. Bottomley, B. Clément, T. Haste, D. Jacquemain, M. Powers, D.A. Schwarz, B. Teisseire, and R. Zeyen. Special issue : Phébus FP final seminar. *Annals of Nuclear Energy*, 61:1–230, 2013.

[6] H. J. Allelein, A. Auvinen, J. Ball, S. Güntay, L. Herranz, A. Hidaka, A. V. Jones, M. Kissane, D. Powers, and G. Weber. State of the art report on nuclear aerosol. Technical report, NEA, Nuclear Energy Agency, 2009.

[7] B.R. Bowsher. Fission-product chemistry and aerosol behaviour in the prymary circuit of a pressurized water reactor under severe accident conditions. *Progress in Nuclear Energy*, 20(3):199–233, 1987.

[8] E.H.P. Cordfunke and R.J.M. Konings. The release of fission products from degrade UO_2 fuel: Thermochemical aspects. *Journal of Nuclear Materials*, 201:57–69, 1993.

[9] L.E. Herranz, J. Ball, A. Auvinen, S. Guntay, D. Bottomley, A. Dehbi, C. Housiadas, P. Piluso, V. Layly, F. Parozzi, and M. Reeks. Progress understanding key aerosol issues. *Progress in nuclear energy*, 52:120–127, 2010.

[10] F.C. Iglesias, B.J. Lewis, P.J. Reid, and P. Elder. Fission products release mechanism during reactor accident conditions. *Solid State Ionics*, 53-56:376–382, 1992.

[11] T.S. Kress, R.A. Lorenz, T. Nakamura, and M.F. Osborne. Correlation of recent fission product release data. In *ICHMT INTERNATIONAL SEMINAR "Fission product transport process in reactor accidents"*, number CONF-890546–7, 1989.

[12] B.J. Lewis, W.T. Corse, M.H. Kaye, F.C. Iglesias, P. Elder, R. Dickson, and Z. Liu. Low volatile fission-products release and fuel volatilization during severe accident conditions. *Journal of Nuclear Materials*, 252:235–256, 1998.

[13] B. Clément, L. Cantrel, G. Ducros., F. Funke, L. Herranz, A. Rydl, G. Weber, and C. Wren. State of the art report on iodine chemistry. Technical report, NEA, Nuclear Energy Agency, 2007.

[14] M. Lacoue-Negre. *Iodine Chemistry in the reactor coolant system of a nuclear power plant in case of a severe accident – Study of CsI/MoO_3 mixtures under steam.* PhD thesis, University of Lille, December 2010.

[15] M. Lacoue-Negre, H. Mutelle, and F. Cousin. Speciation of aerosol transported in the primary circuit: A comparative study. In *Proceedings International Conference "Nuclear energy for New Europe 2009"*, page 408.1, 2009.

[16] M. Gouello, H. Mutelle, F. Cousin, S. Sobanska, and E. Blanquet. Analysis of the iodine gas phase produced by interaction of CsI and MoO_3 vapours in flowing steam. *Nuclear Engineering and Design*, 263:462–472, 2013.

[17] C. Mun, B. Clément, and L. Cantrel. The CHIP programme, 2013. http://www.irsn.fr/EN/Research/Research-organisation/Research-programmes/SOURCE-TERM/CHIP/Pages/The-CHIP-Project-4934.aspx.

[18] C. Mun, Cantrel, and C. Madic. Review of literature on ruthenium behavior in nuclear power plant severe accidents. *Nuclear Technology*, 156:332–346, 2006.

[19] C. Mun, J. Colombani, and L. Cantrel. Current status on ruthenium chemistry in the containment of a nuclear reactor in case of a severe accident with air ingression. In *Proceedings of Nuclear Energy for new Europe*, 2009.

[20] Z. Hózer, L. Matus, O. Prokopiev, B. Alföldy, and Csordás-Tóth. Escape ruthenium with high temperature air. Technical report, KFKI, Atome nergia Kutatóintézet, 2002.

[21] C. Mun, L. Cantrel, and C. Madic. Study of RuO_4 decomposition in dry and moist air. *Radiochimica Acta*, 95:643–656, 2007.

[22] C. Mun, J.J. Ehrhardt, J. Lambert, and J. Madic. XPS investigations of ruthenium deposited onto representative inner surfaces of nuclear reactor containment buildings. *Applied Surface Science*, 253:7613–7621, 2007.

[23] J. Holm, H. Glänneskog, and C. Ekberg. Interactions of $RuO_{4(g)}$ with different surfaces in nuclear reactor containments. Technical report, NKS, Nordisk kernesikkerhedsforskning, 2008.

[24] N. Vér, L. Matus, M. Kunstá, J. Osán, Z. Hózer, and A. Pintér. Influence of fission products on ruthenium oxidation and transport in air ingress nuclear accidents. *Journal of Nuclear Materials*, 396:208–217, 2010.

[25] C.W. Bale, P. Chartrand, S.A. Degterov, G. Eriksson, K. Hack, R. Ben Mahfoud, J. Melancon, A.D. Pelton, and S. Petersen. Factsage thermochemical software and database. *Calphad*, 26(2):189–228, 2002.

[26] C.W. Bale, E. Bélisle, , P. Chartrand, S.A. Decterov, G. Eriksson, K. Hack, I.-H. Jung, Y.-B. Kang, J. Melancon, A.D. Pelton, C. Robelin, and S. Petersen. Factsage thermochemical software and databases-recent developments. *Calphad*, 33(2):295–311, 2009.

[27] A. Roine, J. Mansikka-aho, P. Björklund, and Talonen T. Kentala, J.-P. Hsc chemistry database version 6.12. Outotec Research Oy, 1947-2007.

[28] J.P. Hiernaut, J.Y. Colle, Jonnet J. Pflieger-Cuvellier, R., J. Somers, and C. Ronchi. A knudsen cell-mass spectrometer facility to investigate oxidation and vaporisation processes in nuclear fuel. *Journal of Nuclear Materials*, 344:246–253, 2005.

[29] K. Kurosaki, K. Tanaka, M. Osaka, Y. Ohishi, H. Muta, M. Uno, and S. Yamanaka. Chemical states of fission products and actinides in irradiated oxide fuels analyzed by thermodynamic calculation and post-irradiation examination. *Progress in Nuclear Science and Technology*, 2:5–8, 2011.

[30] S. K. Friedlander. *Smoke, Dust, and Haze: Fundamentals of Aerosol Dynamics*. Oxford University Press, 2 edition, 2000.

[31] M.K. Jeon, Shin J.M., J.J. Park, and G.I Park. Simulation of Cs behavior during high temperature voloxidation process using the HSC chemistry code. *Journal of Nuclear Materials*, 430:37–43, 2012.

[32] F. G. Di Lemma, J. Y. Colle, M. Ernstberger, G. Rasmussen, H. Thiele, and R. J. M. Konings. RADES an experimental set-up for the characterisation of arosol release from nuclear and radioactive materials. *Journal of Aerosol Science*, 70:36–49, 2014.

[33] F. T. Harper, S. V. Musolino, and W. B. Wente. Realistic radiological dispersal device hazard boundaries and ramifications for early consequence management decisions. *Health Physics*, 93(1):1–16, 2007.

[34] S.D. Lee, E.G. Snyder, R. Willis, R. Fischer, D. Gates-Anderson, M. Sutton, B. Viani, J. Drake, and J. MacKinney. Radiological dispersal device outdoor simulation test: Cesium chloride particle characteristics. *Journal of Hazardous Materials*, 176(1-3):56–63, 2010.

[35] L.-J. Meng, V. Teixeira, and M.P. dos Santos. Raman spectroscopy analysis of magnetron sputtered RuO_2 thin films. *Thin Solid Films*, 442:93–97, 2003.

[36] A.K. Arora, M. Rajalakshmi, T.R Ravindran, and V. Sivasubramanian. Raman spectroscopy of optical phonon confinement in nanostructured materials. *Journal Raman Spectroscopy*, 38(6):37–43, 2007.

[37] G.-A. Nazri and C. Julien. Far-infrared and Raman studies of orthorhombic MoO_3 single crystal. *Solid State Ionics*, 217:166–172, 1999.

[38] E. Haro-Poniatowskia, M. Jouanneb, J.F. Morhangeb, C. Julienb, R. Diamanta, M. Fernández-Guastia, G.A. Fuentesa, and J.C. Alonso. Micro-Raman characterization of WO_3 and MoO_3 thin films obtained by pulsed laser irradiation. *Applied Surface Science*, 127-129:674–678, 1998.

[39] R.G.J. Ball, E.H.P. Cordfunke, R.J.M. Konings, and M.H. Rand. Thermochemical data acquisition, joint final report. Technical report, Commission of the European Communities, 1991.

[40] M. Naji, F. G. Di Lemma, A. Kovács, O. Beneš, D. Manara, J.Y. Colle, G. Pagliosa, P. Raison, and R. J. M. Konings. Joint raman spectroscopic and quantum chemical analysis of the vibrational features of Cs_2RuO_4. *Submitted*, 2014.

[41] M.J. Welland, W.T. Thompson, B.J. Lewis, and D. Manara. Computer simulations of non-congruent melting of hyperstoichiometric uranium dioxide. *Journal of Nuclear Materials*, 385, Proceedings of the E-MRS 2008 Spring Meeting: Third Symposium on Nuclear Materials:358–363, 2009.

6

JOINT RAMAN SPECTROSCOPIC AND QUANTUM CHEMICAL ANALYSIS OF THE VIBRATIONAL FEATURES OF Cs_2RuO_4

M. Naji, F.G. Di Lemma, A. Kovács, O. Beneš, D. Manara, J.Y. Colle, G. Pagliosa, P. Raison, and R. J. M. Konings

The Raman spectroscopic characterisation of the orthorhombic phase of Cs_2RuO_4 was carried out by means of group theory and quantum chemical analysis. Multiple models based on ruthenate (VI+) tetrahedra were tested and characterisation of all the active Raman modes was achieved. A comparison of Raman spectra of Cs_2RuO_4, Cs_2MoO_4 and Cs_2WO_4 was also performed. Raman laser heating induced a phase transition from an ordered to a disordered structure. The temperature phase transition was calculated from the anti-Stokes/Stokes ratio and compared to the ones measured at macroscopic scale. The phase transition is connected with tilting and/or rotations of RuO_4 tetrahedra which lead to a disorder at the RuO_4 sites.

Parts of this chapter have been submitted and accepted for publication by the Journal of Raman spectroscopy (currently under revision).

6.1. INTRODUCTION

A lot of attention has been devoted to the study of the behaviour of the ruthenium fission product in nuclear reactor accidents [1–9]. This is because of several factors: its high specific activity [6], high radio-toxicity for its isotopes ^{106}Ru (half life = 369 days) and ^{103}Ru (half life = 39.3 days)[7–9] and also to the increase of its quantity with the fuel burn-up (Ru yield is higher for ^{239}Pu than ^{235}U) [3].

In the case of nuclear severe accidents, mainly gaseous and volatile fission products are released from the damaged fuel, while transition metals such as ruthenium present in the irradiated fuel would not be released to any significant extent. However, in highly oxidising atmospheres, especially under steam air conditions, metallic ruthenium can be oxidized to volatile RuO_3 and RuO_4 at moderately high temperature and almost completely released from the damaged fuel [10]. According to the Ellingham diagram, the presence of volatile ruthenium oxides occurs only if the fuel elements (uranium, plutonium) have previously been oxidized [11]. Important conclusions concerning the ruthenium release can be drawn also from the Chernobyl accident. Indeed, the total release of ^{103}Ru was higher than that of ^{137}Cs, corresponding to about 2.9% of the Ru inventory at the start of the accident [12, 13]. Thus, confirming the possibility of the release of ruthenium outside of the fuel matrix.

When it is released out of the fuel matrix, ruthenium can be found in various physico-chemical forms, either in simple oxide like RuO_3 and RuO_4 or in the form of mixed compounds with alkali metals like Cs, e.g. as Cs_2RuO_4, and alkali-earth metals (Ba, Sr) present in large quantity as fission products [3]. Moreover, possible formation of Cs_2RuO_4 could increase the volatility of Ru during an accident [1]. The necessity and importance of studying the Cs-Ru-O system, stand-out first because of the radiological hazards posed by the volatile nature of its oxides and second to make best estimate assessment in terms of nuclear safety issues.

In terms of thermodynamic features, the system Cs-Ru-O was only rudimentary investigated [14–17], no reliable phase diagram has been reported so far in the literature, most probably because of the unstable character of ruthenium compounds.

Cs_2RuO_4 belongs to compounds with the general formula A_2BX_4 [18]. These are known to crystallize in different type of structures like olivine, spinel, and other incommensurate phases [19]. The rich sequence of structural phases makes the study of such compound challenging and calls for a fundamental understanding of the orientational ordering of BX_4 tetrahedra responsible for structure variations.

Raman spectroscopy has been known to provide useful structural information in various hostile environment like in hot-cells [20, 21]. Thus, vibrational studies of such materials are of great importance in identifying fission products and their corresponding phases in the fuel or in the aerosols released. Consequently, in order to address a part of these issues, we investigated the structure of Cs_2RuO_4 at room and high tem-

Table 6.1: Crystal structure parameters obtained from the analyses on the room temperature XRD pattern. Rietveld analysis was performed with the pattern from 20 to 90°

Atom	x	y	z	occ.
Ru1	0.22786	0.25000	0.41787	0.50000
Cs1	0.66740	0.25000	0.41289	0.50000
Cs2	0.48818	0.25000	0.79550	0.50000
O1	0.26607	0.25000	0.54754	0.50000
O2	-0.00432	0.25000	0.414119	0.50000
O3	0.28954	0.50439	0.365442	1.00000

Note: The atomic positions (in fractional coordinates) and site occupation parameters were refined in the space group Pnma. (Note a=8.4973 Å; b= 6.4682 Å; c= 11.4546 Å; Bragg R-factor = 10.3 ; Rf-factor = 9.26).

perature. A complete vibrational study of this compound by means of Raman spectroscopy will be provided. We succeeded to combine group theory analysis and quantum chemical calculation to attribute all of the observed Raman bands. We found a phase transition, induced locally by Raman laser heating experiment.

6.2. EXPERIMENTAL

6.2.1. MATERIAL SYNTHESIS

The polycrystalline sample Cs_2RuO_4 was prepared by solid state reaction of Cs_2O and RuO_2, following the same procedure described in [15]. Cs_2O was obtained from the decomposition of Cs_2CO_3, performed in a furnace at 925 K overnight in a constant flow of purified O_2 gas. The material was contained in an iridium-platinum boat, and heated with a ramp of 10 K/min. The obtained Cs_2O powder was mixed in stoichiometric quantity with RuO_2 powder and heated stepwise in a silver boat up to 700 K in a flow of purified oxygen. The resulting material was then grinded and heated in a gold boat up to 1075 K. The purity of Cs_2RuO_4 powder was confirmed by X-ray diffraction measurement at room temperature.

6.2.2. INSTRUMENTAL METHODS

X-RAY DIFFRACTION

Room temperature X-ray data of the final compound Cs_2RuO_4 was obtained on Bruker D8-Advance diffractometer equipped with a germanium monochromator and using $CuK_{\alpha 1}$ = 1.5406 Å radiation, the data were collected between 10° and 120° with steps of 0.009° (2θ) and a counting time of 8 s per step. The powder was kept in an argon dry glove box before measurement, due to the hygroscopic character of the compound. Then, it was mixed with an Epoxy resin to avoid reaction with humidity during the measurement, which was performed in air. The room temperature X-ray powder pattern of Cs_2RuO_4 was fitted to the calculated one using a full-profile analysis program [22] to minimize the profile discrepancy factor Rp. The refined structural parameters for Cs_2RuO_4 are given in Table 6.1 and shows a good agreement with those reported in [14].

RAMAN SPECTROSCOPY

Raman micro-spectroscopy measurements were carried out with a Horiba Jobin -Yvon T64000 spectrometer, used in the single (for Stokes lines acquisition) and in the triple additive spectrograph configuration (for anti-Stokes/Stokes measurements). Raman backscattering was excited with an Ar^+ laser working at 514.5 nm (2.41 eV). The crystalline powder was loaded inside an argon glove box into a Plexiglas sample holder with a quartz window and was subsequently sealed. The laser was then focused onto the sample using an objective of x50. The power at the surface of the sample was measured by Coherent power-meter placed at the sample position. The Raman spectrometer was calibrated using a Si single crystal, and the correct shift was maintained for all samples. A calibrated white light source combined with a fiber optic was used to correct Raman spectra for instrumental response. The recorded “response" spectrum was compared with a “reference" spectrum having a known output of intensity vs. wavelength. The correction function $f(\lambda)$ is calculated as :

$$f(\lambda) = [reference]/[response] \tag{6.1}$$

Each spectrum acquired is multiplied by the correction factor to yield the corrected spectrum.

6

6.2.3. COMPUTATIONAL DETAILS

The Density Functional Theory (DFT) calculations have been performed by means of the Gaussian09 code [23] using the B3LYP exchange-correlation functional [24, 25]. The small-core relativistic pseudopotentials of the Cologne-Stuttgart group were used for the heavy atoms: that of Ru Mo contained 28 electrons in the core ([Ar] $3d^{10}$, ECP28MDF) [26], that of Cs 46 electrons ([Kr]$4d^{10}$, ECP46MDF) [27], while that of W 60 electrons ([Kr] $4d^{10}$, $4f^{14}$, ECP60MDF) [28]. Basis sets of quadruple-zeta quality were applied for the 4s, 4p, 4d, 5s electrons of Ru and Mo [27] and for the 5s, 5p, 6s electrons of Cs [26] and for the 5s, 5p, 5d and 6s electrons of W [28]. For oxygen the correlation-consistent cc-pVQZ basis set [29] was used. Both singlet and triplet spin multiplicities were considered in all the model structures. The geometry optimizations were performed without any geometry constraint. The harmonic vibrational frequencies together with Raman activities were calculated for these optimized geometries. In order to be consistent with the experimental Raman spectra, the calculated Raman activities were corrected for the wavelength of the excitation laser line (514.5 nm, Ar) [30, 31].

6.3. RESULTS AND DISCUSSION

The Raman band assignment of Cs_2RuO_4 was performed by a coupling of symmetry selection rules as predicted by group theory and quantum chemical analysis. Figure 6.1 shows a representative Raman spectrum of Cs_2RuO_4 in the 200 – 1000 cm^{-1} wavenumber range, measured at room temperature for an excitation line of 514.5 nm and a power of 2 mW at the sample surface. To extract the damping coefficients and frequencies of the characteristic modes, the spectrum was fitted to a sum of Lorentzian

lines (as shown in Figure 6.1). Table 6.2 lists all the frequencies ν and the damping coefficient Γ of the observed bands. All bands exhibit a rather narrow width, and are located below 1000 cm^{-1}, which is the usual case for these kind of A_2XO_4 (A= Na, K, Rb, Cs and X= Mo, W) compounds [32–37]. Moreover, except a change of the background shape when changing the excitation energies (from 2.41 eV to 1.92 eV), we did not observe any significant change either in the intensity nor in the wavenumber of these modes, confirming the non-resonant character of the observed modes.

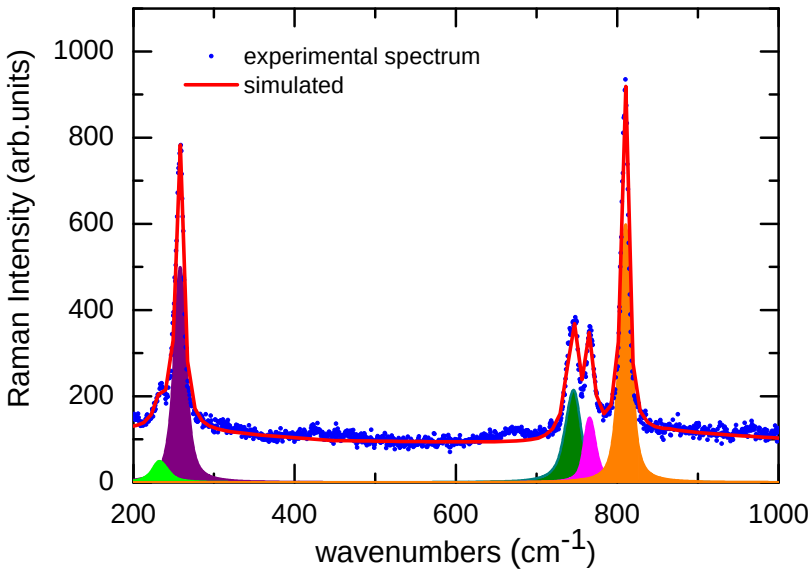

Figure 6.1: Room temperature Raman spectrum of Cs_2RuO_4 (full circles) simulated with a sum of Lorentz bands (solid line). Power at the surface of the sample was 2 mW.

6.3.1. GROUP THEORY ANALYSIS

The room temperature Cs_2RuO_4 crystal structure belongs to space group $Pnma$ with one ruthenium, two caesium and three oxygen independent atoms and it has 4 formula units per unit cell [14].

Applying the group theory analysis (GTA), the fundamental modes at the Γ point *(k=0)* are distributed in terms of the irreducible representations of the factor group D_{2h} as:

$$\Gamma = 13A_g + 8A_u + 8\,B_{1g} + 13B_{1u} + 13B_{2g} + 8B_{2u} + 8B_{3g} + 13B_{3u}.$$

Table 6.2: Comparison of experimental Raman spectrum of Cs_2RuO_4 with the calculated ones of the models RuO_4^{2-}, Cs_2RuO_4 and $Cs_4RuO_4^{2+}$.

Experimental Raman		Calculated			Character
		RuO_4^{2-}	Cs_2RuO_4 (D_{2d})	$Cs_4RuO_4^{2+}$ (D_{2d})	
$\bar{\nu}$ (cm^{-1})	Γ (cm^{-1})	$\bar{\nu}$ (cm^{-1}), *Irr Rep.*	$\bar{\nu}$ (cm^{-1}), *Irr Rep*	$\bar{\nu}$ (cm^{-1}), *Irr Rep.*	
95 w (A_g)			97 (A_1)	72 (A_1)	RuO_2 bend + CsO asym stretch
105 w (B_{3g})			148 (E)	88 (E)	CsO sym stretch
245 w (A_{1g})	16.65	242 (T_2)	325 (A_1)	248 (A_1)	RuO_2 sym bend
270 s (B_g)	10.88	249 (E)	233 (B_1)	303 (B_1)	RuO_2 twist
770 m (B_{2g})	16.6		788 (B_2)	767 (B_2)	RuO asym stretch
780 m (B_{3g})	9.85	747 (T_2)	767 (E)	780 (E)	RuO asym stretch
810 s (A_g)	9.68	808 (A_1)	835 (A_1)	837 (A_1)	RuO sym strech

Where B_{1u}, B_{2u} and B_{3u} are acoustic modes. The vibrations belonging to A_g, B_{1g}, B_{2g} and B_{3g} irreducible representations are Raman active modes.

Since the polarized Raman analysis is not possible in this case (crystalline powder), in order to make a complete assignment of the Raman modes of Cs_2RuO_4 in its orthorhombic phase, we took benefit of two observations : First, the Cs_2RuO_4 spectrum is made of two main envelopes. One asymmetric at low frequency, and a triplet at high frequency. The latter is very likely the sum of bands split from a vibrational mode of higher symmetry. Second, the Cs_2RuO_4 crystalline structure is made of isolated ruthenate RuO_4^{2-} species. Hence, some correlation should exist between their vibrational modes. Therefore, we used the correlation diagram between the "free ion → site group → factor group" to predict the allowed fundamental modes and their consequent splitting (crystal field effect). The correlation diagram is presented in Figure 6.2.

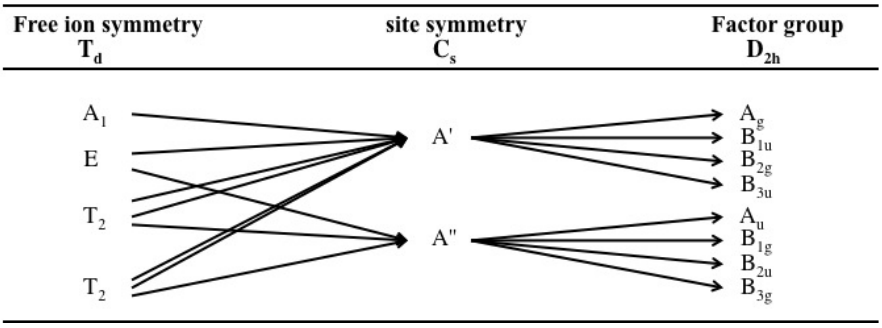

Figure 6.2: Correlation diagram for RuO_4^{2-} in the orthorombic structure. Correlation between T_d point group, C_s site symmetry and D_{2h} factor group.

The free RuO_4^{2-} ion in T_d symmetry exhibits four vibrational Raman active modes A_1, E and $2T_2$. The atomic vector displacement analysis performed through the analysis of the symmetry adapted modes for a given orbit shows that two modes are predominately of stretching type $\nu_1(A_1)$ and $\nu_3(T_2)$ and the rests are bending $\nu_2(E)$, and $\nu_4(T_2)$. Raman tensors related to these irreducible representations predict that all the modes except for A_1 have non-zero polarizability coefficients in the off-diagonal matrix. Therefore, only the A_1 mode is polarized. In the Cs_2RuO_4 crystal, the site symmetry is lower than T_d and the site group analysis allows us to predict the consequent splitting of RuO_4^{2-} ion modes. The doubly and triply degenerate modes (E and T_2) are smoothed out, resulting in the emergence of two bands for ν_2 (A′+A″) and three bands for ν_3 and ν_4 (2A′ + A″). Moreover, the crystal field effect leads to the splitting into eight non-degenerate modes: four for A′ and four for A″ symmetries (Figure 6.2). As said above only vibrations belonging to A_g, B_{1g}, B_{2g} and B_{3g} are Raman active. Thereofore, we have used the GTA analysis to predict all the Raman active modes for Cs_2RuO_4 and we correlated them to those of the RuO_4^{2-} free ion. Now, to assist the assignment

of the Raman spectrum shown in Figure 6.1, we have preformed quantum chemical calculations.

6.3.2. QUANTUM CHEMICAL ANALYSIS

Properly chosen small model structures have often been successfully applied in the literature for characterisation of the main crystal vibrations [38–41]. Such models work well in cases when the main moiety of the compound interacts only weakly with the surroundings. The weak interactions of the RuO_4^{2-} moiety with Cs in crystalline Cs_2RuO_4 satisfies this requirement. We probed three model structures (as shown in

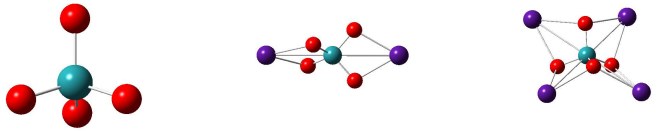

[a] [b] [c]

Figure 6.3: The model structures of: (a) RuO_4^{2-}, (b) Cs_2RuO_4 and (c) $Cs_4RuO_4^{2+}$.

Figure 6.3) for description of the vibrational spectra of solid Cs_2RuO_4. In the crystal, the RuO_4 moieties are distinct units: each Ru is four-coordinated, the four oxygens surround the metal in a distorted tetrahedral arrangement. Our first (simplest) model was the RuO_4^{2-} ion. From the possible two spin multiplicities (singlet, triplet) the triplet one is more stable (by 70 kJ/mol), hence we considered only the data for that state. The Ru-O bond distances of RuO_4^{2-} are in good agreement with the experimental ones (as shown in Table 6.3). Similarly, the calculated Raman spectrum describes well the main features of the experimental Raman spectra (reported in Figure 6.4). These are the symmetric and one of the asymmetric RuO stretching modes at around 800 cm^{-1} and the twisting deformation mode at around 270 cm^{-1}. The wavenumbers are in remarkably good agreement (6.2), while the calculated Raman intensities are too strong in the low-wavenumber part of the spectrum.

Table 6.3: Comparison of selected geometrical parameters (Å, deg.) of Cs_2RuO_4 with the calculated ones of the models RuO_4^{2-}, Cs_2RuO_4 and $Cs_4RuO_4^{2+}$.

Parameter	X-Ray	Calculated		
	Cs_2RuO_4	RuO_4^{2-}	Cs_2RuO_4	$Cs_4RuO_4^{2+}$
Ru-O	1.752-1.774	1.785	1.777	1.777
Cs-O	3.037-3.126	-	2.764	3.026
O-Ru-O	107.4-111.9	109.5	102.9	118/105.4
Ru-O-Cs	106.1-160.8	-	98.4	99.5

The RuO_4 moieties are connected by Cs atoms in the crystal and these Ru-O-Cs interactions (resulting also in the distortion of tetrahedral RuO_4) modify somewhat the vibrations of the RuO_4 moiety with respect to the simple RuO_4^{2-} model. In addition, CsO vibrations appear in the spectra too. The interactions of RuO_4^{2-} with Cs atoms were assessed by two model structures: Cs_2RuO_4 and $Cs_4RuO_4^{2+}$. The second model with two Cs atoms around each oxygen resembles more the surrounding of oxygens in the crystal. Again two spin multiplicities (singlet and triplet) were considered, and the triplets were found to be more stable by 52 and 34 kJ/mol for Cs_2RuO_4 and $Cs_4RuO_4^{2+}$, respectively. These triplet data are presented and discussed in the following.

From the two models the geometrical parameters of $Cs_4RuO_4^{2+}$ agree well with the crystal structure data (cf. Table 6.3). The computed Ru-O bond distance is marginally larger, while the Cs-O bond distance is marginally shorter than those determined for the crystal. Due to the inherent Cs-O interactions in Cs_2RuO_4 as compared to $Cs_4RuO_4^{2+}$ and the solid state, the Cs-O bonds are considerably (by ca. 0.3 Å) shorter in Cs_2RuO_4. This results in considerably stronger Cs-O interactions in the latter model but, does not affect notably the Ru-O interactions, because the Ru-O bond distance is exactly the same as in the $Cs_4RuO_4^{2+}$ model. Therefore, on the basis of the geometrical properties, both models are expected to describe well the vibrations of the RuO_4 moiety, while Cs_2RuO_4 may fail for fundamentals containing significant CsO contribution.

The calculated vibrational spectra of the two models are compared with the experimental one in Figure 6.4. Both models describe well the RuO stretching range of the Raman spectrum with the one intense and two weaker bands in the range of 700-900 cm^{-1}. Also the intense RuO_2 twist around 300 cm^{-1} can be well recognized in the spectra of the two models. Hence the calculations support the attributions of the above mentioned RuO stretching and twisting vibrations based on RuO_4^{2-} model. The weak fundamentals at 325 and 248 cm^{-1} (having the same symmetry and character)in the calculated spectra of Cs_2RuO_4 and $Cs_4RuO_4^{2+}$, respectively, may be associated with the weak feature at 245 cm^{-1} in the experimental spectrum. According to the calculations it may corresponds to RuO_2 bending. We note that the frequency of this vibration in Cs_2RuO_4 is higher by ca. 80 cm^{-1} due to the more strained O-Cs-O arrangement in this model structure.

In general, the calculated Raman spectrum (both the wavenumbers and intensities) of $Cs_4RuO_4^{2+}$ is in somewhat better agreement with the experimental spectrum than the calculated one of Cs_2RuO_4. The latter shows two bands below 200 cm^{-1} with considerable intensity which cannot be recognized in the experimental spectrum. Obviously, this is the consequence of the different CsO interactions in this model. According to the calculations the CsO stretching modes can be expected between 75-300 cm^{-1} mostly mixed with RuO_4 deformation, while the CsO deformation vibrations mixed with RuO_4 deformation probably below 100 cm^{-1}. Two very weak bands can be recognized around 100 cm^{-1} in the Raman spectrum of the solid. The computed data and the proposed characterisation of the experimental Raman bands are compiled in Table 6.2. We note the opposite order in the wavenumbers of the A_1/B_1 deformation and

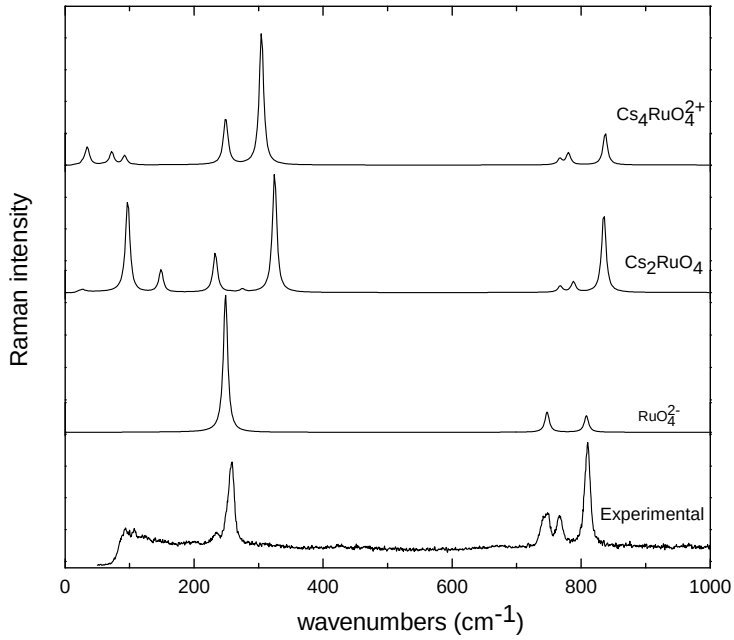

Figure 6.4: Comparison of the experimental Raman spectrum of solid Cs_2RuO_4 (bottom) with the calculated ones of the models RuO_4^{2-}, Cs_2RuO_4 and $Cs_4RuO_4^{2+}$.

B_2/E asymmetric stretching vibrations of the Cs_2RuO_4 and $Cs_4RuO_4{}^{2+}$ models. This is due to the different arrangement of Cs around the $RuO_4{}^{2-}$ moiety in the two model structures.

6.3.3. COMPARISON WITH RUTHENATE AND OTHER TETRAOXY-SPECIES

As stated above, vibrational data on ruthenium tetraoxide and related compounds are lacking from literature. Therefore, we compared our results with those found for liquid ruthenium tetroxide RuO_4 and with the one of crystalline K_2RuO_4 [42, 43]. The Raman spectrum of liquid ruthenium tetroxide exhibits four bands: polarized intense band at 882 cm^{-1} attributed to $\nu_1(A_1)$, a depolarized band at 323 cm^{-1} assigned to $\nu_2(E)$ and two additional bands at 914 cm^{-1} and 334 cm^{-1} to be $\nu_3(T_2)$ and $\nu_4(T_2)$, respectively [42, 43], while for the isostructural K_2RuO_4, the Raman spectrum presents Raman bands related to ν_1, ν_2, ν_3 and ν_4 [43]. Except a slight shift in the wavenumbers our spectrum agrees well with literature. Unfortunately, other oxo-ruthenate related compounds such as Na_2RuO_4, cannot be taken into consideration for a comparison purpose since they do not have the same tetrahedral structural units [44, 45]. In these compounds, ruthenium atoms were found to form trigonal bipyramids [44, 45]. Consequently we have compared the vibrational properties of Cs_2RuO_4 to its molybdate and tungstate analogues. Raman spectra of Cs_2MoO_4 and Cs_2WO_4 were recorded

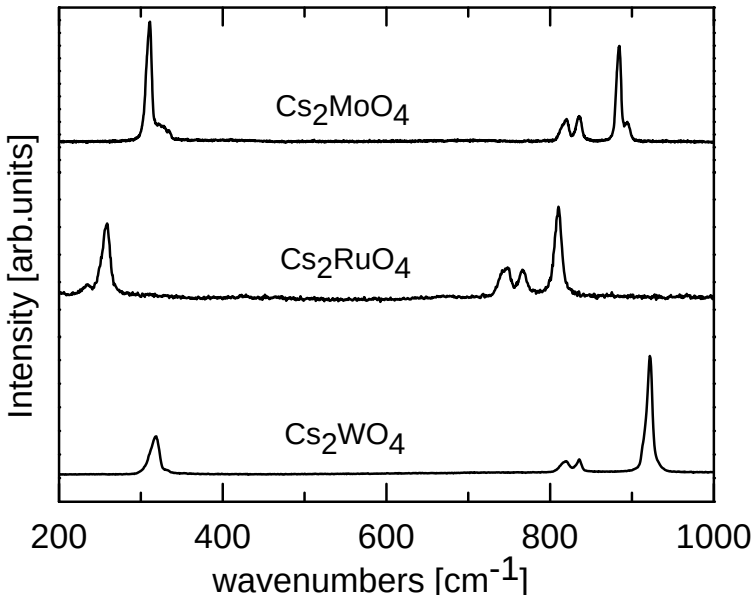

Figure 6.5: Experimental Raman spectra of Cs_2WO_4, Cs_2RuO_4,and Cs_2MoO_4 at room temperature. Power at the surface is 2 mW.

at room temperature under the same conditions described above. The computed Raman spectra of the $WO_4{}^{-2}$, $RuO_4{}^{-2}$, $MoO_4{}^{-2}$ species show the same characteristic differences as the experimental ones (these spectra are shown in Figure 6.5).

In contrast to cubic systems of M_2XO_4 (M= Na, K) and (X= Mo, W) [33, 35], the analogues caesium compounds crystallize in an orthorhombic symmetry. Within the instrumental uncertainty the phonon wavenumbers of Cs_2MoO_4 and Cs_2WO_4 shown in Figure 6.5 agree well with those reported in literature [46]. We note that in [46], the band centered at 881 cm^{-1} for Cs_2MoO_4 was reproduced with only one mode, whereas in our spectrum we observe a small shoulder at 893 cm^{-1} too. A similar band was observed in the high temperature orthorhombic phase of Na_2MoO_4 as well as in its room temperature hydrated one $Na_2MoO_4.xH_2O$ (orthorhombic phase), that is due to the high distortion of the tetrahedral molecular symmetry of MoO_4^{2-} [34]. Regarding Cs_2WO_4, its phonon wavenumbers fit well with the ones reported for Rb_2WO_4 [36]. Comparing MoO_4^{2-} to WO_4^{2-}, the fundamental modes of the latter moiety are generally blue-shifted. The larger stretching frequency of the WO_4 moiety as compared to MoO_4 is attributed to the larger relativistic effects in W, which result in shorter bond distance and larger stretching force constant for WO_4. This feature characteristic for elements in the 5. and 6. rows of the periodic table is well documented [47, 48]. As the shorter

bond distances mean larger electron densities within the bonds, their repulsion can results in larger bending force constants too. Hence the blue shift of the fundamentals of WO_4^{2-}.

As can be seen in Figure 6.5, all the bands of Cs_2RuO_4 are red-shifted with respect to Cs_2MoO_4. This is in agreement with the larger mass of Ru with respect to Mo (being in the same row of the periodic table). The magnitude of the shift, however, may suggest an additional origin. In Cs_2XO_4 (Ru, Mo, W), the electronic configuration of Ru(VI+) is $[Kr]4d^2$, whereas Mo(VI+) and W(VI+) exhibit both d^0 configuration in their valence shell. The electronic structure of the central atom directs towards tetra coordination. While for Cs_2XO_4 (X= Mo, W, Ru) the coordination number of the central atom is the same, the ligand field is different. In RuO_4^{2-} a ligand field stabilization for d^2 occurs being different from those for d^0 configuration. This may induce an effect resulting in a loosening of the force constants, and consequently in red shifts.

6.3.4. LASER HEATING INDUCED PHASE TRANSITION

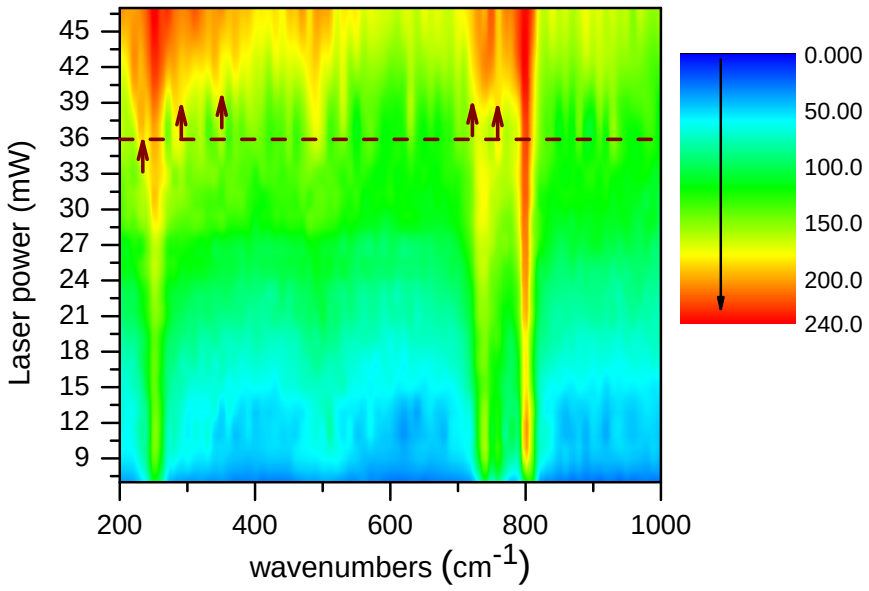

Figure 6.6: 3D plot showing the dependence on laser heating for the Raman spectra of Cs_2RuO_4 heated with 514 nm (Ar+)laser. The x-axis represents the wavenumbers, y-axis shows the laser power measured at the sample surface and z-axis (change of colors) represents the variation of Raman intensity. Intensity increase from blue to red. Arrows indicate appearance of Raman modes above 36 mW (shown with dashed line).

Laser Raman spectroscopy represents a powerful tool for the *in situ* investigation

of structural changes. A large number of laser induced phase transitions and oxidation studies using this technique have been conducted on a wide range of materials. In this experiment, we irradiated the sample surface with different powers and simultaneously collect the Raman spectra. Figure 6.6 represents a three-dimensional plot of Raman spectra acquired at different laser power. The x-axis corresponds to the wavenumber, the y-axis is the laser power measured at the sample surface, while the color change represents the change of the Raman intensity in increasing scale from blue to red. Upon increasing the laser power in the 2-36 mW power range, the Raman spectra remains qualitatively the same. The wavenumbers of all peaks exhibit relatively weak power dependence, except for the band at 237 cm^{-1}, which exhibits a weak band-width change due to the anharmonic effect introduced by the increase of temperature when the laser power is increased. The Raman spectra change drastically above 36 mW (dashed line in Figure 6.6). The changes in the Raman spectra are very impressive *i.e.* some Raman bands split and new bands appear in the wavenumber range between 237-400 cm^{-1} and 700-850 cm^{-1} (illustrated with arrows in Figure 6.6). Appearance of new modes reveal in most cases a reduction of the crystal symmetry, here most probably because of rotational/translational changes of RuO_4 tetrahedra. Furthermore, appearance of these new modes in the Raman spectra is accompanied with an increase of the band-widths of the observed bands indicating that some disorder is introduced in the new structure.

A phase transition for Cs_2RuO_4 was observed by differential scanning calorimetry (DSC) at 907 K by Ball et al. [49]. Moreover some unpublished high temperature phases can be found in ICDD Database for Cs_2RuO_4, these being related to an hexagonal and a tetragonal crystal structures. The former was obtained at 975 K by van Vlaanderen, et al. [50], while the latter one by Range and Wolffram at 423 K [51]. Finally a phase transition has been reported for the iso-structural compound, Cs_2MoO_4 by Wallez et al. [46]. Furthermore, high temperature XRD measurement was performed to evaluate the phase transition of Cs_2RuO_4 (not shown here). Around 875 K the appearance of new bands in the XRD pattern could be observed, this transition was completed at 975 K. The new pattern is similar to the one of van Vlaanderen [50].

The scenario of the laser induced phase transformation could be proposed as follows: from a thermal point of view, the large temperature gradient present in the spot heated by the laser will result in thermal stresses. These induce a gradient of lattice constants and enhance the degree of freedom of species. Thus, permit the rotation and also translation of RuO_4 tetrahedra and Cs atoms, resulting in a more disordered system as indicated by the broadening of the Raman bands. Consequently, the system undergoes a phase transition similar to that reported for Cs_2MoO_4 [46].

The thermal effect of a laser beam is the result of its absorption by the sample. It is evident that the absorptivity of Cs_2RuO_4 in the wavelength range of the laser is very high as shown by the red shifts of bands and also the increase in band-widths. At laser power higher than 36 mW, the heating effect is directly observed by the CCD camera image of thermal radiation from the laser-heated spot. To estimate the temperature

at the surface of the sample, different methods can be used. In this study, we have recorded the Stokes and anti-Stokes lines as a function of the laser power. Figure 6.7 (a) shows some selected Stokes and Anti-Stokes Raman spectra of Cs_2RuO_4 obtained with a stepwise increase in laser power. As described in the experimental methods, the intensities were corrected for the spectral responses of the optical system and the CCD detector (quantum efficiency) and the sample was maintained in a sealed sample holder. Using the following equation (eq. 6.2) based on the Boltzmann distribution of modes between energy levels one can give a good estimate of the temperature at the surface of the irradiated spot.

$$\frac{I_{anti-Stokes}}{I_{Stokes}} = \left(\frac{\nu_0 + \nu_j}{\nu_0 - \nu_j}\right)^4 e^{-\frac{hc\nu_j}{k_B T}} \tag{6.2}$$

where ν_0 and ν_j are the wavenumbers of the excitation line and the Raman modes, respectively, $I_{anti-Stokes}$ and I_{Stokes} are the intensities of the anti-Stokes and Stokes Raman peaks, k_B is the Boltzmann constant, c is the speed of light and T is the temperature. Intensities and wavenumbers of the B_{1g} mode at 270 cm^{-1} were used as input parameters. Figure 6.7 (b) shows the calculated correlations between the laser power and sample temperature. The sample temperature calculated from the

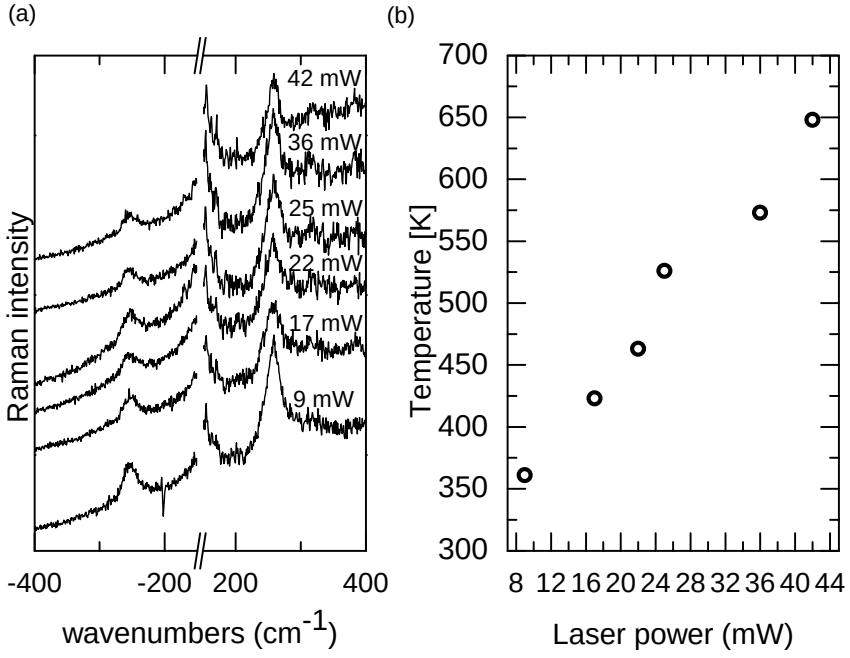

Figure 6.7: (a) Selected Raman spectra collected from Cs_2RuO_4 with a stepwise increase in laser power showing, showing the Stokes and anti-Stokes low wavenumber region [200-400]cm^{-1}. (b) Correlation of the laser power with a local temperature of the sample evaluated with the method described in equation (6.2).

anti-Stokes/Stokes method gives rather satisfactory results and we estimate a phase transition temperature at around 571 K. However one has to be cautious in interpreting these values. The estimation of the accuracy seems to be difficult especially at high powers where the fluorescence level in the spectra becomes more dominant. Furthermore, as all the observed modes broaden at high temperature, the evaluation of their corresponding intensities can be also a source of uncertainty, mainly because of band overlapping (Figure 6.7 (b)).

Prior to conclude on this study, one has to comment the phase transition temperatures obtained from Raman spectroscopy (571 K) and from DSC and XRD data (875-975 K). The temperature measured from the ratio of anti-Stokes/Stokes Raman modes corresponds more or less to a temperature at the sample surface with a size $\sim 1\mu m^2$. Furthermore, it is expected that the central point of the laser beam impact would undergo the greatest heating effect, with a reduction at increasing displacement radii. Thus, the temperature is not uniform in the irradiated surface. The time for the laser to heat the monitored sample area (determined by the diameter of the slit entrance of the spectrometer) to a uniform temperature, must depend on the laser power. Therefore, this reveals the kinetic character of the probed phenomenon. Consequently, the calculated temperature is then an average temperature of probed surface and is different or at least difficult to correlate with the one obtained from DSC or XRD measurements where the sample is held under thermodynamic equilibrium.

6.4. CONCLUSIONS

In this study, we have provided the Raman vibrational features of the orthorhombic phase of Cs_2RuO_4. By coupling group theory to quantum chemical analysis we succeeded to attribute the Raman active modes of its orthorhombic room temperature structure. Raman laser heating caused multiple spectral changes and appearance of new modes characterized by an increase of the band-widths of the bands. Thus suggesting that a phase transition from an ordered to disordered symmetry has occurred. This latter was confirmed by high temperature X-ray measurement. The new structural phase is connected with tiling and or rotations of RuO_4 tetrahedra which, leading to a disorder at the RuO_4 sites. The temperature phase transition was calculated from the anti-Stokes/Stokes ratio and compared to the one obtained from other measurements. Thus, the temperature induced structural changes, must play an important role in the adhesion of the Cs_2RuO_4 at the fuel's surface when undergoing thermal variations.

ACKNOWLEDGEMENTS

The authors would like to acknowledge M. Sierig and D. Bouxiere for their contribution to this work.

REFERENCES

[1] P. Giordano, A. Auvinen, G. Brillant, J. Colombani, N. Davidovich, R. Dickson, T. Haste, T. Karkela, J.S. Lamy, C. Mun, and et al. Recent advances in understanding ruthenium behaviour under air-ingress conditions during a PWR severe accident. *Progress in Nuclear Energy*, 52(1):109–119, 2010.

[2] P. Giordano, A. Auvinen, G. Brillant, J. Colombani, N. Davidovich, R. Dickson, T. Haste, T. Karkela, J.S. Lamy, C. Mun, and et al. Ruthenium behaviour under air ingress conditions: main achievements in the SARNET project. volume 3. 2008.

[3] C. Mun, L. Cantrel, and C. Madic. Review of literature on ruthenium behavior in nuclear power plant severe accidents. *Nuclear technology*, 156(3):332–346, 2006.

[4] A. Auvinen, G. Brillant, N. Davidovich, R. Dickson, G. Ducros, Y. Dutheillet, P. Giordano, M. Kunstar, T. Karkela, M. Mladin, and et al. Progress on ruthenium release and transport under air ingress conditions. *Nuclear engineering and design*, 238 (12):3418–3428, 2008.

[5] L. Soffer, S.B. Burson, C.M. Ferrell, R.Y. Lee, and J.N. Ridgely. Accident source terms for light-water nuclear power plants. final report. Technical report, Nuclear Regulatory Commission, Washington, DC (United States). Division of Systems Technology. Funding organisation: Nuclear Regulatory Commission, Washington, DC (United States), 1995.

[6] J.M. Evrard, C. Marchand, E. Raimond, and M. Durin. Use of PHEBUS FP experimental results for source term assessment and level 2 PSA. In *Proceedings 5th Technical seminar on the Phébus FP programme*, pages 24–26. 2003.

[7] M.E. Frazier, T.K. Andrews, B.B. Thompson, and M.A. Wincek. Technical report, Pacific Northwest Laboratory, Annual Report, 1977.

[8] B. Szubinska and J. H. Luft. Ruthenium red and violet. III. Fine structure of the plasma membrane and extraneous coats in amoebae (A. proteus and chaos chaos). *The Anatomical Record*, 171(3):417–441, 1971.

[9] R. Masse. Le ruthénium, les métaux activés. *Toxiques nucléaires*, pages 112–124, 1982.

[10] D.A Powers, L.N. Kmetyk, and R.C. Schmidt. A review of the technical issues of air ingression during severe reactor accidents. Technical report, Nuclear Regulatory Commission, Washington, DC (United States). Div. of Systems Research, 1994.

[11] C. E. L. Hunt, D.S. Cox, and F.C. Iglesias. Fission-product release during accidents — an accident management perspectives. *Nuclear engineering and design*, 148(2): 205–216, 1994.

[12] H.M. Apsimon and N. Mahadeva. The behaviour of ruthenium isotopes released from Chernobyl. In *Scope-Radpath Workshop*. 1989.

[13] H. Albrecht. Results of the SASCHA program on fission product release under core melting conditions. *Radiochimca Acta*, 41(4):141–144, 1987.

[14] D. Fischer and R. Hoppe. Zur konstitution von oxoruthenaten(VI) 1. Über den aufbau von $Cs_2[RuO_4]$. *Zeitschrift für anorganische und allgemeine Chemie*, 591 (1):87–94, 1990.

[15] E.H.P. Cordfunke, R.J.M. Konings, W. Ouweltjes, and P. van Vlaanderen. The standard enthalpy of formation of Cs_2RuO_4. *The Journal of Chemical Thermodynamics*, 22(3):285–288, 1990.

[16] D. Fischer and R. Hoppe. Über „gemischt-koordinierte" einkernige anionen. 2. Ein Oxoruthenat(VI) neuen Typs: $CsK_5Ru_2O_9 = CsK_5[RuO_5][RuO_4]$. *Zeitschrift für anorganische und allgemeine Chemie*, 617(11):37–44, 1992.

[17] R.G.J. Ball, B.R. Bowsher, E.H.P. Cordfunke, S. Dickinson, and R.J.M. Konings. Thermochemistry of selected fission product compounds. *Journal of Nuclear Materials*, 201:81–91, 1993.

[18] J. Fabry and J.M. Pérez-Mato. Some stereochemical criteria concerning the structural stability of A_2BX_4 compounds of type $\beta - K_2SO_4$. *Phase Transitions: A Multinational Journal*, 49(4):193–229, 1994.

[19] A.R. West. *Solid state chemistry and its applications*. John Wiley & Sons, 2013.

[20] C. Jégou, R. Caraballo, S. Peuget, D. Roudil, L. Desgranges, and M. Magnin. Raman spectroscopy characterization of actinide oxides $(U_{1-y}Pu_y)O_2$: Resistance to oxidation by the laser beam and examination of defects. *Journal of Nuclear Materials*, 405(3):235–243, 2010.

[21] G. Guimbretiere, L. Desgranges, C. Jegou, A. Canizares, P. Simon, R. Caraballo, N. Raimboux, M.-F. Barthe, M.-R. Ammar, O.A. Maslova, F. Duval, and R. Omnee. In *Advancements in Nuclear Instrumentation Measurement Methods and their Applications (ANIMMA)*, pages 1–8. June 2013.

[22] J. Rodriguez-Carvajal. FULLPROF: a program for rietveld refinement and pattern matching analysis. In *Satellite meeting on powder diffraction of the XV congress of the IUCr*, volume 127. 1990.

[23] M.J.E.A. Frisch, G.W. Trucks, Hs. B. Schlegel, G.E. Scuseria, M.A. Robb, J.R. Cheeseman, G. Scalmani, V. Barone, .B Mennucci, G.A. Petersson, and et al. *Inc., Wallingford, CT*, 200, 2009.

[24] A. D. Becke. Density functional thermochemistry. III. The role of exact exchange. *The Journal of Chemical Physics*, 98(7):5648–5652, 1993.

[25] C. Lee, W. Yang, and R. G. Parr. Development of the Colle-Salvetti correlation-energy formula into a functional of the electron density. *Physical Review B*, 37: 785–789, Jan 1988.

[26] I. S Lim, P. Schwerdtfeger, B. Metz, and H. Stoll. All-electron and relativistic pseudopotential studies for the group 1 element polarizabilities from K to element 119. *The Journal of Chemical Physics*, 122(10):104103, 2005.

[27] K. A. Peterson, D. Figgen, M. Dolg, and H. Stoll. Energy-consistent relativistic pseudopotentials and correlation consistent basis sets for the elements Y–Pd. *The Journal of chemical physics*, 126(12):124101, 2007.

[28] D. Figgen, K.A. Peterson, M. Dolg, and H. Stoll. Energy-consistent pseudopotentials and correlation consistent basis sets for the 5d elements hf–pt. *The Journal of Chemical Physics*, 130:164108, 2009.

[29] T. H. Dunning. Gaussian basis sets for use in correlated molecular calculations. I. The atoms boron through neon and hydrogen. *The Journal of Chemical Physics*, 90(2):1007–1023, 1989.

[30] P.L. Polavarapu. Ab initio vibrational Raman and Raman optical activity spectra. *Journal of Physical Chemistry*, 94(21):8106–8112, 1990.

[31] G. Keresztury, S. Holly, G. Besenyei, J. Varga, A. Wang, and J.R. Durig. Vibrational spectra of monothiocarbamates-II. IR and Raman spectra, vibrational assignment, conformational analysis and ab initio calculations of S-methyl-N,N-dimethylthiocarbamate. *Spectrochimica Acta Part A: Molecular Spectroscopy*, 49 (13):2007–2026, 1993.

[32] G.D. Saraiva, C. Luz-Lima, P.T.C. Freire, A.J. Ramiro de Castro, G.P. de Sousa, F.E.A. Melo, J.H. Silva, and J. Mendes Filho. Vibrational and structural properties in the dihydrate sodium tungstate and in the dihydrate sodium molybdate crystals. *Journal of Molecular Structure*, 1033:154–161, 2013.

[33] C. L. Lima, G.D. Saraiva, P.T.C. Freire, M. Maczka, W. Paraguassu, F.F. de Sousa, and J. Mendes Filho. Temperature-induced phase transformations in Na_2WO_4 and Na_2MoO_4 crystals. *Journal of Raman Spectroscopy*, 42(4):799–802, 2011.

[34] C. Luz-Lima, G.D. Saraiva, A.G.S. Filho, W. Paraguassu, P.T.C. Freire, and J. Mendes Filho. Raman spectroscopy study of $Na_2MoO_4 * 2H_2O$ and Na_2MoO_4 under hydrostatic pressure. *Journal of Raman Spectroscopy*, 41(5):576–581, 2010.

[35] G.D. Saraiva, W. Paraguassu, M. Maczka, P.T.C. Freire, J.A. Lima, C.W.A. Paschoal, J. Mendes Filho, and A.G. Souza Filho. Temperature-dependent Raman scattering studies of Na_2MoO_4. *Journal of Raman Spectroscopy*, 39(7):937–941, 2008.

[36] A. Jorio, P. Saint-Gregoire, and M.A. Pimenta. High-temperature phase transitions in incommensurate Rb_2WO_4. *Journal of Physics: Condensed Matter*, 12(44):9307, 2000.

[37] K. Inoue and Y. Ishibashi. Raman scattering study of the phase mode in the incommensurate phase of K_2SeO_4. *Journal of the Physical Society of Japan*, 52(2): 556–561, 1983.

[38] D. Figgen, K.A. Peterson, M. Dolg, and H. Stoll. Molecular models in ab initio studies of solids and surfaces: from ionic crystals and semiconductors to catalysts. *Journal of Chemical Reviews*, 89(1):199–255, 1989.

[39] N. Uchida and S. Masahiro. Mndo study on infrared spectra of silicates. *Journal of Non-Crystalline Solids*, 122(3):276–284, 1990.

[40] J.-L. You, G.-C. Jiang, Hou, H.-Y. H. Chen, Y.-Q. Wu, and K.-D. Xu. Quantum chemistry study on superstructure and raman spectra of binary sodium silicates. *Journal of Raman Spectroscopy*, 36(3):237, 2005.

[41] V. Labet and P. Colomban. Vibrational properties of silicates: A cluster model able to reproduce the effect of "sio4" polymerization on raman intensities. *Journal of Non-Crystalline Solids*, 370:10–17, 2013.

[42] M.H. Ortner. Infrared spectrum and thermodynamic properties of ruthenium tetroxide. *The Journal of Chemical Physics*, 34(2):556–558, 1961.

[43] W.P. Griffith. Studies on transition-metal peroxy-complexes. part VI. Vibrational spectra and structure. *Journal of the Chemical Society A: Inorganic, Physical, Theoretical*, pages 1663–1664, 1968.

[44] K. M. Mogare, K. Friese, W. Klein, and M. Jansen. Structures of two sodium ruthenates: Na_2RuO_4 and Na_2RuO_3 syntheses and crystal. *Zeitschrift für anorganische und allgemeine Chemie*, 630(4):547–552, 2004.

[45] M. Shikano, R. K. Kremer, M. Ahrens, H.-J. Koo, M.-H. Whangbo, and J. Darriet. Synthesis and characterization of a magnetic semiconductor Na_2RuO_4 containing one-dimensional chains of Ru^{6+}. *Inorganic chemistry*, 43(1):5–7, 2004.

[46] G. Wallez, P. E. Raison, A.L. Smith, N. Clavier, and N. Dacheux. High-temperature behavior of dicesium molybdate Cs_2MoO_4: Implications for fast neutron reactors. *Journal of Solid State Chemistry*, 215:225–230, 2014.

[47] J.K. Laerdahl, T. Saue, and K. Faegri Jr. Direct relativistic MP2: properties of ground state CuF, AgF and AuF. *Theoretical Chemistry Accounts*, 97(1-4):177–184, 1997.

[48] M. Iliaš, P. Furdík, and M. Urban. Comparative study of electron correlation and relativistic effects in CuF, AgF, and AuF. *The Journal of Physical Chemistry A*, 102: 5263–5268, 1998.

[49] R.G.J. Ball, E.H.P. Cordfunke, R.J.M. Konings, and M.H. Rand. Thermochemical data acquisition, joint final report. Technical report, Commission of the european communities, 1991.

[50] P. van Vlaanderen. *Energieonderzoek Centrum Nederland, Petten, The Netherlands.*, Private Communication, 1993.

[51] K.-J. Range. Private communication. *Universität Regensburg, Institut für Anorganische Chemie, Germany*, 2000.

7

DISCUSSION AND CONCLUSIONS

7.1. SUMMARY OF THE RESULTS

The aim of this work was to characterise the aerosols released during accidents and sabotage involving nuclear and radioactive materials, focusing on the understanding of the aerosol formation processes and the chemical reactions taking place. Our analyses described the morphology, the size distribution and the chemical and elemental composition of the particles as function of their size (measured by their AED, Aerodynamic Equivalent Diameter). These data are important for the risk assessment, as they can help to improve the assessment of the source term related to different Radiological Dispersion Events (RDE's). They can be used as input for codes determining the extension and level of of the contaminated area (such as ARGOS [1], RODOS [2], HOTSPOT [3]). In particular if following a RDE a partitioning of the radioactivity in the aerosols as function of their size occurs, the results of these codes could be influenced. These codes consider currently only a homogeneous distribution of the radioactivity in the different size ranges. Finally the size characterisation of aerosols is also useful for assessing the risk associated with the inhalation of the radioactive particles released.

A new experimental set-up (RADES, Radiological Dispersion Events Set-up) was developed for the purpose of producing and characterising aerosols from RDE's. This was tested on a wide range of materials and has proven to be suitable for the production and collection of aerosols under controlled laboratory conditions. The set-up permits to analyse the effect of different variables on aerosols characteristics by separate effect studies. In particular the effect of the chemical interactions between different materials or different atmospheres can be investigated. Laser heating was newly applied in our experiments for the production of aerosols from RDE's. Previous studies, as presented in Chapter 1, applied laser heating to investigate thermo-physical properties of radioactive and non-radioactive materials [4–6] or used laser heating only to simulate RIA (Reactivity Initiated Accident) [7, 8]. The choice of a laser heating

technique, over other available heating techniques (e.g. spark generator, furnace technology, plasma generator) is related to specific experimental requirements, such as: avoiding interaction of the sample with supports or heating elements (as laser heating is a self containing system); the possibility of avoiding contamination of the heating system when using radioactive materials; obtaining a precise and flexible control on the heating transient (by a PID controller); and reaching extreme conditions (such as rapid-high-temperature transients).

Moreover the feasibility of different analytical techniques for the characterisation of aerosols, such as SEM/EDX, Raman Spectroscopy, and ICP-MS, was investigated. These analytical techniques have proven to work in synergy to provide a complete characterisation of the aerosol release. For example by the post-analyses of the particles collected with the MOUDI impactor we gained information about the size distribution. By analysing separately each impactor stage by Raman spectroscopy and ICP-MS we investigated the trends of the chemical and elemental composition as function of the particles AED. The morphology and elemental composition of the aerosols was finally studied by SEM/EDX. In addition the aerosol formation process was investigated by studying the aerosol gaseous precursors, using thermochemical equilibrium calculations (by FactSage software [9, 10]) and experimental vaporization studies (with the Knudsen Effusion Mass Spectrometer, KEMS described in [11, 12], and in Appendix B). These techniques permit in fact to study the gaseous release and the chemical reactions, which form the aerosols and influence their chemical compositions.

The RADES set-up was applied to study different release scenarios including dirty bombs detonations, release from simulated spent nuclear fuel under accidental and sabotage scenarios and also to investigate chemical reactions which can influence the radioactive release from nuclear fuel. From the first case studied, dirty bombs detonations, we could identify different morphological features of the aerosols. The aerosols give rise to a bimodal size distribution, consisting of micrometer particles (related to the thermo-mechanical shock on the pellet), and agglomerates of nanometric particles (related to the condensation of the vapour formed). The smaller nanometric particles agglomerate during transport due to the high number of primary particles. The bigger particles instead were collected as spherical particles, which were related to the ejection of liquid material from the laser melted area, and also as solid fragments, released from the un-melted pellet. A similar bimodal size distribution and morphology of the particles were observed also for large scale tests [13, 14]. The authors of these studies performed explosive experiments with simulated Radioactive Dispersion Devices (RDD's, a.k.a. dirty bombs), consisting of explosive and inactive simulates for the radioactive source. They give a similar explanation of the formation of the analysed particles, relating the bigger particle (>10 μm) to the mechanical shock created by the explosion, while the smaller particles were related to the vaporization process. However the fractional release between the two aerosols size ranges cannot be reproduced in our experiments, due to the impossibility to control and scale the shock wave. The mechanical shock in our tests is related only to the thermal shock

on the pellet induced by laser heating and not to an explosive event. The aerosols formed from the vaporization process instead can be simulated, as the experiments permit to reproduce a fast-high-temperature gas release rapidly quenched by a cool air environment. Thus this vaporization process will lead to the formation of nanometric primary particles. On these particles high attention for the risk assessment is focused due to their long range transport in the environment and their high probability of deposition in the lungs when inhaled. Thus our set-up can be applied to study the formation and characteristics of these particles. We do not pretend with our tests to give a complete simulation of a RDD, but instead we aimed at investigating the influence of different variables on the aerosol formation mechanism by separate effect studies, such as the influence of the interaction with other materials.

From the experiments simulating the nanometric aerosols generated by a dirty bomb detonation (as shown in Chapter 3) different features of the particles were observed for the sources tested (CsCl, Ir, Co, $SrTiO_3$). These lead to identify the CsCl source as potentially the most dangerous mainly due to its higher release. In these studies we tested also the influence of cladding materials (tungsten and/or stainless steel) on the aerosols characteristics, while previous studies investigated the influence of soil and/or explosives [13, 14]. From our experiments we identified two different interaction phenomena between source and cladding materials. The first consists of a solid phase agglomeration and was observed when the material did not chemically react with the source tested (for example when applying stainless steel as cladding material). In this case the initial compounds will vaporized separately and condense forming separate primary particles. These will then agglomerate forming mixed agglomerates. In the second case, as observed for tungsten as cladding material, the compounds can react in the gas phase generating a new compound which will then condense. In this case we could detect by Raman spectroscopy a new chemical compound in the aerosols. The formation of the new compound could affect significantly the risk assessment since the radioactive element will be confined in a compound with different thermal-physical properties, influencing its release and the aerosols characteristics. We also tested mixtures of cladding materials to simulated multiple cladding layers. These tests showed that an interaction between multiple claddings can also affect the release as it could prevent the interaction of one of the cladding layers with the source material. It must be investigated if thede interactions could occur in a real RDD explosion. In summary our experiments showed that the claddings can affect the release by the formation of new compounds with different properties or by a different agglomeration behaviour. This can finally lead to a modified size distribution and to a different elemental and chemical speciation of the aerosols as function of their size. This latter effect can influence also a radioactivity partitioning in the aerosols, with finally an effect on the results of codes calculating the radiological consequences of such events. Similar effects were observed when analysing the influence of other materials on the aerosol release [13, 14]. Harper et al. [13] concluded that materials can interact with the radioactive materials by agglomeration and/or coagulation and affect the size of the "radioactive" particles. Thus we can conclude that in their tests no chemical reactions were observed. Lee et al. [14] indicate also an effect of the

soil and explosive on the release of CsCl, such as the formation of mixed aerosols containing both carbonaceous materials and simulated source materials (CsCl), or a different ratio of Cs and Cl in the aerosols. They could not assess the cause of such effects (e.g. chemical reactions or agglomeration phenomena). The comparisons with previous experiments show that by these separate effect studies we can effectively studies the aerosol formation mechanisms, the chemicals reactions, and moreover observe their different influence on the aerosol characteristics. However for the improvement of the simulation of such scenarios, new studies should be conducted with a different system able to deal with non-homogeneous source, and able to simulate the dynamics of the reactions between multiple layer claddings and the radioactive source.

The second study (presented in Chapter 4) had the aim of describing the aerosol release from simulated spent nuclear fuel, in view of accidents and sabotage involving spent fuel storage or during spent fuel transport. Spent fuel safety has become of high interest after the Fukushima accident. While extensive research was performed on release from nuclear reactor accidents [15–25], less work has been performed on release from spent nuclear fuel [26, 27]. In this study laser heating was used to vaporize the simulated spent nuclear fuels and to produce aerosols under repeatable high temperature transients, by the PID control of the laser power. In particular, we wanted to analyse the aerosol size distribution and the fission products partitioning in the different aerosol size ranges, as these can have an effect on the risk assessment by an element specific partitioning in the aerosols. Different simulated spent nuclear fuels were tested and showed a similar trend for the size distribution, morphology and elemental size partitioning of the aerosols. The higher volatile elements were enriched in the smaller particles (e.g. Cs, Ru, Mo), while the lower volatile elements were concentrated in the bigger particles (e.g. Ce, Ba, U as shown in Figure 7.1). A similar effect was observed in explosive tests by Molecke et al. [27]. In these experiments the high volatile elements class, simulated only by CsI, was enriched in the smaller particles (respirable size range), while the matrix elements (CeO_2, or depleted UO_2) were observed in the bigger particles. In our separate effect studies we were further able to correlate this partitioning phenomenon to the aerosol formation mechanism. The smaller particles are formed by the condensation of the vapour release (enriched in high volatile elements), while the bigger particles are formed by the ejection of liquid or solid material from the pellet (enriched in low volatile elements). This partitioning of the radioactive elements as function of size ranges can have a high influence on risk associated to the inhalation, as highly radio-toxic elements are concentrated in the respirable fraction. On the other hand by separate effect studies we observed that the aerosols containing the dangerous radioactive element Pu, simulated by Ce, will be concentrated in the particles with bigger AED. Thus this elemental partitioning can lead to radioactivity redistribution in the aerosols as function of the particles size. Finally uranium was found in high concentration also in the smallest particles (AED <0.18 μm). This will have an influence on its incorporation in the blood if inhaled by humans, as the aerosols of such small dimension will have faster kinetics of dissolution with respect to micrometer particles. Moreover the chemical form of the uranium aerosols, assessed in our study to be U_3O_8 and UO_{2+x}, although in the low soluble

class, will have a faster dissolution with the respect to the starting compound UO_2. Thus they will have a higher health risk.

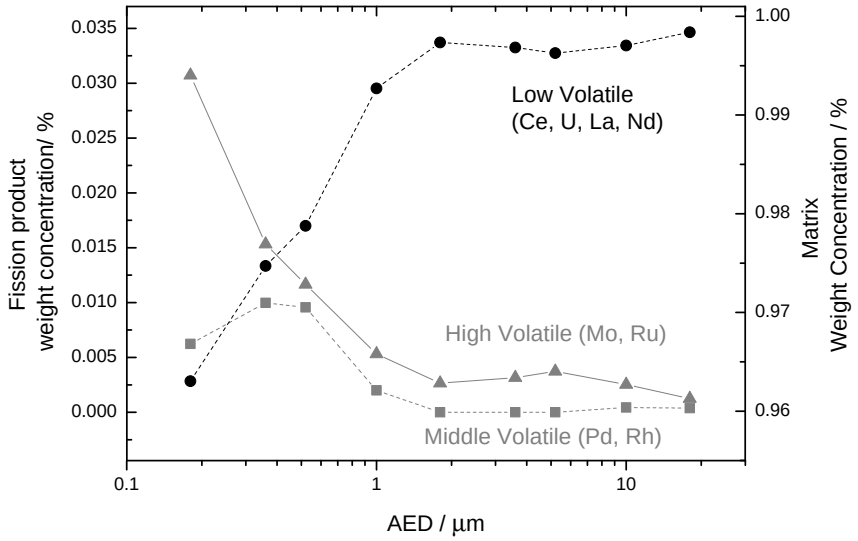

Figure 7.1: Example of trends of the elements in the different volatile class for the AECL simfuels, as already reported in Chapter 4.

These experiments have shown that our novel approach of coupling of the aerosolization experiments on simulated spent nuclear fuel with the equilibrium vaporization studies is effective, as it permits to predict the chemical forms of the fission products in the aerosols, the influence of the oxidising environments on the release (such as the release of metallic fission products) and to understand chemical reactions that lead to the formation of new compounds. In particular the thermochemical equilibrium calculations showed the formation of Cs_2MoO_4 by the interaction of CsI with Mo in the simulate fuel, and a possible effect on the release of free molecular iodine in oxidising conditions. To better study these phenomena we performed some separate effect studies, investigating the vaporization of mixtures containing CsI and metallic fission products, as described in Chapter 5.

The study of the interaction of CsI with low volatile metallic fission products (Mo and Ru) is important, as shown Chapter 4, to understand the reactions taking place during release from spent nuclear fuel. On the other hand these reactions were observed in previous studies [28–30] to be important in nuclear reactor severe accidents, as they could lead to molecular iodine release. In this study the effect of these chemical reactions on the aerosol characteristics and on the iodine gaseous

release have been analysed in more detail. The interaction of these compounds in oxidising conditions can break the CsI bond by the formation of Cs_2XO_4 (X=Mo, Ru) species, releasing gaseous I_2 at low temperature. From our studies it was observed that while the reaction between CsI and Mo will have a strong effect on the release, the reaction between CsI and Ru does not strongly affect the release (in Figure 7.2). It has been shown that these reactions have fast kinetics, as they were observed also in our rapid heating experiments and even in absence of steam. Finally these experiments demonstrated a dependence of the chemical composition as function of the particles AED for the CsI-Mo mixtures. CsI aerosols were collected mainly in the bigger AED>5.6 μm, while the MoO_3 aerosols were collected in the smaller AED<1 μm, and in the middle MOUDI stages with 1 μm<AED<5.6 μm mixed aerosols containing Cs_2MoO_4 were observed.

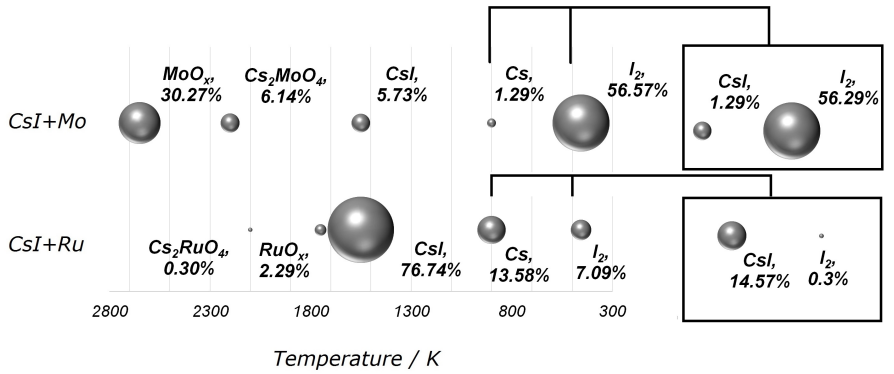

Figure 7.2: Results from the thermo-chemical equilibrium calculations for the two mixtures (CsI-Mo and CsI-Ru), previously shown in Chapter 5.

Following the importance of the formation of these compounds (Cs_2XO_4) on the radioactive release and the lack of a reference Raman spectrum, which is used in this study to identify the chemical composition of the aerosols, a study was performed on the crystal structure and vibrational features of Cs_2RuO_4, *asdescribed* in Chapter 6. The Raman band assignment of Cs_2RuO_4 was performed by a coupling of symmetry selection rules as predicted by group theory and quantum chemical analysis. Finally a phase transition was observed by Raman laser heating, which caused multiple spectral changes and appearance of new modes characterized by broadening of the band-widths. This phase transition was confirmed by high temperature X-ray diffractometer measurement at 975 K, as already reported in literature by DSC measurements [31].

7.2. OUTCOME

The main outcome from our studies can be summarized as follows:

- A new set-up to simulate release from radioactive and nuclear materials under different scenarios (RDD, sabotage or accidents) was successfully built and tested. This set-up was able to produce aerosols under control laboratories conditions and collect them for post-analyses.
- By applying a wide range of post-analyses techniques (such as SEM/EDX, Raman spectroscopy and ICP-MS) we achieved a complete description of the aerosols. The synergy of these techniques permit not only the characterisation of the aerosol size and morphology but also of their chemical form.
- The importance of studying the chemical reactions by thermochemical equilibrium calculations and vaporization studies, which permit to predict the gaseous aerosols precursors, was demonstrated.
- Two different release mechanisms were identified: Solid-Liquid Ejection and vapour condensation. These mechanisms showed a relation to the size distribution (which was bimodal and shown in Figure 7.3), to the morphology of the aerosols and their chemical composition.

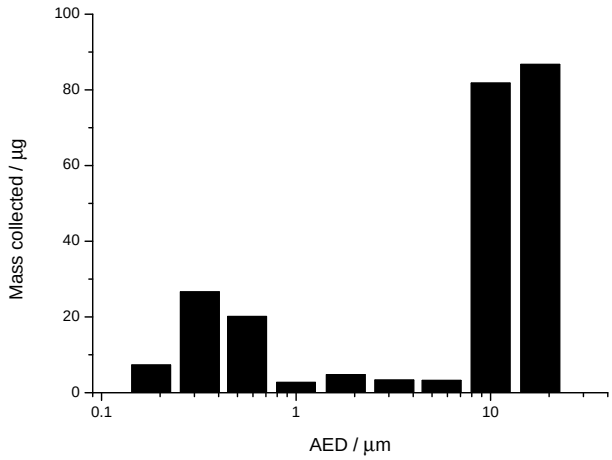

Figure 7.3: Example of size distribution for AECL simfuel showing a bimodal size distribution, as described in Chapter 4.

- It was found that vapour condensation is the most important process because it forms the smaller particles, which are inhalable and deposit deep in the lungs. This process could be simulated with our system, showing that laser heating is a good technique for the study of the aerosols release from RDE's.
- Moreover the importance of chemical reactions, which influence the chemical composition of the vapour released was clearly demonstrated. These interactions can lead to the formation of new chemical compounds, with different

thermal-physical properties influencing the aerosol formation process and the aerosol characteristics. On the other hand it can also lead to the breaking of chemical bonds with increase of gaseous radioactive release.

- Solid phase agglomeration was found to be an important process that can modify the AED size of the particles released.
- A partitioning of the different radioactive elements as function of the aerosols AED was demonstrated, which can lead to inhomogeneous activity in the aerosols as function of their size. This phenomena is generally not taken in account for the predictions of codes calculating the extension and level of the contaminated area after a RDE's.
- Finally it has been demonstrated that these separate effect experiments are necessary for a better understanding of the aerosol formation mechanism, and of the influence of different phenomena on the aerosol characteristics.

7.3. OUTLOOK

The studies describe in this thesis demonstrate that chemical reactions between different compounds during a RDE affect the release and the aerosol formation mechanisms, thus further experiments are strongly recommended for the investigation of the influence of all materials presents in the potential release scenarios. We encourage to perform separate effect studies, as these permit to understand the effect of aerosol formation mechanism and chemical reactions on the release characteristics. In this view we propose further separate effect studies on:

- The interaction of radioactive sources with explosive, other cladding materials, or soil for RDD's simulated release.
- The influence of the cladding or structural materials on release from spent nuclear fuel.
- The chemical reactions relevant for the radioactive release during severe accidents, such as the one between CsI and boron oxides, or silver from the Ag-In-Cd control rods.

Moreover the study of the chemical and elemental partitioning as function of the particles size, as shown in this work, is relevant for the risk assessment following a release, as it can lead to radioactivity size partitioning in the aerosols. This observation must be implemented in the codes to improve the accuracy and reliability of the predictions. In order to improve the results of the calculations these codes must be modified to accept new input parameters, such as non-homogeneous activity distribution as function of particles size. On the other hand this elemental partitioning has also a high impact on nuclear forensics analyses. Analytical techniques on the particles released following a RDE's , such as age determination of the radioactive material by its ratio with the daughter nuclide, will be influenced by an elemental size partitioning. On this topic studies with the RADES system are highly recommended,

analysing the aerosol release from different simulated radioactive sources with dopant to simulate their daughter nuclides.

Moreover as the oxidising environment has shown a high influence on the release, it will be highly suggested to test different gaseous environments (such as Ar/H_2, and steam), in order to investigate further the oxygen potential effect on simulated spent nuclear fuel release and the kinetic limitations acting in these conditions. Finally experiments with PuO_2 and MOX are strongly advised to validate our results with the CeO_2 surrogates, and eventually with real spent fuel.

REFERENCES

[1] ARGOS. Computer software cbrn whitepaper. decision support for emergency management, 2008. Accessed from www.pdc.dk/Argos/downloads/ARGOS_whitepaper.pdf.

[2] RODOS. RODOS: Decision support system for off-site nuclear emergency management in europe, 2000. Accessed from http://www.rodos.fzk.de/Overview/moreinfo.html.

[3] HotSpot. NARAC: Hotspot 2.07.2, computer software, 2011. Accessed from https://narac.llnl.gov/HotSpot/HotSpot.html.

[4] P. D. W. Bottomley, T. Wiss, A. Janssen, B. Cremer, H. Thiele, D. Manara, M. Scheindlin, M. Murray-Farthing, P. Lajarge, M. Menna, D. Bouexiére, and V. V. Rondinella. Characterisation of high temperature refractory ceramics for nuclear applications. *IOP Conference Series: Materials Science and Engineering*, 32(1): 012003, 2012.

[5] D. Manara, M. Sheindlin, W. Heinz, and C. Ronchi. New techniques for high-temperature melting measurements in volatile refractory materials via laser surface heating. *Review of Scientific Instruments*, 79(11):113901–7, 2008.

[6] F. De Bruycker, K. Boboridis, P. Poeml, R. Eloirdi, R. J. M. Konings, and D. Manara. The melting behaviour of plutonium dioxide: A laser-heating study. *Journal of Nuclear Materials*, 416(1-2):166–172, 2011.

[7] C. S. Viswanadham, K. C. Sahoo, T. R. G. Kutty, K. B. Khan, V. P. Jathar, S. Anantharaman, Arun Kumar, and G. K. Dey. Laser pulse heating of nuclear fuels for simulation of reactor power transients. *Pramana- Journal of Physics*, 75(6):1267–1272, 2010.

[8] W. A. Zanotelli, G.D. Miller, and E.W. Johnson. Aerosol characterization from a simulated hcda : 1979 annual report. 1981. NUREG/CR-2109, MLM-2790, R7 Accessed from http://www.osti.gov/bridge/servlets/purl/972223-KyjlCP/972223.pdf.

[9] C.W. Bale, P. Chartrand, S.A. Degterov, G. Eriksson, K. Hack, R. Ben Mahfoud, J. Melancon, A.D. Pelton, and S. Petersen. Factsage thermochemical software and database. *Calphad*, 2002.

[10] C.W. Bale, E. Bélisle, P. Chartrand, I.-H. Jung, Y.-B. Kang, J. Melancon, A.D. Pelton, and S. Petersen. Factsage thermochemical software and databases – recent developments. *Calphad*, 2008.

[11] J.P. Hiernaut, J.Y. Colle, Jonnet J. Pflieger-Cuvellier, R., J. Somers, and C. Ronchi. A Knudsen cell-mass spectrometer facility to investigate oxidation and vaporisation processes in nuclear fuel. *Journal of Nuclear Materials*, 344:246–253, 2005.

[12] J.-P. Hiernaut, P. Gotcu, J.-Y. Colle, and R.J.M. Konings. Thermodynamic study of actinides and lanthanides during total vaporisation of a very high burn-up uo_2 fuel. *Journal of Nuclear Materials*, 378:349–357, 2008.

[13] F. T. Harper, S. V. Musolino, and W. B. Wente. Realistic radiological dispersal device hazard boundaries and ramifications for early consequence management decisions. *Health Physics*, 93(1):1–16, 2007.

[14] S. D. Lee, E. G. Snyder, R. Willis, R. Fischer, D. Gates-Anderson, M. Sutton, B. Viani, J. Drake, and J. MacKinney. Radiological dispersal device outdoor simulation test: Cesium chloride particle characteristics. *Journal of Hazardous Materials*, 176(1-3):56–63, 2010.

[15] P.D.W. Bottomley, B. Clément, T. Haste, D. Jacquemain, M. Powers, D.A. Schwarz, B. Teisseire, and R. Zeyen. Final seminar of the Phébus FP programme. *Annals of Nuclear Energy*, 61:1–230, 2013.

[16] B. Clément, L. Cantrel, G. Ducros., F. Funke, L. Herranz, A. Rydl, G. Weber, and C. Wren. State of the art report on iodine chemistry. Technical report, NEA, Nuclear Energy Agency, 2009.

[17] B.R. Bowsher. Fission-product chemistry and aerosol behaviour in the primary circuit of a pressurized water reactor under severe accident conditions. *Progress in Nuclear Energy*, 20(3):199–233, 1987.

[18] E.H.P. Cordfunke and R.J.M. Konings. The release of fission products from degrade UO_2 fuel: Thermochemical aspects. *Journal of Nuclear Materials*, 201:57–69, 1993.

[19] L.E. Herranz, J. Ball, A. Auvinen, S. Guntay, D. Bottomley, A. Dehbi, C. Housiadas, P. Piluso, V. Layly, F. Parozzi, and M. Reeks. Progress understanding key aerosol issues. *Progress in nuclear energy*, 52:120–127, 2010.

[20] T.S. Kress, R.A. Lorenz, T. Nakamura, and M.F. Osborne. Correlation of recent fission product release data. In *ICHMT International Seminar "Fission product transport process in reactor accidents"*, 1989. CONF-890546-7.

[21] B.J. Lewis, W.T. Corse, M.H. Kaye, F.C. Iglesias, P. Elder, R. Dickson, and Z. Liu. Low volatile fission-products release and fuel volatilization during severe accident conditions. *Journal of Nuclear Materials*, 252:235–256, 1998.

[22] H.J. Allelein, A. Auvinen, J. Ball, S. Guntay, L.E. Herranz, A. Hidaka, A.V. Jones, M. Kissane, D. Power, and G. Weber. State of the art report on nuclear aerosols. Technical report, NEA, Nuclear Energy Agency, 2007.

[23] F.C. Iglesias, B.J. Lewis, P.J. Reid, and P. Elder. Fission products release mechanism during reactor accident conditions. *Solid State Ionics*, 53-56:376–382, 1992.

[24] M.P. Kissane. On the nature of aerosols produced during a severe accident of a water-cooled nuclear reactor. *Nuclear Engineering and Design*, 238:2792–2800, 2008.

[25] W. Krischer and M.C. Rubinsten. *The Phébus fission product project*. Elsevier applied science, 1992.

[26] M. A. Molecke, J.E. Brockmann, D.A. Lucero, M. Steyskal, and M.W Gregson. Spent fuel sabotage test program, surrogate and fission product aerosol results. *47th Annual Meeting of the INMM*, SAND2006-5556C, Paper 116, 2006.

[27] M. A. Molecke, J. E. Brockmann, L. A. Klennert, M. Steyskal, M. W. Gregson, W. Koch, O. Nolte, W. Brücher, G. G. Pretzsch, B. A. Autrusson, and O. Loiseau. Spent fuel sabotage testing: depleted uranium oxide aerosol results. *Packaging, Transport, Storage and Security of Radioactive Material*, 19(2):95–101, 2008.

[28] M. Gouello, M. Lacou-Negre, H. Mutelle, F. Cousin, S. Sobanska, and E. Blanquet. Chemistry of iodine and aerosol composition in the primary circuit of a nuclear power plant. In *Proceedings of ICAPP*, 2011.

[29] M. Lacoue-Negre, H. Mutelle, and F. Cousin. Speciation of aerosol transported in the primary circuit: A comparative study. In *Proceedings International Conference "Nuclear energy for New Europe 2009"*, page 408.1, 2009.

[30] N. Vér, L. Matus, M. Kunstá, J. Osán, Z. Hózer, and A. Pintér. Influence of fission products on ruthenium oxidation and transport in air ingress nuclear accidents. *Journal of Nuclear Materials*, 396:208–217, 2010.

[31] R.G.J. Ball, E.H.P. Cordfunke, R.J.M. Konings, and M.H. Rand. Thermochemical data acquisition, joint final report. Technical report, Commision of the European Communities, 1991.

A

LOSSES CALCULATIONS

Aerosol losses in the RADES systems were calculated with the following formula as reported in [1]. Calculations have been performed for standard conditions and laminar flow. The results of a calculation are reported in Figure A.1, this was performed for the L-tube collection system showed in Chapter 2, for which higher losses are obtained.

$$Losses = (1 - Ptot) * 100 \tag{A.1}$$

where

$$Ptot = Pdiff * Pdep * Pbend \tag{A.2}$$

if $\mu \geq 0.009$

$$Pdiff = 0.819e^{-11.5} + 0.0975e^{-70.1p} \tag{A.3}$$

if $\mu < 0.009$

$$Pdiff = 1 - 5.50p^{2/3} + 3.77p \tag{A.4}$$

where

$$p = 4C_{diff}L/Q \tag{A.5}$$

$$Pdep = 1 - \frac{2}{\pi}(2 * k\sqrt{1-k^{2/3}} - k^{1/3}\sqrt{1-k^{2/3}} + arcsin(k^{1/3})) \tag{A.6}$$

where for a horizontal tube

$$v_0 \propto \sqrt{\frac{k}{\frac{m_a * m_b}{m_a + m_b}}} \tag{A.7}$$

$$Pbend = St * \theta \tag{A.8}$$

where C_{diff} is the diffusion coefficient, L is the tube length, Q the gas flow in m^3/s,v_s is the settling velocity, d the AED.

A

From this calculation it can be seen that the losses will affect only the particles with AED>10 μm. These particles have less importance in risk assessments, as they are transported for small distances and are not inhalable. Moreover by modifying the sample holder with a vertical system important contributions to the aerosols losses have been eliminated ($Pbend$ and $Pdep$) .

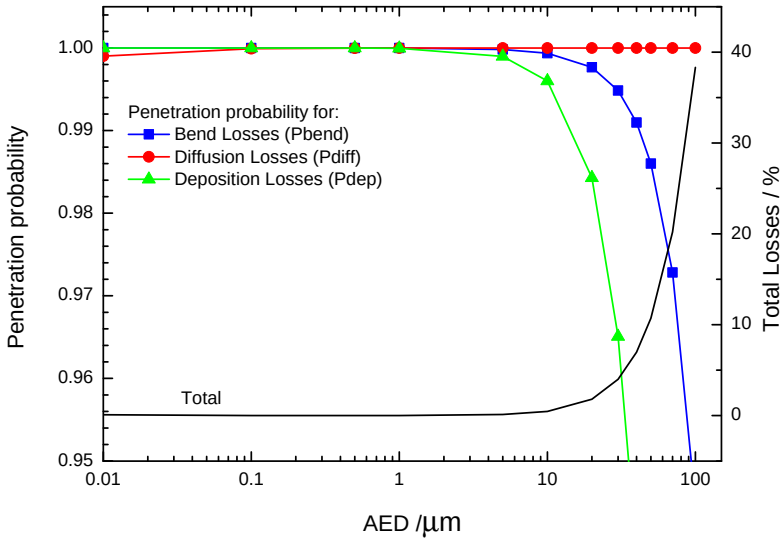

Figure A.1: Aerosol losses in the L-tube collection system, calculated for standard conditions, for a 30 l/min laminar flow before entering the MOUDI impactor.

REFERENCES

[1] P.A. Baron and K. Willeke. *Aerosol measurement: principles, techniques, and applications.* Wiley, 2 edition, 2001.

B

KNUDSEN EFFUSION MASS SPECTROMETRY

Mass spectrometry has been used for more than 60 years for the determination of high-temperature thermodynamic properties of condensed and gaseous phases [1]. It is an ideal method for the study of the vapour composition as it permits the identification of almost all gaseous species and the determination of their partial pressures. Moreover it is very sensitive and fast, thus allowing time-resolved measurements [2]. The instrument applied in our studies is confined in a 5 cm thick lead shielded glove box, which permits to study actinides compounds, but also small quantities of irradiated material.

The instrument used (shown in Figure B.1) is a Knudsen cell coupled with a mass spectrometer. A Knudsen cell is a closed cell, in which an equilibrium between the solid and gaseous phase can be achieved. The cell is small enough so that the average mean free path of the gaseous phase is bigger than the cell size (e.g. the gaseous species travel without collisions, a.k.a. Knudsen conditions). A small orifice (of diameter d) is made in the cell, from which a negligible quantity of gaseous phase escapes. The mass spectrometer (Pfeiffer-vacuum qma 400) measures the intensity of this gaseous beam, which is proportional to the pressure in the cell (as described in equation B.3). Once calibrated, one can deduce from the flow intensity the pressure in the cell. Knudsen conditions are achieved when the total pressure (P) remains below the value at which P/d of does not exceed 1 Pa/mm. When the pressure increase and the mean free path of the molecules become comparable to the dimension of the cell, collisions start to modify the flow ("failure-of isotropy") [1]. In order to maintain the equilibrium within the cell, the ratio between the effusing area (aC) and evaporation surfaces of the sample must be less than one (in our case, between 0.05 and 0.07).

The cell is heated by a high temperature furnace (up to 2500 K), made of tungsten

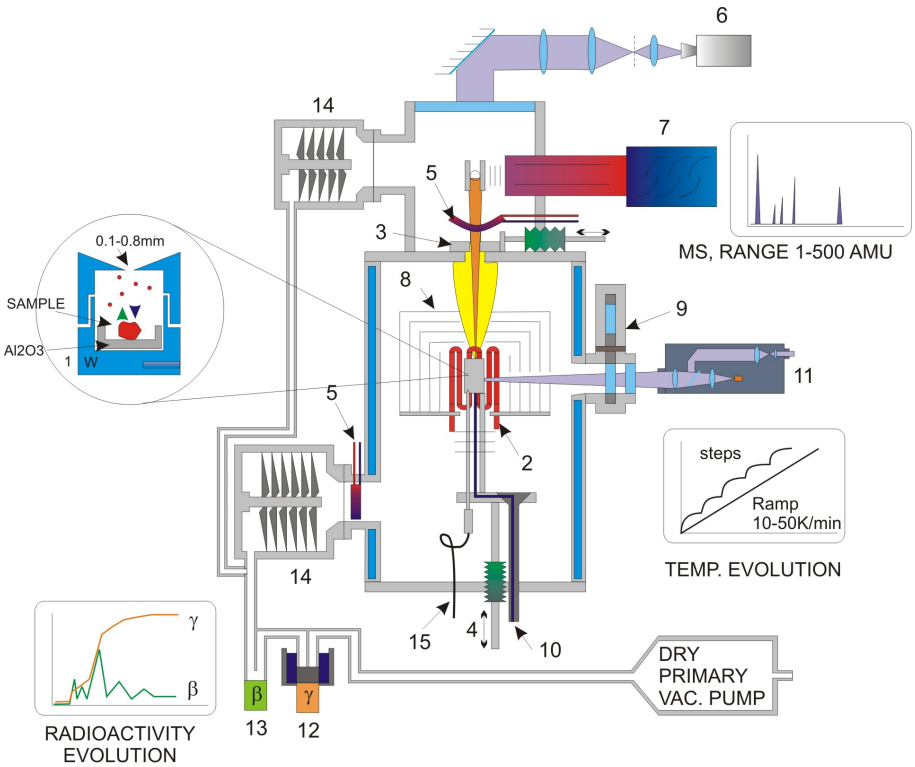

1: KNUDSEN-CELL WITH BLACK-BODY HOLE
2: TUNGSTEN RESISTANCE COIL
3: MOLECULAR BEAM CHOPPER FOR REFERENCE NOISE DIAGRAM
4: FACILITIES TO LIFT CELL FOR FAST HEATING
5: LN-TRAP TO REDUCE NOISE
6: CCD CAMERA TO ALIGN THE CELL HOLE AND CHOPPER DIAPHRAMGS
7: QUADRUPOLE MASS SPECTROMETER
8: THERMIC SHIELD (3 TUNGSTEN AND 4 TANTALUM)
9: REVOLVING PROTECTION WINDOWS
10: INLET GAS CAPILLAR
11: LINEAR PYROMETER
12: GAMMA-COUNTER WITH LN-TRAP
13: BETA-COUNTER
14: TURBO MOLECULAR PUMP
15: REMOVABLE W/Re THERMO COUPLE

Figure B.1: A schematic of the KEMS system used in our studies, from Gotcu [2].

coil-heating element surrounded by seven thermal shields, which ensure temperature homogeneity in the cell [3]. The temperature can be measured by a pyrometer, focused in a blackbody hole [4], or by thermocouples. The whole system is placed in an ultrahigh vacuum chamber (10^{-6}-10^{-4} Pa). Finally the Knudsen cell can be also equipped with a gas inlet to apply an external source of gas in the cell. The gas is introduced from an a small external reservoir kept at controlled pressure to permit a prompt response.[3]. In some of our studies a pressure of oxygen was used to study the effect of an oxidising environment on the release from simulated spent nuclear fuel.

The kinetic theory of gases shows that for each gaseous species i the flow can be expressed (mol/s) by Hertz-Knudsen equation [1]:

$$\frac{dn_i}{dt} = \frac{(p_i aC)}{(2\pi * M_i RT)}^{1/2} \tag{B.1}$$

where n_i is the number of atoms or molecules per unit of volume (in the cell) of species i, p_i its partial pressure and M_i its molar mass. R is the ideal gas constant 8.314 J/(mol*K), T is the absolute temperature and C is the Clausing factor. The Clausing factor is used to identified the transmission probability of the real orifice (C=1 for an ideal orifice). There are several empirical relations that can be used for C, as function of the diameter of the orifice and its length. Finally the integrated Hertz-Knudsen equation can also provide the mass loss by effusion during a period of time for the specie i [2]:

$$\Delta m_i = (p_i aC\delta T)\frac{M_i}{(2\pi * RT)}^{1/2} \tag{B.2}$$

The vaporized species (atoms and molecules) effused from the cell are then collimated through different apertures to the ionisation chamber of the mass spectrometer. A small number of the molecules or atoms (0.001%) are ionised by the electronic beam, extracted from the ionisation chamber and then analysed by the mass spectrometer. The intensity of the molecular beam for a species i, I_i^+ , is proportional to the vapour pressure in the cell according to the equation [2]:

$$p_i = \frac{I_i^+ T}{K_i} \tag{B.3}$$

where K_i is the calibration factor:

$$K_i = k_g k_i \tag{B.4}$$

k_g is an instrumental factor independent of the vaporized species and k_i a factor dependent on the species i by the formula:

$$k_i = \sigma_i \gamma_i f_i \tag{B.5}$$

where σ_i is the ionisation cross section of the species i, γ_i the efficiency of the secondary electron multiplier, and f_i is the isotopic abundance of species i. The ionisation

cross section is the parameter which has the most influenced and uncertainties in these calculations. It can be taken at the maximum of the ionisation efficiency curve or from theoretical calculations such as the ones of Mann or Otvos and Stevenson [5, 6]. Moreover Otvos and Stevenson [6] proposed the additive postulate for molecular cross sections which means that the cross section can be determined by adding the atomic cross sections of the constituent atoms.

The instrumental factor is determined instead by calibration of the system, at each experiment. This is performed by vaporising a known quantity of reference material together with the sample. The sample and the reference material have to be inert, to avoid their interaction. Often silver is used as a reference material because it is a metal with a well-known vapour pressure. Silver was chosen in our studies as it is inert in our systems and is vaporised completely up to 1400 K, generally before the matrix (UO_2) evaporation started. From the ion intensities (I_{Ag}) of the silver isotopes ^{107}Ag and ^{109}Ag and the vapour pressure of silver (p_{Ag}) obtained from literature data (such as Hultgren et al. [7]) the global calibration factor for silver (K_{Ag}=$k_g k_{Ag}$) can be determined experimentally by using equation [2]:

$$K_{Ag} = \frac{I_{Ag}^{+} T}{p_{Ag}} \tag{B.6}$$

From equations B.2 and B.6 we can obtain the expression of the calibration factor function of the known mass vaporized:

$$K_{Ag} = \frac{aCM_i{}^{1/2}}{\Delta m_{Ag}} \frac{\sum (I_{Ag}^{+} T1/2)^{1/2}}{2\pi * R} \delta t \tag{B.7}$$

Finally by dividing by k_{Ag} (the calibration factor dependent from the specie) the instrumental calibration factor (k_g) can be obtained. This can then be used for the determination of the partial pressure of the other species vaporized.

REFERENCES

[1] J. Drowart, C. Chatillon, J. Hastie, and D. Bonnell. High temperature mass spectrometery: instrumental techiniques, ionization, cross-sections, pressure measurments and thermodynamic data. IUPAC Technical Report. *Journal of Pure Applied Chemistry*, 77:683–737, 2005.

[2] P. Gotcu. Principles of the method: Knudsen cell mass spectrometry. Internal Communication, Report for Institute for Transuranium Elements.

[3] J.Y. Colle, D. Hiernaut, Papaioannou, C. Ronchi, and A. Sasahara. Fission product release in high-burn-up UO_2 oxidized to U_3O_8. *Journal of Nuclear Materials*, 348: 229–242, 2006.

[4] J.Y. Colle and F. Capone. Very high temperature laser heated furnace for knudsen cell mass spectrometry. *Review of Scientific Instruments*, 79:055105–1, 2008.

[5] J. B. Mann. Ionization cross sections of the elements calculated from meansquare radii of atomic orbitals. *Journal of Chemical Physics*, 46:1646, 1967.

[6] J. W. Otvos and D. P. Stevenson. Cross-sections of molecules for ionization by electrons. *Journal of American Chemical Society*, 78:546–551, 1956.

[7] R. Hultgren, R. L. Orr, P. D. Anderson, and K. K. Kelley. *Selected Values of Thermodynamic Properties of Metals and Alloys*. 1963.

SUMMARY

Nuclear Safety and Security are pillars for the application of the nuclear technology and for its acceptance by the public. The Fukushima accident has caused moreover a re-focus on nuclear reactor safety worldwide. This accident has shown that events previously considered unlikely can indeed happen and their environmental impact therefore needs to be evaluated. The safety of nuclear material has become consequently relevant not only during reactor operations, but also in all the other phases of the nuclear fuel cycle (including the storage and transport) and the assessment of the radiological consequences should be carried out also for these phases. Moreover after the $9/11^{th}$ terrorist attack the effect of dirty bombs detonations has become relevant in the public concern. To assess the consequences of such Radiological Dispersion Events (RDE's) it is necessary to perform a source term evaluation. This consist of a quantitative description of the radioactive release, which include both the gaseous species and aerosols released. The description of the aerosol release is also the input of codes calculating the extension of the contaminated area and the level of contamination. The results from such codes are needed for the creation of emergency plans and to plan mitigation strategies, but also to assess the health consequences of radioactive releases for the population. However the description of the source term can suffer from substantial uncertainties, which can affect the results of the calculations. Improvement of the radioactive source term description for such events is consequently of great importance.

A new experimental set-up (RADES, Radioactive Dispersion Events Set-up) was consequently developed for the purpose of producing and characterising aerosols that are typical for RDE's. This was tested on a wide range of materials and has proven to be suitable for the production and collection of aerosols under controlled laboratory conditions. The set-up permits to analyse the effect of different variables on aerosols characteristics by separate effect studies. In particular the effect of the chemical interactions between different materials or different atmospheres can be investigated. In addition the aerosol formation process was investigated by studying the aerosol gaseous precursors, using thermochemical equilibrium calculations and experimental vaporization studies (with Knudsen Effusion Mass Spectrometry). These techniques permit to study the gaseous release and the chemical reactions, which form the aerosols and influence their chemical compositions.

The RADES set-up was applied to study the aerosol released from different scenarios including dirty bombs detonations, release from simulated spent nuclear fuel under accidental and sabotage scenarios and also to investigate chemical reactions which can influence the radioactive release from nuclear fuel. From the first case, dirty

bombs' detonations, we found a bimodal size distribution, consisting of micrometer particles (related to the thermo-mechanical shock on the pellet), and agglomerates of nanometric particles (related to the condensation of the vapour formed). The fractional release between the two characteristic aerosols size ranges in a RDD cannot be reproduced in our experiments, due to the impossibility to control and scale the shock wave. The aerosols formed from the vaporization process instead can be simulated, as the experiments permit reproducing a fast high-temperature gas release rapidly quenched by a cool air environment. High attention for the risk assessment is focused on these particles due to their long range transport in the environment and their high probability of deposition in the lungs when inhaled. Thus our set-up can be applied to study the formation and characteristics of these particles. From the experiments we identify the CsCl source as the most dangerous mainly due to its higher release. In these studies we tested also the influence of cladding materials (tungsten and/or stainless steel) on the aerosols characteristics. Our experiments showed that the claddings can affect the release by the formation of new compounds with different properties or by a different agglomeration behaviour. This can finally lead to a modified size distribution and to a different elemental and chemical speciation of the aerosols as function of their size. This influences the radioactivity partitioning in the aerosols, with finally an impact on the results of codes calculating the radiological consequences of such events.

We also investigated the aerosol release from simulated spent nuclear fuel, in view of accidents and sabotage involving spent fuel storage or during spent fuel transport. In particular, we studied the aerosol size distribution and the fission product partitioning in the different aerosol size ranges, as these can have an effect on the risk assessment by an element specific partitioning in the aerosols. Different simulated spent nuclear fuels were tested and showed a similar trend for the size distribution, morphology and elemental partitioning with size of the aerosols. The higher volatile elements were enriched in the smaller particles (e.g. Cs, Ru, Mo), while the lower volatile elements were concentrated in the bigger particles (e.g. Ce, Ba, U). This effect was correlated to the aerosol formation mechanism. The smaller particles are formed by the condensation of the vapour release (enriched in high volatile elements), while the bigger particles are formed by the ejection of liquid or solid material from the pellet (eventually enriched in low volatile elements). This partitioning of the radioactive elements as function of size ranges can affect the risk associated to their inhalation, as highly radio-toxic elements are concentrated in the respirable fraction. On the other hand by separate effect studies we observed that the aerosols containing the dangerous radioactive element Pu, simulated by Ce, will be concentrated in the particles with bigger AED. Thus this elemental partitioning phenomenon can lead to radioactivity redistribution in the aerosols as function of the particles size.

This study has shown that our novel approach of coupling of the aerosolization experiments with the equilibrium vaporization studies is effective, as it permits to predict the chemical forms of the fission products in the aerosols, the influence of the oxidising environments on the release (such as of noble metal fission products)

and to understand chemical reactions that lead to the formation of new compounds. In particular the thermochemical equilibrium calculations showed the formation of Cs_2MoO_4 by the interaction of CsI with Mo, and a possible effect on the release of free molecular iodine in oxidising conditions. By seperate effect studies we subsequently assessed the effect of these chemical reactions on the aerosol characteristics and on the iodine gaseous release. We observed that while the reaction between CsI and Mo will have a strong effect on the release, the reaction between CsI and Ru does not strongly affect the release. The interaction of these compounds in oxidising conditions can break the CsI bond by the formation of Cs_2XO_4 (X=Mo, Ru) species, releasing gaseous I_2 at low temperature. Finally these experiments demonstrated a dependence of the chemical composition on the particles AED for the CsI-Mo mixtures, that CsI aerosols were collected mainly in the bigger AED>5.6 μm, while the MoO_3 aerosols were collected in the smaller AED<1 μm, and finally that mixed aerosols containing Cs_2MoO_4 were observed in the middle MOUDI stages with 1 μm<AED<5.6 μm. In view of the importance of the formation of these compounds (Cs_2XO_4) on the radioactive release and the lack of Raman patterns, which are used in this study to identify the chemical composition of the aerosols, a study was finally performed on the crystal structure and vibrational features of Cs_2RuO_4. The Raman band assignment of Cs_2RuO_4 was performed by a coupling of symmetry selection rules as predicted by group theory and quantum chemical analysis. A phase transition was observed by Raman laser heating. This phase transition was confirmed by high temperature X-ray diffractometer measurement at 975 K.

SAMENVATTING

Nucleaire veiligheid en beveiliging zijn de hoekstenen voor de toepassing van nucleaire technologie en diens acceptatie bij het publiek. Het Fukushima ongeluk heeft bovendien een wereldwijde hernieuwde interesse in reactorveiligheid veroorzaakt. Dit ongeluk heeft laten zien dat eerder onwaarschijnlijk geachte gebeurtenissen kunnen plaatsvinden en dat hun impact op het milieu moet worden geëvalueerd. De veiligheid van nucleair materiaal is aanzienlijk relevanter geworden, niet alleen gedurende de normaal bedrijf van reactoren, maar ook tijdens alle andere fases van de brandstofcyclus (inclusief opslag en transport) en de beoordeling van de radiologische gevolgen moeten ook voor deze fases worden uitgevoerd. Daarnaast zijn na de terroristische aanval van 11 september de effecten van vuile bom explosies meer relevant geworden voor het publieke belang. Om de gevolgen de verspreiding van radioactief materiaal door zulke radiologische dispersie gebeurtenissen (RDE's) te beoordelen is het nodig de bronterm te evalueren. Deze beschrijft de hoeveelheid van de vrijgekomen radioactieve stoffen, zowel in gas vorm als in aerosolen vorm. De beschrijving van de aerosolen is ook de invoer voor de computerprogramma's die de omvang van het besmette gebied en het niveau van de besmetting modeleren. De resultaten van dit soort modellen zijn nodig voor het ontwerp van noodplannen en mitigatie strategieën, alsmede om de consequenties van de radioactieve stoffen voor de volksgezondheid te beoordelen. Helaas kan de beschrijving van deze bronterm gevoelig zijn voor onzekerheden, welke het resultaat van de berekeningen kunnen beïnvloeden. Verbetering van de beschrijving van de radioactieve bronterm voor dit soort gebeurtenissen is daarom van groot belang.

Een nieuwe experimentele opstelling (RADES, radioactieve dispersie gebeurtenissen opstelling) is ontwikkeld, met als doel om de aerosolen te produceren en karakteriseren die kenmerkend zijn voor RDE's. De opstelling is getest voor een breed scala van materialen en is bewezen geschikt te zijn voor de productie en verzameling van aerosolen onder gecontroleerde laboratorium condities. De opstelling maakt het mogelijk de effecten van de verschillende variabelen op de karakteristieken van de aerosolen afzonderlijk te onderzoeken. In het bijzonder kan het effect van de interactie tussen verschillende materialen of verschillende atmosferen worden onderzocht. Daarnaast werd het aerosolvormingsproces onderzocht door het bestuderen van de gasvormige voorlopers van de aerosolen met behulp van de thermochemische evenwichtberekeningen en experimentele studies van de verdamping (met Knudsen effusie massaspectrometrie). Deze technieken maken het mogelijk om de gasvormige vrijzetting en chemische reacties waardoor de aerosolen vormen en die hun chemische samenstelling beïnvloeden, te onderzoeken.

De RADES opstelling werd toegepast om de aerosolen die vrijkomen bij verschillende scenario's met onder andere vuile bom ontploffingen, vrijzetting uit gesimuleerde gebruikte nucleaire brandstof bij ongelukken en sabotage scenario's te bestuderen en ook om chemische reacties die de radioactieve vrijzetting van nucleaire brandstof kunnen beïnvloeden te onderzoeken. Voor het eerste geval, de vuile bom ontploffingen, vonden we een bimodale grootteverdeling, bestaande uit deeltjes in het micrometer bereik (die gerelateerd zijn aan de thermo-mechanische schok op de pellet), en agglomeraten van nanometrische deeltjes (die gerelateerd zijn aan de condensatie van de gevormde damp). De fractionele verdeling tussen de verschillende bereiken van deeltjesgrootte in een RDE kan niet worden gereproduceerd in onze experimenten, vanwege de onmogelijkheid om de schokgolf te controleren en schalen. Maar de aerosolen die worden gevormd door het verdampingsproces daarentegen kunnen worden gesimuleerd, aangezien het experiment het mogelijk maakt om het gas dat bij hoge-temperatuur vrij is gekomen snel af te koelen in een koude omgeving. Er is veel aandacht aan deze deeltjes geschonken gezien ze over grote afstanden getransporteerd kunnen worden in het milieu en de hoge waarschijnlijkheid van afzetting in de longen bij inademing. Zodoende kan onze opstelling worden toegepast om de vorming en karakteristieken van deze deeltjes te bestuderen. Uit alle experimenten kunnen we de CsCl bron als het meest gevaarlijke aanwijzen vanwege zijn hoge uitstoot. In deze studie hebben we ook de invloed van omhullingmaterialen (wolfraam en/of roestvrij staal) op de karakteristieken van de aerosolen bestudeerd. Onze experimenten hebben laten zien dat het omhullingmateriaal een effect kan hebben door de vorming van nieuwe bverbindingen met andere eigenschappen of door een veranderd agglomeratiegedrag. Dit kan uiteindelijk leiden tot een veranderde grootteverdeling en tot een veranderde elementaire en chemische verdeling van de aeroloen als functie van hun grootte. Dit beïnvloed de radioactieve partitionering in aerosolen, wat tenslotte een invloed kan hebben op de resultaten van de modellen die de radiologische gevolgen van dit soort evenementen uitrekenen.

We hebben ook onderzoek gedaan naar de vrijlating van aerosolen uit gesimuleerde afgebrande splijtstof, met het oog op ongelukken en sabotage bij de opslag en transport van verbruikte brandstof. In het bijzonder bestudeerde we de aerosol grootteverdeling en de splijtingsproducten partitionering in de verschillende aerosol grootte bereiken, want deze kunnen een effect hebben op de risicobeoordeling vanwege een element specifieke partitioning in de aerosols. Verschillende gesimuleerde afgebrande splijtstoffen werden getest en vertoonden een soortgelijke trend voor de grootteverdeling, morfologie en elementaire verdeling als functie van de groote van de aerosolen. De meer vluchtige elementen waren verrijkt met kleinere deeltjes (bijv Cs, Ru, Mo), terwijl de minder vluchtige elementen (bijvoorbeeld Ce, Ba, U) in de grotere deeltjes waren geconcentreerd. Dit effect kon worden gecorreleerd aan de aërosolvormingsmechanisme. De kleinere deeltjes worden gevormd door de condensatie van de vrijgekomen damp (verrijkt in meer vluchtige elementen), terwijl de grotere deeltjes worden gevormd door het uitwerpen van vloeibaar of vast materiaal uit het tablet (eventueel verrijkt in minder vluchtige elementen). Deze verdeling van de radioactieve elementen als functie van grootte kan het risico van inhalatie beïnvloeden, aangezien

zeer radiotoxische elementen geconcentreerd zijn in de inadembare fractie. Anderzijds, bij afzonderlijke-effect-studies zagen we dat de aerosolen die het gevaarlijke radioactieve element Pu bevatten, gesimuleerd door Ce, geconcentreerd waren bij een grotere AED. Dit verschijnsel kan dus leiden tot een herverdeling van de radionucliden in de aerosolen als functie van de deeltjesgrootte.

Dit onderzoek heeft aangetoond de koppeling van de aerosolvormingsexperimenten met evenwichtstudies van de verdamping effectief is, want het maakt het mogelijk de chemische vorm van de splijtingsproducten in de aerosolen te voorspellen, de invloed te begrijpen van de oxiderende omgeving op de vrijzetting (zoals de edelmetaal splijtingsproducten) en de chemische reacties die leiden tot de vorming van nieuwe verbindingen. In het bijzonder bleek uit de thermochemische evenwichtsberekeningen dat de vorming van Cs_2MoO_4 door de interactie van CsI en Mo, een mogelijk effect heeft op het vrijkomen van moleculair jodium in oxiderende omstandigheden. Door een afzonderlijk-effect-studie hebben we vervolgens de gevolgen van deze chemische reacties op de aerosol-kenmerken en op de vrijzetting van gasvormig jodium onderzocht. We zagen dat de reactie tussen CsI en Mo een grote invloed op de vrijlating zal hebben, terwijl het effect bij de reactie tussen CsI en Ru zo sterk zal zijn. De interactie van deze verbindingen bij oxiderende omstandigheden kan de CsI binding verbreken door de vorming van Cs_2XO_4 (X=Mo, Ru) moleculen, waarbij gasvormig I_2 bij lage temperatuur vrijkomt. Tenslotte toonden deze experimenten een afhankelijkheid van de chemische samenstelling op de AED van de deeltjes voor CsI-Mo mengsels. De Csl aerosolen werden vooral waargenomen in het grotere AED>5.6 μm bereik, terwijl de MoO_3 aerosolen waargenomen werden in het kleinere AED<1 μm bereik, en tenslotte werden gemengde aerosolen die Cs_2MoO_4 bevatten waargenomen in de middelste MOUDI stadia 1 μm<AED<5.6 μm. Gezien van het belang van de vorming van deze verbindingen (Cs_2XO_4) bij de vrijzetting van radioactieve elementen en het ontbreken van Raman patronen die in deze studie werden gebruikt om de chemische samenstelling van de aerosolen te bepalen, werd uiteindelijk een onderzoek uitgevoerd naar de kristalstructuur en vibratie eigenschappen van Cs_2RuO_4. De toewijzing van de gemeten Raman banden aan Cs_2RuO_4 werd uitgevoerd door een koppeling van symmetrische selectieregels zoals voorspeld door groeptheorie en kwantumchemische analyse. Een fase overgang werd waargenomen tijdens Raman laser verhitting, en deze faseovergang werd bevestigd door een hoge temperatuur röntgendiffractometer meting bij 975 K.

CURRICULUM VITÆ

16-07-1987 Born in Cork, Ireland.

EDUCATION

2006	Undergraduate Liceo Scientifico Informatico, Ladispoli (Rome)
2009	Bachelor Degree Università La Sapienza, Rome
2011	Master Degree Università La Sapienza, Rome
2015	Ph.D. Delft University of Technology
Thesis:	Characterisation of aerosols from simulated Radiological Dispersion Events
Promotor:	Prof. dr. R.J. M. Konings

PROFESSIONAL EXPERIENCE

2009	Trainee on the Charaterisation of Sorbent for CO_2 Polo a Idrogeno Civitavecchia (Rome), Italy
2011-2012	Trainee on the RADES set-up development European Commission, Joint Research Centre, Institute for Transuranium Elements, Karlsruhe, Germany
2012-2015	Grant holder on the evaluation of source term for RDE's European Commission, Joint Research Centre, Institute for Transuranium Elements, Karlsruhe, Germany

EXTRA CURRICULA ACTIVTIES

2013	Member of the local organising committee for the IWSSTP2013 (International Workshop on SubSecond ThermoPhysics)
2013	Electron microscopy demonstration at EFFEKTE 2013 Wissenschaftsfestival-Science Festival
2014	Organization of a workshop and a panel session at the IYNC2014 (International Youth Nuclear Conference)

LIST OF PUBLICATIONS

Chapter 1 of this thesis constitutes a paper already published in a peer reviewed scientific journal. From the other academic chapters extract have been submitted for peer review to scientific journals.

- Di Lemma F.G., Colle J.-Y., Ernstberger M., Rasmussen G., Thiele H., Konings R. J. M., *RADES an experimental set-up for the characterization of aerosol release from nuclear and radioactive materials.* Journal of Aerosol Science 70, 36-49.

- Di Lemma F.G., Colle J.-Y., Ernstberger M., Konings R. J. M.*Characterisation of aerosols from RDD's surrogate compounds produced by fast thermal transients.* Accepted under revision by Journal of Nuclear Science and Technology, 2015.

- Di Lemma F.G., Colle J.-Y., Rasmussen G., Konings R. J. M. *Fission products partitioning studies on simulated aerosol release from spent nuclear fuel.* Submitted, 2014.

- Di Lemma F.G., Colle J.-Y., Beneš O., Konings R.J.M. *A separate effect study of the influence of metallic fission products on CsI radioactive release from nuclear fuel.* Accepted under revision by Journal of Nuclear Materials, 2015.

- Naji M., Di Lemma F.G, Kovács A., Beneš O., Manara D., Colle J.-Y., Pagliosa G., Raison P., Konings R.J.M. *Combination of Raman spectroscopy and Quantum chemical analysis for the vibrational features of* Cs_2RuO_4. Accepted under revision by Journal of Raman Spectroscopy, 2015.

PRESENTATIONS

- Di Lemma F.G., Colle, J.-Y., Ernstberger M., Thiele H., and Konings R. J. M., *Experimental aerosol characterization for the evaluation of source term from RDE's (Radiological Dispersion Events.* EAC, 2012, European Aerosol Conference. Oral Presentation.

- Di Lemma F.G., Colle J.-Y., Ernstberger M., Rasmussen G., Van Winckel S., Avincola, V., and Konings, R. J. M. *Fast experiments for simulation of RDE's and source term characterization.* 10th IWSSTP, 2013, International Workshop on Subsecond Thermophysics. Oral Presentation.

- Di Lemma F.G., Colle J.-Y., Ernstberger M., Thiele H., Rasmussen G., Avincola V., and Konings R.J.M. *RADES (Radiological Dispersion Events Set-up) and result from the characterization of the aerosols from simulated RDE's.* EAC2013, European Aerosol Conference. Poster.

- Di Lemma F.G., Colle J.-Y., Beneš O., and Konings R.J.M. *Knudsen Cell measurements applied for the study of gaseous precursors and chemical process acting in aerosol formation for the RADES set-up.* EAC 2013, European Aerosol Conference. Poster.

- Di Lemma F.G., Colle J.-Y., Rasmussen G., Van Winckel, S., Thiele H. and Konings R.J.M. *An ICP-MS analysis on aerosols from simulated nuclear fuel, to study the elemental composition of particles released during nuclear accidents.* EAC 2013, European Aerosol Conference. Poster.

- Di Lemma F.G., Colle J.-Y., Ernstberger M., and Konings R. J. M.*Characterization of aerosols from simulated dirty bombs detonations.* GAEF, 2014, Gesellschaft fuer AErosolForschung. Oral Presentation.

- Di Lemma F.G., Colle J.-Y., Beneš O., Rasmussen G., Van Winckel S., and Konings R. J. M., *Chemistry studies for radioactive aerosols in simulated severe accidents.* IYNC 2014, International Youth Nuclear Conference. Oral Presentation.

ACKNOWLEDGMENTS

The decision to undergo or not a Ph.D. was at first for me a controversial decision, being away from my family in Italy and prolonging my study for another three years were my biggest fears. However after these 3 years, having overcome the initial difficulties, I do not in the slightest regret my decision. These have been the most interesting, challenging, and fun years of my life.

I would therefore thank the European Commission, the JRC and the former Director Prof. Dr. Fanghänel to have given me the possibility to perform this project. An important thanks goes to the 7^{th} Framework Program of the European Commission for the grant support.

I would like also to thank TU Delft for giving me the possibility with this work to candidate for a Ph.D. and in particular I would like to thank the Beadle office, and especially Thea (from the Radiation Science & Technology Department), and Ans (from the Graduate Office of Applied Sciences) for the help during this process and the (complicated) administrative issues.

A special thanks goes to to all the doctoral committee members for the precious time and comments.

Most of all I would like to thank Prof. dr. Rudy Konings, which has been my promotor and supervisor. Helping me daily with the scientific doubts and personal fears, challenging me to test new ideas and giving always direction and precious advices.

I would like to acknowledge the contribution to this work and to my personal development by Jean-Yves. He has been my guide in all scientific and technical matters. Whenever I needed it, I could count on him. I would not have accomplished any of this work without his precious contribution.

I would like to thank my former professor Prof. Dr. Cumo and Dr. Rondinella for helping me and introducing me to the ITU research centre.

In particular I would like to thank my unit, "Materials Research", for the help in every analysis, GB issues, for the suggestions and also for a simple talk at the coffee machine. I would like especially to acknowledge the precious scientific and technical help (and friendship) from Annette, Dario, Dinos, Dragos, Ondrej, Mark, Alex and Luka. Special thanks goes to the Microscope group Bert, Markus, Hartmut, and Thierry

for helping in the SEM characterisation, teaching me how to use the instruments, their encouragement and friendship, and especially for the FILAMENTS. A special acknowledgment goes to Mohamed, Attila and Philippe for the help in the study of the vibrational features of the Cs_2RuO_4. An enormous Dankeschön finally goes to Petra for helping every day with the ITU administrative issue, for the precious suggestions, encouragement and friendship.

I would like to thank the XRD group Giorgio Pagliosa, Daniele Bouexiere and Philippe Raison, for the analyses, the discussions and the help. The ICP-MS group Gert, Helene, Stefaan, Mariangela and Brian for all the analyses performed and for the enormous effort they put in this work. A special acknowledgment goes to Detlef Wegen, Paul Carbol and Vincenzo Rondinella for providing the AECL simfuels and helping in the characterisation of the samples. I would likt to thank also Nicole for the precious MOUDI impactor, Klaus and Jean for the fruitful talks and scientific discussions. To the workshop a special thanks for every part of RADES they helped build.

I would like finally to thank my companions the "Research fellows group" for the dinners, discussions, disco nights and just for sharing this challenging experience. In particular I would like to thank the "Germans" Oliver, Kevin and Lars for their friendship, laughs and also for the help in my 2^{nd} house moving. A special thank to Victor, the first student I supervised, for the help with Dutch translations and in the lab.

The "Italian group" deserve an important acknowledgement for the lunches together, the coffees and making me feel at home. To Valentina, Elisa, Fabiola, Luca, Tsvetolavo (you are ORMAI ITALIANO), Dario, Concetta, Simona e Zap un grazie SPECIALE!!!

Especially I would like to thank Valentina for sharing every phase of this turbulent experiences, from the start to the end, I acknowledge you as one of my best and closest friends. We have faced all the fears and problems together, from finding a place were to live to the Ph.D. dissertation. To Elisa for being my office lady, for the laugh, the songs, correcting each other sentences during the writing of our articles, for the lab hours, and finally to listen to all my complains. To Fabiola for the energy, encouragement and friendship, for just passing by when I did not want to talk, for getting angry for me when I was not able to do so myself.

The front and back cover were designed by Alessia Travanti. Front was retrieved and modified from http://sheridancollege.files.wordpress.com/2012/07/133834900.jpg. For this I would like to deeply thank Alessia Travanti and also Roberto Alesi for the amazing bookmark.

A special thanks goes to my family, they have always cared for me and supported me in every decision I made (also if it means I will go further away from home). To my mother for giving me unconditional love, support, and for the innumerable St.

Anthony candles. To my father for transmitting all the important values of hard work, trustiness, and loyalty. To my sister to whom I will always look up as an example of generosity, kindness and determination. To Zio Gege a special thanks for all the help and support.

Grazie to my friends: Chiara, Serena, Sonia, Lollo e Matilde, for every time they traveled just to see me, for the calls, whatsAPP group conversions and just for their special friendship. I feel close to you everyday and I know that our friendship will last eventhough the oceanic distances. "Me dovete ancora SOPPORTA'!"

A special thanks goes to Anja and Simon and their families for making me feel always welcome and "integrated", for sharing with me all the Germans traditions, for all the "Grillen" and "Fasching" parties, breakfasts and dinners, finally for the "Urlaub" together.

Grazie mille to Luca, my first fan, my best friend (also if he does not like this word) and partner, for every dinner out, for every coccola, for every suggestion (even if you think I am not listening). I feel lucky everyday to be able to see the generous, intelligent and successful man you are becoming.

I know I have surely forgotten someone, because I met so many wonderful people during these years, but you know I am deeply thankful to all of you.

ARIGATO GOZAIMASU!!!